An Experimental Conduction Error Calibration Procedure for Cooled Total Temperature Probes

Steven Tyler Englerth

Thesis submitted to the faculty of the Virginia Polytechnic Institute and State University in partial fulfillment of the requirements for the degree of

Master of Science

In

Aerospace Engineering

K. Todd Lowe

Joseph A. Schetz

William J. Devenport

February 23rd, 2015

Blacksburg, Virginia

Keywords: Heat transfer, Conduction Error, Total Temperature Probe

An Experimental Conduction Error Calibration Procedure for Cooled Total Temperature Probes

Steven Tyler Englerth

ABSTRACT

The accurate measurement of total temperature in engine diagnostics is a challenging task which is subject to several sources of error. Conduction error is predominant among these sources since total temperature sensors are embedded into a cooled strut for measurement. This study seeks to understand the effect of conduction error on total temperature probe performance from an analytical and experimental standpoint and to provide an effective calibration procedure. The review of historical low-order models, as well as results from a developed thermal resistance model, indicates that conduction error is driven by dimensionless parameters, including the Biot, Nusselt, and Reynolds Numbers, as well as a non-dimensional temperature characterizing the flow/strut temperature difference. A conduction error calibration procedure for total temperature probes is experimentally tested in this study. Data were acquired for nominal flow total temperatures ranging from 550 °F to 850 °F with the probe Reynolds number varying from 2,000 to 12,000 for varying conduction conditions with axial temperature gradients up to 1150 °F per inch. A physics-based statistical model successfully expressed total temperature probe performance as a function of dimensionless conduction driver and probe Reynolds number. This statistical model serves as a "calibration surface" for a particular total temperature probe. Due to the scaling of the problem, this calibration is experimentally obtained in moderate temperature regimes, then implemented in higher temperature regimes. The calibration yields an overall uncertainty in total temperature measurement to be ±4% of the total temperature for flow conditions typical in engine diagnostics, with extreme uncertainties in input conditions. Conduction error is successfully shown to be independent of any temperature regime and driven by dimensionless parameters.

Acknowledgements

I want to thank everybody that has been a part of this work and has supported me throughout my years at VT. Thanks to Dr. William Devenport for guiding me in my initial undergraduate research days; this was valuable experience that helped prepare me for graduate school. Thanks to Drs. Todd Lowe and Joseph Schetz for being excellent advisors and pushing me to maintain a high standard for my work.

I want to thank Pratt and Whitney for funding this research and continuing a great partnership through the Center of Excellence with Virginia Tech. The work for this thesis was completed for Pratt and Whitney Center of Excellence task #84. Dr. Charlie Haldeman, Andrew Consiglio, and Justin Urban have all been great to work with and have helped me grow as an engineer and experimentalist and will be great mentors in my future career with Pratt and Whitney. I have had a ton of fun with this project and am looking forward to others like it.

Thanks to the students in Dr. Lowe's lab, namely Donnie Brooks, Dan Cadel, and Tobias Ecker. You guys have been great friends and you have taught me a lot about our facilities. Thanks to Alex Schneider for his computational work with total temperature probes and for being there to bounce ideas off of.

Thanks to the AOE machine shop, namely James Lambert, Andy Tawney, and Cameron Hollandsworth for their fantastic work in my research projects. Thanks to Mark Montgomery for helping me expand my knowledge of electronics and for his help in the lab. Thanks to the AOE front office for processing my numerous purchase orders and to Steve Edwards and Jonathan Spence.

Thank you to my family for always supporting my educational path; it's too bad Connecticut is so far away from South Carolina! Thanks to the Mangi for the good times in Blacksburg over the years. Thanks to my girlfriend, Stephanie, for being by my side and her patience with my Masters completion. It has been a long journey but it is finally nearing the end.

Table of Contents

List of Figures

List of Tables

Nomenclature

Θ	Conduction driver
M	Free stream Mach number
h	Coefficient of convective heat transfer
k	Thermal conductivity, W/m/K
Re	Reynolds number
Nu	Nusselt number
Bi	Biot number
R	Overall sensor recovery factor
$\overline{R}$	Overall Mach corrected recovery factor
α	Aerodynamic recovery factor
L	Thermocouple immersion length from base
d	Diameter of thermocouple or thermocouple wire
γ	Gas constant
Q	Amount of heat transferred
I	Electrical current
$\underline{R}$	Electrical resistance

Subscripts

j	Thermocouple junction
t	Stagnation/total condition
s	Static condition
b	Base, the point of contact between thermocouple and strut
c	Convective, pertaining to the thermocouple junction
w	Wall
R	Radiation
d	Diameter of thermocouple used as characteristic length scale
ID	Inner diameter of stagnation tube used as characteristic length scale
flow	Pertaining to the fluid property
solid	Pertaining to the solid property
wire	Pertaining to the wire for a bare wire thermocouple junction

Abbreviations

TRM	Thermal resistance model
L/d	The effective length to diameter ratio of a thermocouple
Conv	Convective
Cond	Conductive
Rad	Radiative
ID	Inner diameter of stagnation tube

1 INTRODUCTION

Accurate measurement of flow total temperature in many hot flows of practical interest, including jet engines, is a critical task. In jet engine industry, it is important for efficiency assessment and blade design. Maximizing the combustion temperature is critical for the thermal efficiency and thrust per rate of airflow through the core engine.[1] In general, this combustion temperature is bounded by blade durability. Blades are manufactured hollow to create internal cooling channels. These internal cooling channels are tapped into on the blade surface in order to provide a layer of cooling air on the blade surface. Thus, there exists a large temperature gradient between the freestream flow and the blade surface.

Measurement of the total temperature in particularly harsh regions of an engine requires specially designed thermometry. Sensors composed of a thermocouple and stagnation tube assembly have been a successful standard for total temperature measurement, as seen in Figure 1.1. The sensor and its support structure must consist of material appropriate for exposure to this temperature regime. Just as blades are subjected to cooling in the hot section, the support structure must be cooled to prevent structural failure. The total temperature sensors are generally embedded in a cooled rake. Thus, the total temperature sensors are in direct thermal contact with the cooled support structure, subjecting the sensor to a large temperature gradient from sensing location to the thermal contact with the cooled support structure. The sensor being in direct thermal contact with the cooled support structure directly impacts its performance via error due to heat conduction away from the sensing location. The results presented in this study seek to understand and quantify the effect that conduction between total temperature sensor and its immediate support structure has on sensor performance.

1.1 GENERAL RELATIONSHIPS GOVERNING THERMOCOUPLE PERFORMANCE

A thermocouple reading is significantly dependent on the temperature at its measurement junction.[2] This measurement results from a heat balance between several sources; heat transfer by conduction within the thermocouple, heat transfer by radiation to or from the thermocouple, heat transfer through the boundary layer via convection, and conversion of flow kinetic energy to thermal energy within the boundary layer. Each of these heat transfer mechanisms contributes to the measurement error which is manifested as a deviation from the flow total temperature. These heat transfer mechanisms are calculated and combined into a total error equation, which has been well documented in previous works.[2-6] The measurement errors due to this heat transfer balance are traditionally termed as velocity error, conduction error, and radiation error. Heat transfer via convection occurs when the gas is moving, thus convective error is termed velocity error. There is additional error, termed transient error, associated with measurement of transient temperatures due to the thermal capacity of the thermocouple.

The heat transfer balance that results in the indicated thermocouple temperature is shown in Figure 1.1. The oncoming free stream flow is ingested by the stagnation tube and flows across the thermocouple and out of the exit vent. Heat convects from the fluid to the thermocouple at the leading edge stagnation point and across the streamwise length of the thermocouple which is in

contact with the moving fluid. This heat transfer mechanism is indicated by q_{conv}. Heat radiates from the thermocouple to its surroundings, i.e. primarily the stagnation tube and objects upstream of the thermocouple junction and is represented as q_{rad}. If there exists a large temperature difference between the base of the sensor assembly and the free stream total temperature, heat will conduct away from the thermocouple junction. The conductive heat transfer mechanism is indicated as q_{cond}. It is critical to realize that the temperature indicated by a thermocouple is simply a heat transfer balance between convective, conductive, and radiative heat mechanisms.

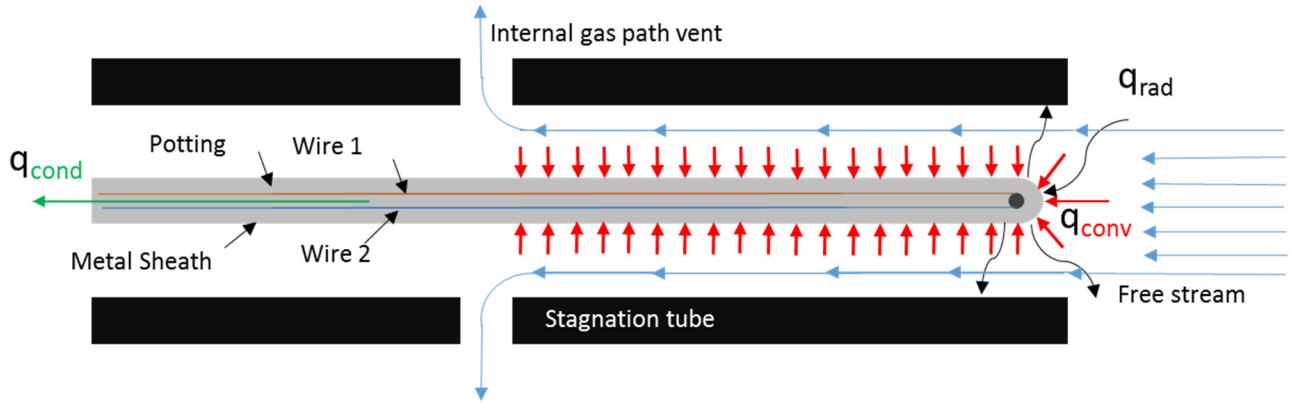

Figure 1.1: Generalized schematic for a shielded total temperature probe geometry and sources of heat transfer.

There are several approaches to accurately measuring the flow total temperature that include: (1) measurement using a simple bare wire thermocouple and correcting its reading based on known environmental effects, (2) using a sonic velocity aspirated probe that has a constant correction factor, or (3) designing a probe that minimizes error from all sources and does not require a correction factor.[2] These approaches all depend on understanding thermocouple performance related to the environment it is exposed to; it is the task of the designer to create an environment that is favorable for total temperature measurement within an acceptable accuracy. Historical and modern designs of total temperature probes favor the third approach. These so called "direct reading" probes are easier to use and do not require as rigorous a correction process or precise knowledge of operating environment.[2] Direct reading probes require careful design such that all sources of error are minimized; this generally requires elaborate probe geometries which are not always practical to use. Due to spatial limitations in engine testing, design of direct reading probes are more of an academic exercise than a practical solution.

1.1.1 Overall Recovery Factor

For the purpose of this study, the overall thermocouple performance will be defined by the ratio of the temperature measured by the thermocouple and the flow total temperature. This relation is shown in Equation (1.1), where R is the overall recovery factor, T_j is the thermocouple measured temperature, and T_t is the flow total temperature.

$$R = \frac{T_j}{T_t} \tag{1.1}$$

This overall recovery factor serves as a measure of how well the total temperature probe under test recovers the total thermal energy of the flow. Recall the previous discussion of Figure 1.1 that indicated that the measured thermocouple temperature is the result from a heat transfer balance between convection, conduction, and radiation. Of these three heat transfer mechanisms, convection is key in how heat is transferred from the moving fluid to the thermocouple junction. A moving fluid has a total energy that is made up of thermal energy and kinetic energy. From a purely aerodynamic standpoint, it is important to determine the baseline probe performance. The effect of conduction, fluid velocity, and radiation on probe performance will then be explored after the baseline aerodynamic study has been performed.

1.1.2 Aerodynamic Recovery Factor

The aerodynamic recovery factor is a measure of how well a probe recovers the kinetic energy of fluid flow as thermal energy. A moving fluid has a higher temperature when brought to rest due to the kinetic energy associated with its motion by the first law of thermodynamics. This thermal and kinetic energy of the flow is conserved and combined to give a measure of the total energy, of the moving fluid, termed the total temperature. Therefore the relationship between total temperature and static temperature is simply proportional to the kinetic energy of the flow. The kinetic energy of the flow scales on the square of fluid bulk velocity and requires knowledge of the specific heat of the fluid. Thus the temperature equivalent of the flow kinetic energy is T_t-T_s, where c_p is the specific heat of the fluid.

$$T_t - T_s = \frac{V^2}{2c_p} \tag{1.2}$$

The temperature measurement T_j at the thermocouple junction is indicated to be some temperature between the static and total temperature, i.e. $T_s < T_j < T_t$. The temperature equivalent of kinetic energy recovered by the thermocouple is taken to be T_j-T_s. How well the thermocouple recovers the total kinetic energy of the flow is indicated by the aerodynamic recovery factor α, given in Equation (1.3). This definition is simply the ratio of kinetic energy recovered by the thermocouple versus the total kinetic energy contained in the moving flow.

$$\alpha = \frac{T_j - T_s}{T_t - T_s} \tag{1.3}$$

Aerodynamic recovery factors for thermocouples parallel and normal to the flow direction are reported in the literature to have the following values.[2,7-9] The aerodynamic recovery factor for bare wire thermocouples parallel to the flow direction is given in Equation (1.4) and for orientation normal to the flow direction in Equation (1.5). These values can be used to estimate the measured thermocouple temperature and are strictly functions of thermocouple geometry.

$$\alpha = 0.86 \pm 0.09 \tag{1.4}$$

$$\alpha = 0.68 \pm 0.07 \tag{1.5}$$

Using the isentropic relation between static temperature and total temperature shown in Equation (1.6), Equation (1.3) can be reduced to the relationship in Equation (1.7). This result, for a perfect gas, indicates the temperature at the thermocouple junction directly as a function of total temperature, Mach number of the external flow over the thermocouple M, and the aerodynamic recovery factor α.

$$\frac{T_s}{T_t} = \left(1 + \frac{\gamma - 1}{2} M^2\right)^{-1} \tag{1.6}$$

$$T_j = T_t \left[1 - (1 - \alpha)\frac{[(\gamma - 1)/2]M^2}{1 + [(\gamma - 1)/2]M^2}\right] \tag{1.7}$$

1.1.3 Velocity Error

Velocity error is the manifestation of measurement error due to incomplete conversion of kinetic energy to thermal energy in the boundary layer. This concept was discussed in the previous section and is reliant on the aerodynamic recovery factor α. Measurement error is any measured deviation T_t-T_j between the flow total temperature and the thermocouple temperature. Error due to velocity, E_V, is simply a rearrangement of Equation (1.7).

$$E_V = T_t - T_j = T_t(1 - \alpha)\frac{[(\gamma - 1)/2]M^2}{1 + [(\gamma - 1)/2]M^2} \tag{1.8}$$

The aerodynamic recovery factor α can be used in conjunction with the overall recovery factor R to perform a correction factor correction Δ, discussed in detail by Glawe, Simmons, and Stickney.[8,9] This correction factor Δ is defined in Equation (1.9) and is related to the aerodynamic recovery factor and ratio of static to total temperature. This correction factor is subsequently added to the overall recovery factor definition in Equation (1.1) to give the flow total temperature. This result, combined with the correction definition in Equation (1.9) produces the Mach corrected recovery factor $\overline{R}$ in Equation (1.10).

$$\Delta = (1 - \alpha)\left(1 - \frac{T_s}{T_t}\right) \tag{1.9}$$

$$\overline{R} = R + \Delta = R + (1 - \alpha)\left(\frac{[(\gamma - 1)/2]M^2}{1 + [(\gamma - 1)/2]M^2}\right) \tag{1.10}$$

This recovery factor correction is used to correct for error due to Mach number effects, i.e. velocity.

1.1.4 Conduction Error

Conduction error is the focus of this study, but it has historically received the least in-depth discussion of all error sources. Conduction error is the measurement error due to heat loss via

conduction from the thermocouple junction along its length. Measurement error is any measured deviation T_t-T_j between the flow total temperature and the thermocouple temperature. The historical functional form for conduction error is derived by assuming the thermocouple to be a thin rod subjected to one-dimensional steady heat conduction. This derivation can be found in detail in Eckert and Drake (1959) and Özişik (1977).[10,11] The solution reduces to the form expressed in Equation (1.11).[2] The conduction error is expressed as a function of total temperature, base temperature T_b, the geometry of the thermocouple, and the convective heat transfer h_c at the thermocouple junction. The base temperature is the temperature at the base of the thermocouple junction. The thermocouple geometry is contained in the variables L, d, and k_s which represent the thermocouple immersion length from its base, the thermocouple wire diameter, and the thermal conductivity of the solid, respectfully.

$$E_C = T_t - T_j = \frac{T_t - T_b}{\cosh\left(L\sqrt{\frac{4h_c}{dk_s}}\right)} \tag{1.11}$$

Equation (1.11) shows that conduction error is driven by the temperature difference between the total flow temperature and the base temperature of the thermocouple; this quantity will be normalized on the total temperature to produce a dimensionless conduction driver parameter. This temperature difference can be very large for thermocouples in contact with a cooled structural support. It can be observed that as this temperature difference increases, the conduction error increases for a constant convective heat transfer rate. Furthermore, the conduction error decreases as the argument of the hyperbolic cosine function increases either by increasing the immersion length L or the convective heat transfer h_c, for a thermocouple of set diameter and thermal conductivity. The coefficient of convective heat transfer scales with Reynolds number, i.e. pressure and flow velocity for constant total temperature, thus knowledge of h_c based on the operating regime is an effective parameter for probe design. The probe designer can also choose material of low thermal conductivity and a small wire size within reason, considering durability requirements.[2]

1.1.5 Radiation Error

Radiation error is the measurement error due to heat transfer via radiation to or from the thermocouple and its surroundings. Thermal radiation is the radiative energy emitted by bodies due to their own temperature. Measurement error is still manifested as any measured deviation T_t-T_j between the flow total temperature and the thermocouple temperature. When observing combined radiation and convection heat transfer to a thermocouple, Equation (1.12) is used to calculate measurement error due to radiation. The radiation error becomes predominant at very high temperatures. The error is a function of the form factor K_R, which characterizes the effects of geometry and orientation of surfaces and the resulting radiation heat transfer between them. The emissivity ε of the thermocouple material is challenging to estimate as it is both a function of temperature and material oxidation.[11] The area available for radiation is indicated by A_R and the area available for heat convection is A_c; these two areas are generally equal and can be eliminated from the radiation error calculation. The Stefan-Boltzmann constant is represented by σ.

$$E_R = T_t - T_j = \frac{K_R \sigma \varepsilon A_R (T_j^{\,4} - T_w^{\,4})}{h_c A_c} \tag{1.12}$$

Radiation corrections for thermocouples have been extensively studied.[12-16] Estimation of surface emissivity for various materials has been documented in literature.[17-20] The effect of material oxidation on emissivity for platinum thermocouples was studied by Glawe and Shepard.[21] Oxidation and general exposure to high temperature exhaust streams significantly increases the thermocouple emissivity. Clean, unused probes become more of a "black body" with increasing emissivity, where "black body" is defined to be a perfect emitter and perfect absorber of thermal radiation.

Since the areas available for convection and radiation are equivalent, and the form factor can be taken to be unity if the probe enclosure is large compared to the thermocouple wire diameter, radiation error is primarily driven by material emissivity, surrounding wall temperature, and the convective heat transfer. Using material with low emissivity and controlling the wall temperature is the most effective way of limiting radiation error. Probe design to increase wall temperature closest to the thermocouple generally uses multiple concentric shields around the thermocouple.[4,13,22] The theory behind this design is that each successive shield acquires heat via radiation from the previous shield thus each successive shield is at a higher temperature than the previous shield. The innermost shield temperature, i.e. T_w, is ultimately increased which in turn reduces measurement error due to radiation. Simply adding radiation shields is not always practical, especially if the flow velocity is low.[2]

1.1.6 Transient Error

Transient error arises due to the thermal capacity of the thermocouple material. When the flow temperature is changed, the thermocouple measurement will lag behind the changing flow temperature. Simple analysis of a thermocouple as a one-lump system with convection boundaries can be performed to obtain the transient response. Under the assumption that the thermal conductivity of the thermocouple junction is much greater than the convective heat transfer at the junction, the spatial variation of temperature can be ignored for the purpose of analyzing the junction temperature as simply a function of time.[11] The energy equation results in a balance between heat flow into the thermocouple junction via convection over its surface area A and the rate of increase of the internal energy of the junction, mathematically defined in Equation (1.13).

$$Ah_c\left[T_t - T_j(t)\right] = \rho c_p V \frac{dT_j(t)}{dt} \tag{1.13}$$

Equation (1.13) can be rearranged to the form shown in Equation (1.14). The volume to surface area ratio for a thin rod reduces to be d/4. The time constant for thermocouple junction response is indicated by the variable τ. The time constant is dependent on the material properties and geometry: the density ρ, specific heat c_p, and wire diameter d are critical in defining the thermal capacity of the thermocouple. The convective heat transfer coefficient h_c indicates how much heat addition is occurring at the thermocouple junction.

$$E_T = T_t(t) - T_j(t) = \tau \frac{dT_j}{dt} \ , \tau = \frac{\rho c_p d}{4h_c} \tag{1.14}$$

The mathematical formulation expressed in Equation (1.14) is that which describes a first order instrument.[23] When exposed to an instantaneous change in temperature, i.e. a step function, the junction temperature changes at a rate dependent on its time constant. The time constant is defined to be the time taken for the junction temperature to reach 63.2% of the final total temperature value in this case. The solution to Equation (1.14) is shown in Equation (1.15), where $T_{j,i}$ is the initial junction temperature. Note that when $t = \tau$, $T_j(\tau)$ achieves 63.2% of the temperature from its initial junction temperature and T_t.

$$T_j(t) = (T_{j,i} - T_t)e^{-t/\tau} + T_t \tag{1.15}$$

Reducing transient error is achieved by reducing the characteristic time constant of the thermocouple. This is done by either decreasing the density, specific heat, or diameter of the thermocouple wire, or maximizing the convective heat transfer to the thermocouple. Further governing equations of time response and temperature lag for general bodies subjected to heating or cooling are given in detail by Goodwin.[24] Experimental techniques for determining thermocouple time response are well studied.[25-28] Alternative methods, namely dynamic compensation, are available to improve thermocouple temperature lag.[29]

1.2 Review of Historical Total Temperature Probe Designs

The evolution of total temperature probe design has been well documented.[2,38] The goal of designing total temperature probes is to develop a flow environment around the thermocouple that produces a measurement with acceptable accuracy.[2] The previously discussed analytical models for thermocouple sources of error serve as an effective design guideline for total temperature probes. The overall error is mainly a function of the convective heat transfer and the recovery factor of the thermocouple junction.[2] Producing an environment favorable for convective heat transfer, while maintaining an acceptable velocity error, tends to decrease both the radiation and conduction error for a given conduction driver.

It is necessary to design total temperature probes with a shield around the sensing junction in order to produce a favorable environment around the thermocouple junction. The surrounding shield serves as a stagnation tube to bring the flow to a near stagnation condition. The earliest documented shielded total temperature probe design was created by Franz for temperature measurement in a supercharger.[30] This probe featured a stagnation shield; a thermometer was used for temperature measurement and was placed at the shield inlet where the stagnation point was formed. The thermometer was built into a streamlined body of low thermal conductivity material such that the measurement was not affected by heat conduction. This probe had significant measurement challenges for very turbulent flow where cross-flow around the shield body impacted the stagnation point location.

Franz's first design featured no through flow. He went on to improve this "free stagnation principle" by modifying the shield geometry to allow internal flow through the probe along the

measurement device. This second total temperature probe designed by Franz still featured an inlet diffuser but switched to a through flow configuration using a thermocouple as the sensing device. Vents were added to the back portion of the shield behind the thermocouple junction. The addition of vents allowed flow through the sensor, greatly improving the measurement performance. The temperature sensing location was located entirely within the shield, thus negating the effects of turbulence. The shield design conditions the flow around the temperature sensing junction. Hottel proved that the Franz probe proved to be extremely sensitive to yaw angle due to instability associated with the inlet diffuser.[7] The instability associated with flow through the inlet diffuser was eliminated by simply changing the shield to be of a straight tube geometry.[7] The simple straight tube geometry is shown in Figure 1.2. However, this design featuring a shield with through flow crudely set the framework for future total temperature development. The internal velocity through the probe can be selected using vent area to inlet area ratios for one-dimensional isentropic compressible flow.[31] Subsequent straight tube designs using thermocouples with through flow can be considered a standard configuration in total temperature measurement.[32-35] The design procedure is not rigorous and corrections are required for a suitable design.

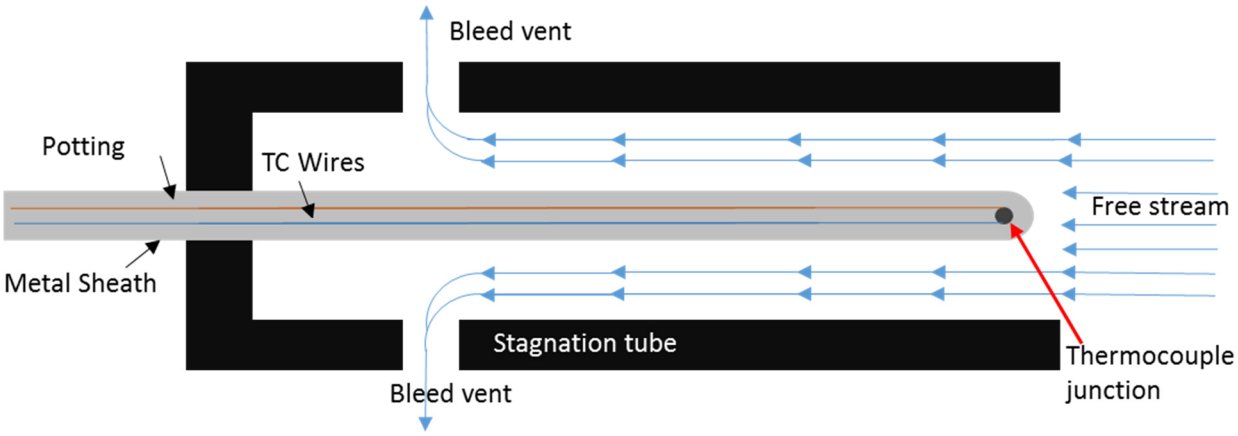

Figure 1.2: Conventional, straight tube total temperature probe design.

Other designs that did not feature a straight tube design with through flow were investigated.[36-38] Probes featuring alternative designs may be required where spatial restrictions inhibit any conventional straight tube geometries. These designs typically have a straight geometry along the thermocouple axis where the thermocouple junction is exposed to the stagnated flow at the end of the shield. Spade tip designs feature a straight tube with a section removed; radial shield material is removed such that the junction is exposed and the shield wall is directly behind the junction. This design produces a stagnant condition on the thermocouple junction. This spade tip design was studied by Beede and Droms[37], and variations of this spade tip design are discussed in Moffatt and Markowski[36]. A schematic for a spade tip design is showed in Figure 1.3. Warren compiles results for numerous probe designs and subsequently develops a probe featuring a conventional, straight tube design.[38]

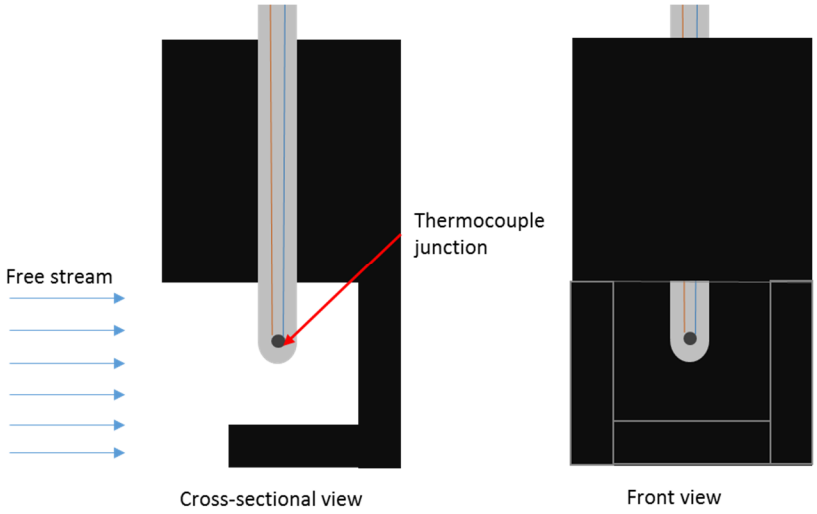

Figure 1.3: Schematic of spade tip total temperature probe design.

An extensive review of the literature reveals the design of probes to limit conduction error. Qualitative observations of conduction error were first made by Hottel and Kalitinsky in 1945 when the Franz style probe was tested with varying thermocouple junction locations. The performance of the probe significantly increased as the distance between the thermocouple junction and the wall was increased; it is believed that this observation indicates the conduction conditions changing.[2] Moffatt and Markowski introduced the analytical model using the hyperbolic cosine for conduction error in 1948, shown in Equation (1.11).[36] The experimental determination of thermocouple time constants and subsequent corrections were first documented by Scadron and Warshawsky in 1952. The method used for calculating conduction error consisted of a theoretical calculation involving combined convective, conductive, and radiative heat transfer from a single wire to calculate a time constant which then lead to a theoretical formulation for steady state conduction and radiation error.[3] This is the first extensively documented source that provides an in depth analytical method for conduction error calculation. Wormser[27] performed work similar to Scadron and Warshawsky by experimentally determining thermocouple time constants and subsequent analytical conduction and radiation corrections. Previous literature shows conduction error corrections of simply using heat transfer models to estimate correction factors.[15,21,25-29].

It is worth noting here the efforts of Rhodes et al.[39] and their numerical modeling of total temperature sensors. This model assumed the sensor to be axially symmetric thus allowing the sensor to be easily discretized into axial cells. The temperature of each cell was obtained from the iterative solution of the time dependent energy equation integrated over each cell. The solution of the energy equation encompasses the convective, conductive, and radiative energy transfer between all cells in the domain. The work of Rhodes et al. provides a method for higher fidelity analysis. Similar work was performed by Zeisberger.[34] An even more in depth modeling technique for total temperature sensors was conducted by Schneider.[43] Complete fluid simulations involving conjugate heat transfer in ANSYS Fluent were performed to determine the temperature distribution within the total temperature sensor.

The current study is important because it experimentally investigates conduction error of cooled total temperature probes and provides a procedure for calibration of this error source. Both analytical and experimental results of total temperature sensor performance under varying conditions are explored, with special interest in characterization of conduction error. The literature yields no earlier experimental determination of sensor performance strictly as a function of conduction error, but rather earlier work emphasizes the design procedure to produce probes that minimize conduction error. This study provides guidelines for the calibration of conduction error and proves conduction error to be governed by dimensionless parameters. Due to this fact, conduction error calibration can be performed in any temperature regime and can be universally used.

The problem at hand and the theory behind thermocouple performance for gas temperature measurement has been discussed. Chapter 2 features the modeling of total temperature probe performance, using both historical methods and a higher fidelity thermal resistance model. The current experimental setup, acquisition procedure, and post processing are discussed in Chapter 3 and basic uncertainties are estimated. Chapters 4 and 5 consist of experimental results and related discussion.

2 LOW-ORDER MODELS

Numerous low-order models have been used to predict sensor performance under various conditions. Low-order models serve a valuable role in quickly predicting qualitative behavior in sensor performance, as opposed to full-scale simulations which take an excessive amount of time to perform. These models are physics-based solutions for simplified sensor geometries, often using empirical correlations from historical experimental data. The effect of dimensionless conduction driver, Reynolds number, total temperature, sensor material, and other parameters are easily studied.

2.1 MOFFAT CONDUCTION ERROR MODEL

Equation (1.11) introduced in section 1.1.4 can be directly used to study the effect of a non-dimensional conduction error on sensor performance. Moffat[2] includes a procedure for estimating sensor error for bare-wire, unshielded thermocouples.

The calculation of the convective heat transfer coefficient depends on the sensor internal Reynolds number. For the following discussion, the Nusselt number needs to be defined. The Nusselt number is defined as the ratio of convective heat transfer to the thermal conductivity of the flow and is calculated in accordance with Equation (2.1). The Reynolds number used is defined in Equation (2.2) and uses freestream flow properties evaluated at the flow total temperature. For an orientation with the thermocouple axis aligned with the flow direction, the Nusselt number scales with the 0.674 power of Reynolds number, indicated by Equation (2.3). This correlation is the result of numerous experimental data sets for bare wire thermocouples.[2] The diameter of the thermocouple wire is used as the characteristic length scale for the Nusselt and Reynolds number.

$$Nu = \frac{h_c d_{wire}}{k_{flow}} \tag{2.1}$$

$$\mathrm{Re} = \frac{\rho U d_{wire}}{\mu} \tag{2.2}$$

$$Nu = 0.085 \cdot \mathrm{Re}^{0.674} \tag{2.3}$$

The coefficient of convective heat transfer can now be estimated using Equations (2.1) through (2.3) yielding the following result.

$$h_c = 0.085 \frac{k_{flow}}{d_{wire}} \mathrm{Re}^{0.674} \tag{2.4}$$

This result for the coefficient of convective heat transfer is now substituted into Equation (1.11).

$$T_t - T_j = \frac{T_t - T_b}{\cosh\left(L\sqrt{\frac{4 \cdot 0.085 k_{flow}\,\mathrm{Re}^{0.674}}{d_{wire}^2\, k_{solid}}} \right)} \tag{2.5}$$

Equation (2.5) can be rearranged into a more suitable form. The squared d_{wire} term can be removed from the radical to produce a dimensionless L/d_{wire}. The numerator of the right hand side will be moved to the left hand side to produce a dimensionless conduction error term E_c as follows:

$$E_c = \frac{T_t - T_j}{T_t - T_b} = \frac{1}{\cosh\left(2 \cdot \frac{L}{d_{wire}} \sqrt{0.085 \cdot \frac{k_{flow}}{k_{solid}}}\,\mathrm{Re}^{0.337} \right)} \tag{2.6}$$

Equation (2.5) can also be rearranged to predict sensor performance as function of dimensionless conduction driver. Rather than normalizing both sides of the equation by the numerator, normalization is made on the flow total temperature T_t.

$$\frac{T_t - T_j}{T_t} = 1 - R = \frac{\frac{T_t - T_b}{T_t}}{\cosh\left(2 \cdot \frac{L}{d_{wire}} \sqrt{0.085 \cdot \frac{k_{flow}}{k_{solid}}}\,\mathrm{Re}^{0.337} \right)} \tag{2.7}$$

Equation (2.7) directly expresses the sensor performance R as a function of dimensionless conduction error $(T_t-T_b)/T_t$ and Reynolds number. The dimensionless conduction driver term is defined to be Θ in Equation (2.8).

$$\Theta = \frac{T_t - T_b}{T_t} = 1 - \frac{T_b}{T_t} \tag{2.8}$$

Observing the two forms of Moffat's model shows that a sensor's conduction error is clearly reliant on Θ, L/d_{wire}, Reynolds number, and the k_{flow}/k_{solid}. The parameter that requires additional investigation is the k_{flow}/k_{solid} parameter. Discussion of this parameter cannot be successfully performed without introduction of the Biot number. The Biot number relates the relative magnitudes of the convective heat transfer coefficient and the internal conductance of the solid. It is very similar to the Nusselt number, though the thermal conductivity is of the solid. The Biot number is expressed in Equation (2.9).

$$Bi = \frac{h_c L}{k_{solid}} \tag{2.9}$$

The characteristic length L in the Biot number calculation is taken to be the ratio of the volume to surface area for a three-dimensional solid; the ratio of area to perimeter is used for a two-dimensional solid. The characteristic length L turns out to be d/4 for a cylindrical rod. The relationship between Biot number and thermal conductivity of the solid has been established, along with the earlier relationship between Nusselt number and thermal conductivity of the flow. Solving Equations (2.1) and (2.9) for the respective thermal conductivities yields the relationship shown in Equation (2.10) between the ratio of the thermal conductivities, with the Biot and Nusselt numbers.

$$\frac{k_{flow}}{k_{solid}} = \frac{h_c d_{wire} / Nu}{h_c d_{wire} / 4Bi} = \frac{4Bi}{Nu} \tag{2.10}$$

Substituting the Nusselt-Reynolds relationship in Equation (2.3) into Equation (2.10) will express the Biot number as a function of the thermal conductivity ratio and Reynolds number.

$$Bi = \frac{k_{flow}}{k_{solid}} \frac{0.085\mathrm{Re}^{0.674}}{4} \tag{2.11}$$

Combining this result into Equation (2.5) will show that the hyperbolic cosine argument is nothing more than the Biot number decomposed into the thermal conductivities of the problem and the Reynolds number. Equation (2.5) can subsequently be rewritten purely as a function the sensor L/d ratio and the Biot number:

$$T_t - T_j = \frac{T_t - T_b}{\cosh\left(2\frac{L}{d_{wire}}\sqrt{Bi}\right)} \tag{2.12}$$

Equation (2.12) indicates that the error due to conduction along the length of a thermocouple is inherently a Biot number problem, with dependence on the sensor geometry parameter L/d_{wire}.

2.2 THERMAL RESISTANCE MODEL

A thermal resistance model was created using an electrical circuit analogy commonly used for steady state heat transfer solutions.[11] This analogy directly relates the rate of heat flow, Q , through a material to the current, I, present in an electrical circuit. The resistance of the electrical circuit is directly analogous to the material resistance to a temperature gradient. Along with the circuit resistance, the electric potential is what drives the steady state solution; the temperature difference serves as the driver for the steady state solution of the thermal resistance model. These relationships are easier to grasp by observing the governing equations. Ohm's law is shown in Equation (2.13) and serves as the fundamental equation relating current, I, across a conductor with resistance $\underline{R}$, experiencing an electric potential V. Fourier's law of heat conduction is shown in Equation (2.14) and serves as the fundamental equation relating heat transfer between two points in a material subjected to a temperature gradient to the material's thermal conductivity, k, through some area A.

$$I = \frac{V}{R} \tag{2.13}$$

$$Q = kA\frac{\partial T}{\partial x} \tag{2.14}$$

Equation (2.14) can be manipulated and put into a form that allows the electric-thermal analogy to be easily viewed. The temperature gradient between two points in a material can be estimated using the temperature difference between the points of interest and the length between them. This result can then be substituted into Equation (2.14). The distance between the two points of interest, Δx, can instead be represented as L. This substitution is done for clarity. This result can be algebraically manipulated to have the same form as Equation (2.13) and is expressed in Equation (2.15).

$$Q = \frac{\Delta T}{\left(\frac{L}{kA}\right)} \tag{2.15}$$

Fourier's law cast in the form shown in Equation (2.15) can now be directly compared to the form of Ohm's law in Equation (2.13). It is easily inspected that the equivalent thermal resistance between two points is represented by the denominator in Equation (2.15), consistent with the resistance in the electrical circuit.

The thermal resistance model consists of a discretized domain of the thermocouple and stagnation tube assembly. The stagnation tube will hereby be referred to as the Kiel head. The domain was discretized into a two node system. The physical system is showed in Figure 2.1 and the axisymmetric discretization is shown with numbered nodes in Figure 2.2.

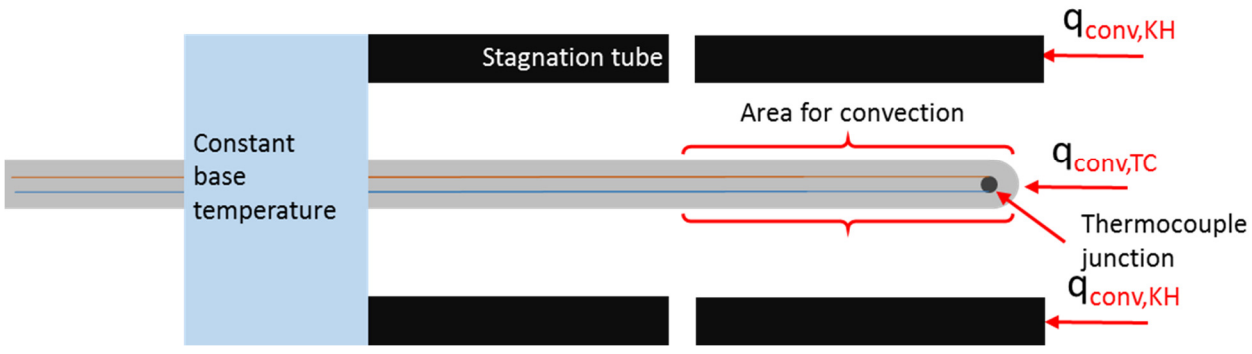

Figure 2.1: Diagram of total temperature probe assembly.

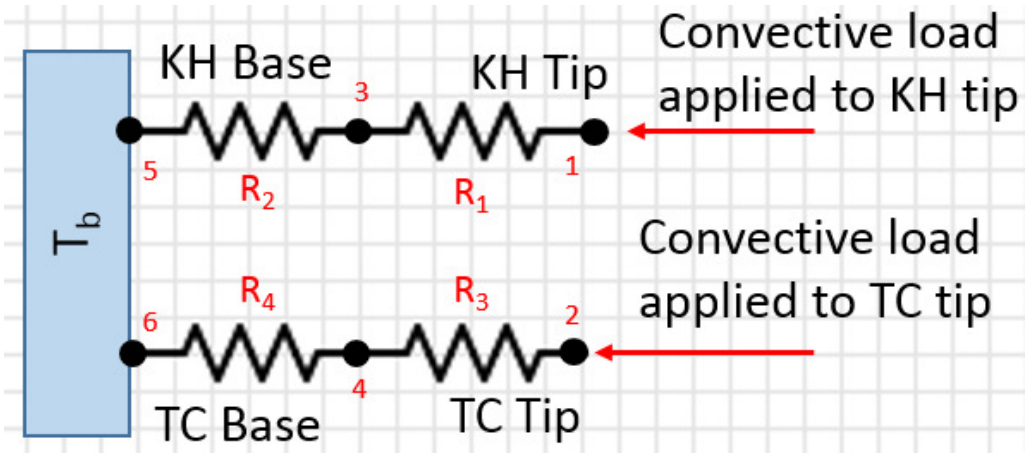

Figure 2.2: Domain discretization of thermal resistance model.

The primary values of interest in this model are the nodal temperatures, namely the temperature of the thermocouple junction represented at node 1. A system of equations is built using Equation (2.14) across each resistance, summing the heat transfer at the central nodes, and applying boundary conditions at the edge nodes 1, 2, 5, and 6. The heat transfer values are summed at the central nodes the same way that current is summed at the nodes of an electrical circuit using Kirchoff's law. The temperature of the base is specified at nodes 5 and 6, while the sources of convective heat transfer are lumped at nodes 1 and 2. The governing equation for convective heat transfer is referred to as Newton's Law of Cooling and is shown in Equation (2.16). The coefficient of convective heat transfer between a fluid and adjacent surface is h. This equation is applied at nodes 1 and 2.

$$Q = hA\Delta T \tag{2.16}$$

There are eight unknowns in this system; the heat transfer value between each node, and the four nodal temperatures. This system of equations is shown in Equation (2.17) and is solved by performing a matrix inversion in Matlab. This inversion gives an analytical expression for the junction temperature in terms of the material thermal resistance, convective coefficients, flow total temperature, and base temperature of the material.

$$\begin{bmatrix} 1 & -1 & 0 & 0 & 0 & 0 & 0 & 0 \\ 0 & 0 & 1 & -1 & 0 & 0 & 0 & 0 \\ 0 & -R_2 & 0 & 0 & 0 & 0 & 1 & 0 \\ 0 & 0 & 0 & -R_4 & 0 & 0 & 0 & 1 \\ -R_1 & 0 & 0 & 0 & 1 & 0 & -1 & 0 \\ 0 & 0 & -R_3 & 0 & 0 & 1 & 0 & -1 \\ 1 & 0 & 0 & 0 & h_{KH} & 0 & 0 & 0 \\ 0 & 0 & 1 & 0 & 0 & h_{TC} & 0 & 0 \end{bmatrix} \times \begin{bmatrix} Q_1 \\ Q_2 \\ Q_3 \\ Q_4 \\ T_1 \\ T_2 \\ T_3 \\ T_4 \end{bmatrix} = \begin{bmatrix} 0 \\ 0 \\ T_b \\ T_b \\ 0 \\ 0 \\ h_{KH}T_t \\ h_{TC}T_t \end{bmatrix} \tag{2.17}$$

The thermal resistance model implements physics previously discussed in Moffat's model, namely the calculation of the convective heat transfer coefficient as a function of the sensor's internal Reynolds number. The Reynolds number used in the calculation of the Nusselt number is for the internal flow through the sensor. Moffat presents a rule of thumb to estimate the internal velocity through a sensor from the freestream velocity. The internal velocity through the sensor, and thus over the thermocouple junction, can be taken to be $1/8^{th}$ of the freestream velocity for a conventional vent-to-inlet area ratio of approximately 20%. This $1/8^{th}$ rule stems from the area-Mach relation for isentropic flow. For calculation simplicity, this scaling factor was instead used to scale the Reynolds number of the external flow by $1/8^{th}$ to be the internal Reynolds number. Once the Reynolds number is calculated using this method, the Nusselt number is calculated. The convective heat transfer coefficient is then calculated from the Nusselt number.

In summary, the thermal resistance model assumes ideal gas behavior and uses a correlation between a scaled external Reynolds number and Nusselt number to estimate the convective heat transfer that the sensor is subject to. The steady state conduction solution is calculated using an electrical circuit analogy where the sensor material has thermal resistance analogous to a resistor in an electrical circuit. The sensor and the Kiel head are composed of the same material. Fidelity is added to the model with flow conductivity and material properties changing as a function of temperature. Further fidelity is added with the inclusion of an equivalent conductivity factor for the sensing thermocouple. The internal thermoelements, thermocouple sheath, and thermoelement potting material are lumped together into a single thermal conductivity. The thermal resistance model requires inputs for total temperature, Mach or Reynolds number, and conduction driver. Remaining input are used for specifying sensor geometry details. The model outputs the recovery factor of the sensor.

2.3 PARAMETRIC STUDIES USING LOW-ORDER MODELS

Important parameters for sensor performance were introduced and discussed earlier in the introduction. The previously described Moffat model and the thermal resistance model are used to predict the impact of Reynolds number, conduction driver, and thermocouple L/d on sensor performance. The impact of the Biot number will first be presented.

2.3.1 Impact of Biot Number and Sensor L/d

Moffat's model in the form of Equation (2.12) can be arranged to give the dimensionless conduction error strictly as a function of L/d and Biot number by dividing both sides by (T_t-T_b). Recall that the Biot number is effectively the ratio of the convective heat transfer rate to how quickly a body conducts heat. The parameter is necessary for determining the balance between convective and conductive heat transfer. The indicated temperature of the sensor is a heat transfer balance between all error sources; convective errors scale with flow velocity and conductive errors scale with the temperature gradient through the material of the sensor. How well a solid resists temperature change due to heat loss through conduction versus how well heat is transferred from the flow to the solid completely driver sensor performance. It should be clear to the reader that maximizing heat transfer to the sensor from the flow via convection and reducing conduction heat transfer from the measurement junction across the length of the sensor is most desired for optimum sensor performance. This is easiest said as maximizing convective heat transfer to the sensor and

minimizing the thermal conductivity of the sensor for a given driver temperature difference. This statement implies that keeping the Biot number as high as possible is desired. Due to the fact that the thermal conductivity of air is magnitudes lower than thermal conductivities of solids, the Biot number will be extremely small, generally on the order of 10^{-5} to 10^{-2}. The effect that this range of Biot numbers has on dimensionless conduction error is shown in Figure 2.3. Increasing the Biot number has the effect of increased convective heat transfer which ultimately decreases the conduction error of the sensor. The importance of the observation cannot be overstated; conduction error decreases as the Biot number increases. The error strongly scales with the convective heat transfer rate. Another observation to be made in Figure 2.3 is the effect of the sensor L/d ratio. It is easily seen that maximizing this parameter also decreases conduction error; this phenomena will be later discussed.

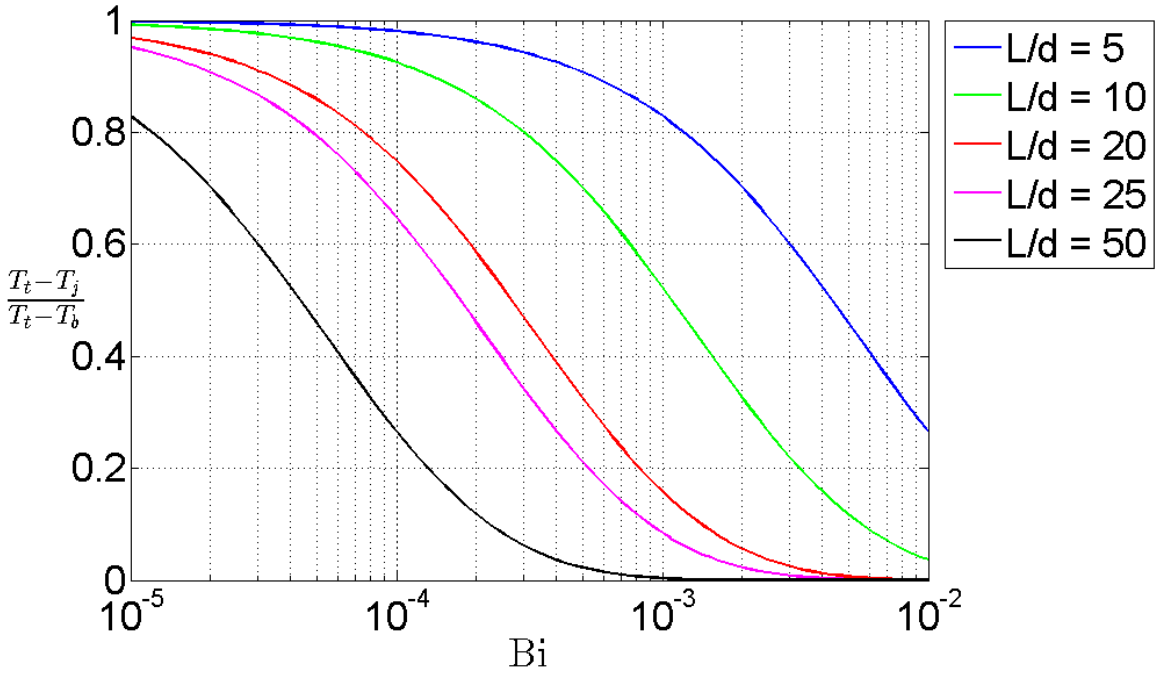

Figure 2.3: Effect of Biot number on dimensionless conduction error using Moffat's model

2.3.2 Impact of Reynolds Number

Both Moffat's model and the thermal resistance model use a Nusselt number to Reynolds number correlation. This correlation is explicitly for unshielded thermocouples aligned with the flow direction. It is evident from this correlation that the convective heat transfer coefficient, h_c, scales with the 0.674 power of Reynolds number. Therefore the Reynolds number is ultimately impacting the heat convection, which in turn directly impacts the sensor performance. The heat convection boundary conditions are introduced into the thermal resistance model at the thermocouple junction and the Kiel head. The heat convection between the freestream flow and the Kiel head, as well as the heat convection between the thermocouple junction and the internal flow through the sensor directly impact the sensor performance.

Study of the impact of Reynolds number was also performed with the thermal resistance model using a total temperature of 550 °F and a moderate conduction driver value of 0.3. The L/d was set to 18 and the ratio k_{flow}/k_{sheath} was set to 0.00225, which is representative of an Inconel sheathed thermocouple. Recall that sensor performance is expressed as the recovery factor; a recovery factor of 1.0 indicates that the sensor perfectly measures the total temperature of the flow. Figure 2.4 illustrates the effect of Reynolds number on the sensor's performance for this particular set of inputs. The prediction from Moffat's model is also included. The legend clearly shows the red curve to be Moffats; the TRM stands for thermal resistance model. Given the previous discussion of Reynolds number and heat convection, it is seen that the effect of convection clearly impacts the sensor performance. At low Reynolds number, i.e. low convection, the effect of conduction error is dominant and decreases the indicated sensor measurement.

The thermal resistance model is not capable of explicitly separating conduction error effects from Reynolds number effects, but allows easy comparison between the two effects. At low Reynolds numbers where the convective heat transfer is low, the conductive heat transfer dominates the sensor performance. At high Reynolds numbers where the convective heat transfer is higher, the effect of the conduction error is not nearly as noticeable, with the sensor performance still increasing, however at a slower rate. In summary, it is expected that the Reynolds number plays a crucial role in reducing the effect of conduction error. This is due to the increased convective heat transfer that occurs at higher Reynolds number.

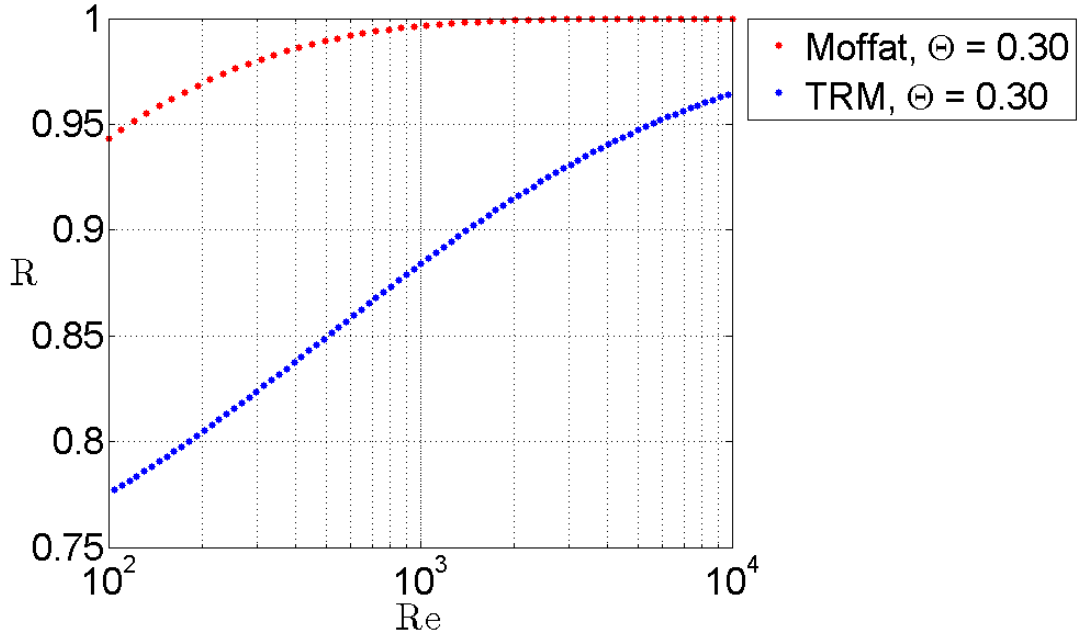

Figure 2.4: Predicted effect of Reynolds number on sensor performance, L/d = 18, k_{flow}/k_{sheath} = 0.00225.

2.3.3 Impact of Conduction Driver

It is necessary to use the thermal resistance model to preliminarily and easily study the effect of conduction error on sensor performance. Recall the fundamental statement that a sensor is subject to conduction error when a temperature gradient along the sensing element is present. The

temperature gradient is imparted into the sensing element from the direct thermal contact between the sensing element and its immediate base support. The magnitude of the temperature difference between the base support and the measuring junction of the sensing element is technically what drives the conduction error of the sensor. It is important to normalize the magnitude of this temperature difference by the total temperature such that the relative strength of the conduction driver can be determined. For example, a temperature difference of 500 °F between the base support and the measuring junction with a total temperature of 800 °F is going to be a much stronger conduction driver than if the total temperature was instead 2000 °F.

Figure 2.5 shows the effect of various conduction drivers, Θ, for a single total temperature over a range of Reynolds numbers using the thermal resistance model. Curves from Moffat's model are included. The total temperature was set to be 550 °F. It goes without saying that the sensor performance decreases as the conduction driver increases. The temperature gradient increases as the conduction driver increases thus reducing the indicated junction temperature of the sensor. For the case of Θ = 0.1, the effect on sensor performance is small at just about a 2% difference in measure of the total temperature between the highest and lowest Reynolds numbers. The sensor performance is further impaired as Θ increases. For the case of Θ = 0.5, the difference is increased to 8% of the total temperature. This is an expected result. As the conduction driver increases, the sensor performance is negatively affected. What follows is discussion of the regime where conduction error dominates sensor performance.

Inspection of Figure 2.5 indicates a recovery roll-off at low Reynolds numbers. Recall the previous discussion of the effect of Reynolds number in section 2.3.2. This discussion is strengthened by inclusion of weaker and stronger conduction drivers than the Θ = 0.3 that was presented in section 2.3.2. Note that the convective heat transfer rate stays constant for a particular Reynolds number.

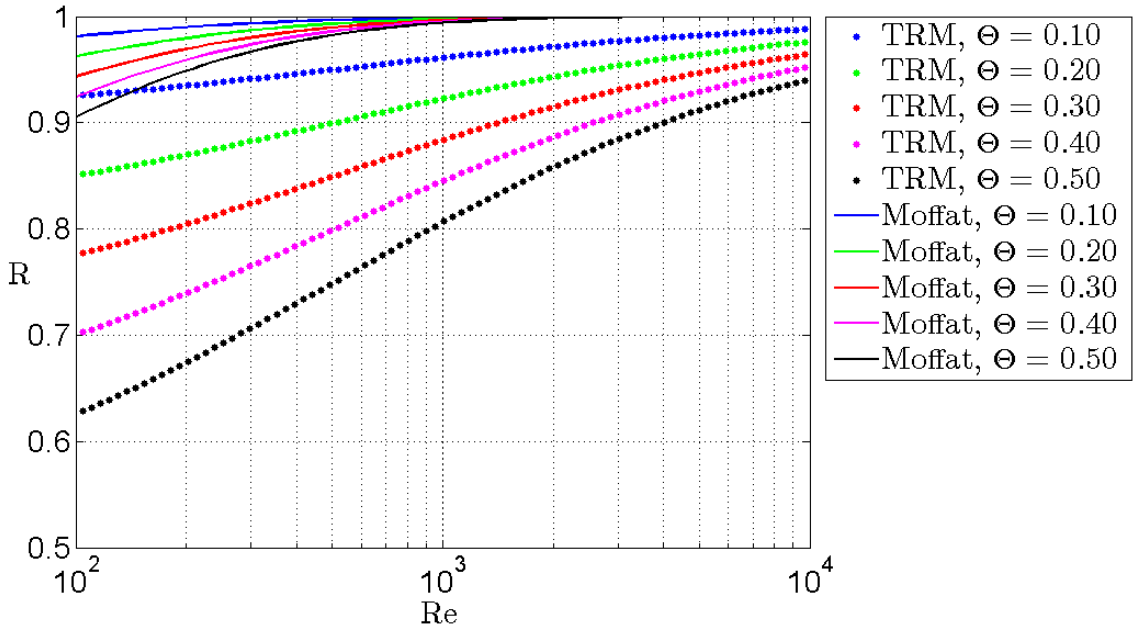

Figure 2.5: Effect of conduction driver on sensor performance, L/d = 18, k_{flow}/k_{sheath} = 0.00225, T_t = 550 °F.

2.3.3.1 The Effect of Sensor L/d on Performance via Conduction Error Minimization

From literature, the standard practice in total temperature probe design is to maximize the distance between the base support and the sensing junction. This distance is then normalized on the diameter of the sensor to provide a dimensionless parameter that is a measure of sensor L/d. It is desired to maximize the sensor L/d in order to reduce the measurement error due to conduction. Increasing the length between the base support and the sensing junction directly decreases the strength of the temperature gradient. The temperature gradient is decreased due to two primary factors that arise from increasing a sensor's L/d: decreasing the conduction driver raises the measured temperature thus decreasing the magnitude of the temperature difference across the sensing element. This coupled with the increased distance between base and junction further decreases the strength of the temperature gradient. Reducing the temperature difference and increasing the distance effectively decreases conduction error since the temperature gradient is mathematically defined as a temperature difference between two points divided by the distance between the two points.

Moffat's model shown in Equation (2.6) is first used to determine the effect that the sensor L/d has on the dimensionless conduction error $(T_t-T_j)/(T_t-T_b)$. The result of increasing a sensor's L/d ratio is seen in Figure 2.6. The conduction error decreases as the L/d ratio is increased. The conduction error also approaches zero as the Reynolds number approaches infinity due to the increase in convective heat transfer. The value of k_{flow}/k_{sheath} is kept constant at 0.00225.

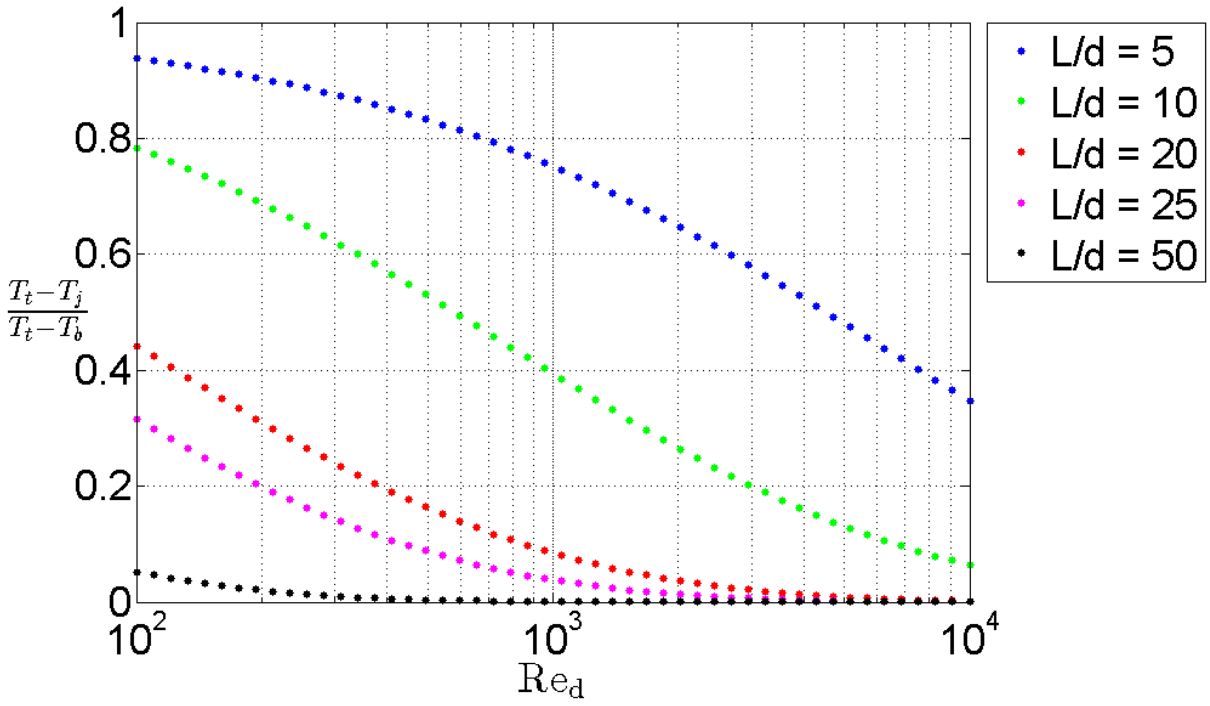

Figure 2.6: Effect of sensor L/d on sensor performance using Moffat's model

Figure 2.6 shows the same characteristic as Figure 2.3, but is cast in the form of Reynolds number. Recall that Biot number is assumed related to Reynolds number by Equation (2.11). Given that the data presented has a thermal conductivity ratio of 0.00225, The Reynolds number range shown in Figure 2.6 is equivalent to a Biot number range of 0.001065 to .02374 in Figure 2.3. These two

figures are not mutually exclusive, but rather present the performance trend in terms of a conventional, easily understood Reynolds number versus the less familiar Biot number. The problem at hand is primarily a Biot number problem, but the Biot number relies on the Reynolds number for convective heat transfer.

The thermal resistance model was also used to study the impact of the sensor L/d on performance for a fixed length thermocouple and a 0.055 in. inlet diameter, 0.5 in. length Kiel head at Mach 0.7 with $\Theta = 0.3$ and $T_t = 1000$ °F. These input conditions used a static pressure of 90 kPa, resulting in a Reynolds number of 6200; note that the characteristic length scale used is the inlet diameter. Platinum was used as the material for both the Kiel head and thermocouple in this example. The L/d was varied from 15 to 50. The sensing junction kept a constant distance from the inlet to the Kiel head. The length of the thermocouple was prescribed as a constant and the diameter was adjusted as L/d was adjusted. The thermocouple diameter was decreased as the L/d was increased since these parameters have an inverse relationship.

Figure 2.7 contains the results for this L/d study. Given that all inputs except sensor L/d were held constant, it is evident that sensor performance is improved when the L/d is increased. For the simulated scenario, about 90% of the total temperature is recovered at L/d = 50 versus just 80% of total temperature recovery at L/d = 15. This performance increase is acquired through the reduction of conduction error.

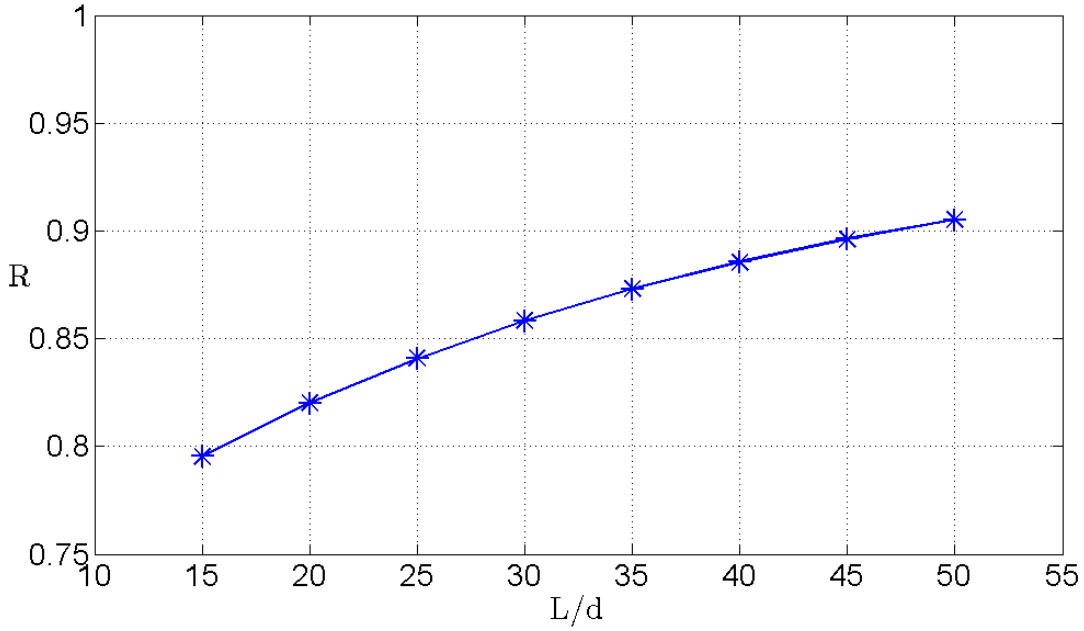

Figure 2.7: Effect of sensor L/d on sensor performance using thermal resistance model, $\Theta = 0.3$

It is important to note that simply increasing a sensor's L/d is not always a viable solution. Sensor durability is greatly impacted when the length gets too long or the diameter gets too small. Increasing the length too far raises the risk of the sensing element drooping and not staying aligned with the flow. Even worse, the sensing element has an increased risk of drooping too far and touching the internal Kiel head surface. High temperature total temperature probes are typically

used in extreme conditions where sensor contamination occurs due to chemical effects of hot gases.4 In general, decreasing sensor diameter adversely affects the useful service life of the sensor. The sensor durability must be taken into account for the design of a satisfactory sensor design.

2.3.3.2 Effect of Sensor Material on Conduction Error

Moffat's model shown in Equation (2.7) is used to determine the effect of sensor material on sensor performance. The primary effect that the sensor material has on performance is its thermal conductivity. Fourier's law of heat conduction, shown in Equation (2.14) indicates that the thermal conductivity, k, directly affects the heat transfer through the sensor. The material of the sensor is directly used for the value of k_{solid}. Three materials with greatly varying thermal conductivities were explored. Copper, platinum, and Inconel were the materials of choice, with thermal conductivities of 400 W/m/K, 72 W/m/K, and 18 W/m/K, respectfully. These materials resulted in k_{flow}/k_{sheath} values of 0.0001245, 0.0007, and 0.00225, respectfully.

The thermal resistance model used the same input conditions that was used for the L/d study in section 2.3.3.1. The only parameter that was changed was the thermal conductivity of the sensor. Recall that the thermocouple sheath and the Kiel head are taken as composed of the same material. The results of changing the material thermal conductivity are illustrated in Figure 2.8. Decreasing the thermal conductivity of the sensor increases the sensor performance by further attenuating the heat transfer due to conduction. Increasing the thermal conductivity increases the conductive heat transfer from the base support to the sensor which decreases the indicated junction temperature. This observation that low thermal conductivity improves sensor performance agrees with past studies. [2,6,37]

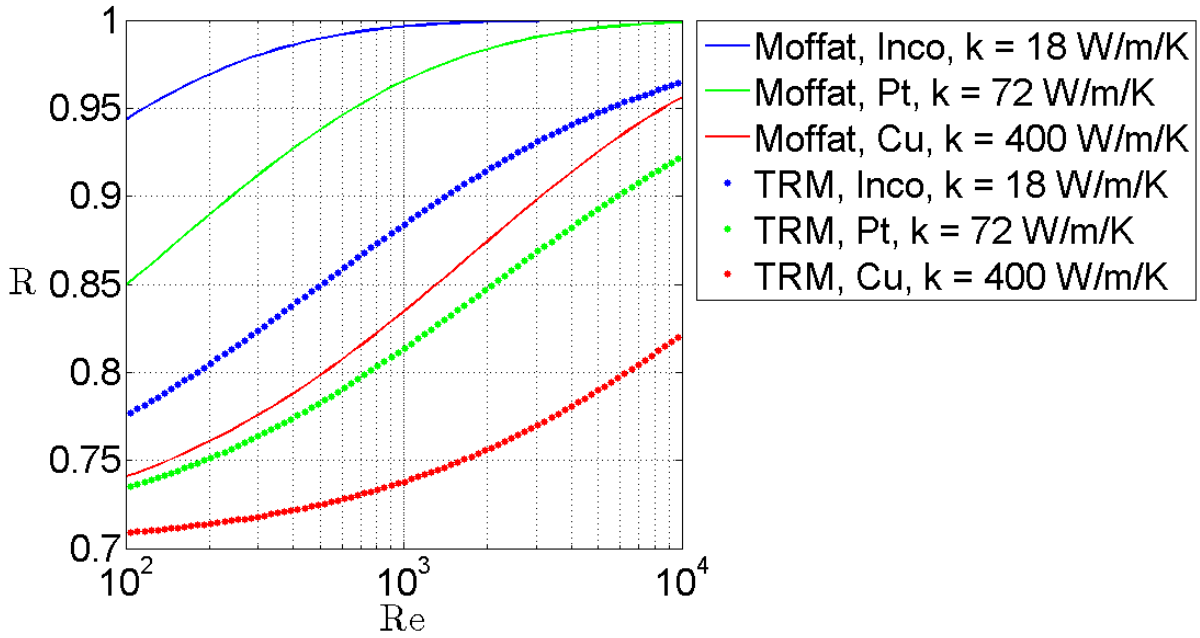

Figure 2.8: Effect of sensor material on performance

2.3.4 Comparison between the Moffat Model and Thermal Resistance Model

From a quantitative standpoint of the sensor performance studies presented in sections 2.3.2 and 2.3.3, the results between Moffat's model and the thermal resistance model are distinctly different. From a qualitative standpoint, both models predicted all of the same trends in sensor performance. The differences stem from the fact that Moffat's model assume a single, standalone thermocouple with a bare-wire junction. The thermal resistance model is modeling a stagnation tube and sheathed thermocouple assembly using the same physics that Moffat's model uses. This difference in problem geometry is what is driving the often large quantitative differences between Moffat's model and the thermal resistance model.

2.3.5 Limitations of the Thermal Resistance Model

Since this model features heat transfer completely due to conduction, with convection boundary conditions applied at the sensor inlet, the sensor performance most heavily rely on the temperature difference between the sensor base and the flow total temperature. If there is no temperature gradient within the sensor, i.e. no conduction error, the sensor is predicted to have perfect performance with a unity recovery factor. Of course, this is not physically correct as there are also errors due to velocity and radiation in a real sensor. This model specifically explores the effect of conduction on the sensor performance, thus the sensor performance converges to a perfect recovery as the conduction error is driven to zero. Though a conduction error must be present in the sensor for the model to be useful, the study of conduction error is isolated in this model without regard to errors due to velocity and radiation effects.

Another limitation of the model is its dependence on the problem geometry. As certain geometries get particularly small and approach zero, the thermocouple wire diameter for example, the numerical calculations performed for segment resistances approach infinity thus pushing the heat transfer through the sensor to zero. Additionally, the calculations for the convective heat transfer coefficient will approach infinity as the wire diameter approaches zero. For the purpose of effectively using this model to predict sensor performance, sensor geometry should be appropriately sized to ensure that erroneous predictions are not made due to numeric singularities.

2.3.6 Moffat's Model Functional Form and Thermal Resistance Model Results

Moffat's model stems from the historical functional form for conduction error, which is from a heat transfer solution in the form of the fin equation.[2,6] This equation was presented earlier in Equation (1.11). It is necessary to determine how effective the historical functional form of conduction error explains the results from the thermal resistance model.

The historical functional form can be recast into purely a function of conduction driver and Reynolds number the same way that Moffat's model was reduced to Equation (2.7). Modifications will be made to this equation to put it into a suitable form to perform a statistical fit of the thermal resistance model results. The entire argument of the hyperbolic cosine that is associated with sensor geometry and sensor material can be absorbed into some constant coefficient c_2 times $Re^{0.337}$. This c_2 constant is theoretically equivalent to $2\frac{L}{d}\sqrt{0.085\frac{k_{flow}}{k_{sheath}}}$. An additional constant, c_1, is added to the numerator to scale the overall model. The closer c_1 is to one, the more effective

this functional form is at describing sensor performance as a function of Reynolds number and driver. The c_1 constant is theoretically equivalent to 1. Equation (2.18) is the functional form that is used to express the sensor performance, R, in terms of the conduction driver, Θ and Reynolds number Re.

$$R = 1 - \frac{c_1 \Theta}{\cosh\left(c_2 \mathrm{Re}^{0.337}\right)} \tag{2.18}$$

The surface described by Equation (2.18) was applied to numerical data obtained using the thermal resistance model. The primary measure of merit are the statistics associated with the surface fit. The Matlab built in function "fittype" was used to define the surface fit functional form. The conduction driver values, Reynolds numbers, and Mach corrected recovery factors were passed as a set of 3-dimensional vectors. The surface fit coefficients were thus obtained for each sensor.

Results were obtained for a conventional total temperature sensor with an L/d of 18 with an Inconel sheathed thermocouple and an Inconel stagnation tube. The stagnation tube had a 0.08 in. outer diameter and 0.0595 in. inlet diameter, with the bleed holes located 0.193 in. from the stagnation tube inlet. The total temperature was set to 1000 °F and the conduction driver was varied from 0 to 0.5 with the Mach number ranging from 0.1 to 0.8. The Reynolds number was subsequently calculated from these inputs.

.Table 1 lists the surface fit coefficients and a few statistical parameters expressing the goodness of fit that the historical functional form of conduction error has when applied to the thermal resistance model results. 95% confidence intervals are included with each fit coefficient. The root-mean-square (RMS) error represents the square root of the sum of the squares of the deviation between the predicted sensor performance by the thermal resistance model and the surface fit. The RMS error can be taken to be a measure of how accurately the surface fit represents the data from the thermal resistance model. This parameter is showing that sensor performance estimated from the surface fit is generally within 0.17% of the flow total temperature that was predicted by the thermal resistance model. The L_∞ norm is the largest deviation between the data set from the thermal resistance model and the surface fit. This indicates that the maximum deviation between sensor performance estimated from the surface fit is 0.43% of the flow total temperature that was predicted by the thermal resistance model. The final statistical parameter of interest in determining the effectiveness of using the historical form for conduction error as the functional form for a surface fit is the coefficient of determination, indicated in the table as R-sq. The coefficient determination is a measure for how well the data set is represented by a statistical model. In this case, the statistical model presented in Equation (2.18) explains 99.79% of the variance in sensor performance. Given the statistical parameters shown in .Table 1, the historical functional form for conduction error serves as an effective statistical model for the sensor performance results calculated by the thermal resistance model.

Recall the theoretical value of c_1 to be one and the theoretical value for c_2 to be $2\frac{L}{d}\sqrt{0.085\frac{k_{flow}}{k_{sheath}}}$. The actual value for c_1 is 37.3% lower than the theoretical value of one. Scaling of the correction factor $\Theta/\cosh(c_2\mathrm{Re}^{0.337})$, indicates that the total temperature sensor geometry and material that the

low-order model uses is not as sensitive to conduction error as the analytical solution for conduction error suggests for an exposed thermocouple. The actual value for c_2 is 79.5% lower than the theoretical value of 0.554. The L/d value used by the model is approximately 18, while the k_{flow}/k_{sheath} value is equal to 0.00279 at 1000 °F. The difference between the theoretical and actual values for the fit coefficients stems from the fact that the heat transfer solution that yields the functional form in Equation (2.18) is for an unshielded thermocouple. Additionally, the large difference between theoretical and actual values for c_2 may be explained by the assumed boundary conditions in the formulation of the heat transfer solution for an exposed thermocouple. Recall that this formulation assumed the convective heat transfer at the tip of the thermocouple junction to be negligible when compared to the convective heat transfer over the entire thermocouple. The low-order model, as well as the sensors experimentally tested, contain a shield that serves the purpose of stagnating the flow around the thermocouple junction.

.Table 1: Summary of surface fit result using functional form expressed in Equation (2.18)

RMS Error	R-sq	L_∞ Norm	Fit constant c1	Fit constant c2
0.0017	0.9979	0.0043	0.6264 +/- 0.0026	0.1142 +/- 0.0015

2.4 THERMAL RESISTANCE MODEL VERIFICATION

Sensor performance predictions were obtained for the geometry of sensor 2 over a range of conduction drivers, Reynolds numbers, and total temperatures. It is necessary to find an appropriate form to represent the data such that the physics of the problem are effectively captured. Previous discussion indicates that sensor performance is primarily a function of both Reynolds number and conduction driver.

2.4.1 Reynolds Number and Conduction Driver

The effect of total temperature has not been discussed yet. Results should be independent of total temperature since both sensor performance and conduction driver is normalized by total temperature. This statement must be proven; the thermal resistance model was ran using total temperatures ranging between 550 °F and 1000 °F across a range of Reynolds numbers. The conduction driver Θ maintained a constant value of 0.3 for this study.

The independence of sensor performance from total temperature value is shown in Figure 2.9. Low order sensor performance predictions can be distinctly estimated in terms of just Reynolds number and conduction driver; the value of the total temperature does not matter. There is one small caveat to this statement that makes the solution not completely independent of the total temperature. The total temperature of the flow is used to calculate material thermal conductivity as well as flow parameters such as viscosity, the specific heat ratio, and density. The effect that the flow total temperature has on the sensor performance due to these property calculations can be taken to be negligible; these effects are dwarfed compared to Reynolds number and conduction effects.

Figure 2.9 serves as a verification of the thermal resistance model. The results presented in this figure show that when the sensor geometry is constant, sensor performance, i.e. recovery factor, depends on just two parameters: the dimensionless conduction driver Θ and the Reynolds number. This is the same form that is presented in the heat transfer solution for a standalone thermocouple in Equation (2.7). This verification proves the validity of the thermal resistance model predictions for total temperature sensor performance. The results from this slightly higher fidelity model reach the same conclusion as the historic characterization of conduction error.

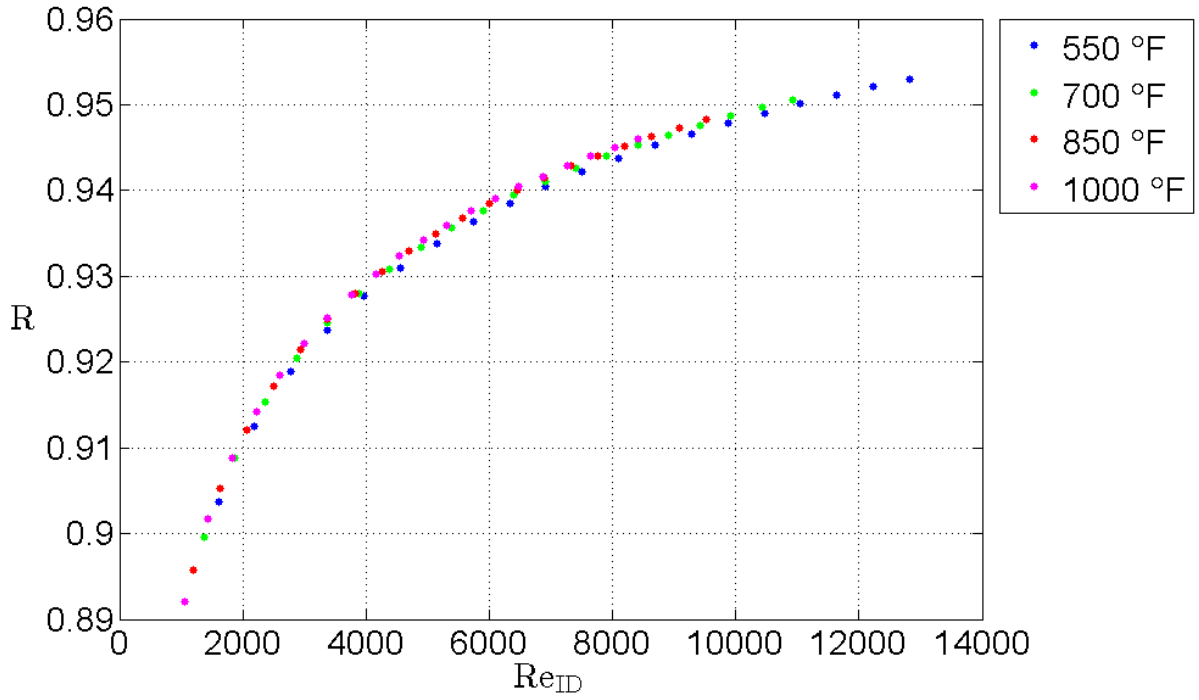

Figure 2.9: Independence of total temperature on low order data collapse for platinum sensors, Θ = 0.3

3 EXPERIMENTAL SETUP AND INSTRUMENTATION

This section is devoted to a discussion of the experimental setup, instruments used, sensors tested, and data acquisition procedure. An experimental rig was developed that allowed variation of sensor conduction driver. All experiments were performed using the Virginia Tech Hot Jet facility. After setting this experimental framework, the post processing procedure is discussed in detail. Significant amount of post processing was required to convert the raw data into its final values.

3.1 TOTAL TEMPERATURE SENSORS

Total temperature sensors tested all used 0.032 in. diameter sheathed, ungrounded thermocouples as the sensing element. Duro-Sense Corporation supplied 12 in. long Type K thermocouples with miniature connectors. Miniature connectors were required because stripped leads were much too small and sensitive to work with. The Type K thermocouples have an Inconel sheath and Chromel-Alumel wire. Chromel is a 90% nickel, 10% chromium alloy that serves as the positive leg of the thermocouple. Alumel is a 95% nickel, 2% manganese, 2% aluminum, and 1% silicon alloy that serves as the negative leg of the thermocouple.

A thermocouple reading is most dependent on the temperature at its junction. The flow most be brought to a stagnation in order to effectively measure the total temperature. To do this, stagnation tubes, also known as Kiel heads, were constructed to fit around the thermocouple. A conventional design was used for the Kiel head manufacturing. The Kiel head features a 0.080 in. outer diameter, 0.06 in. inner diameter, and a 45° inlet chamfer. The inlet chamfer creates a favorable pressure gradient when bringing the free stream flow to a stagnation condition. The vent area was set to be 20% of the inlet area. The vents consisted of four holes 90° radially spaced at a distance 0.18 in. from the Kiel head inlet. The vents were set to be this close from the leading edge to avoid any potential venting jets interfering with the flow around the mounting strut. The Kiel heads were constructed out of 303 stainless steel and have an overall length of 0.58 in. A drawing of the designed Kiel head is shown in Figure 3.1.

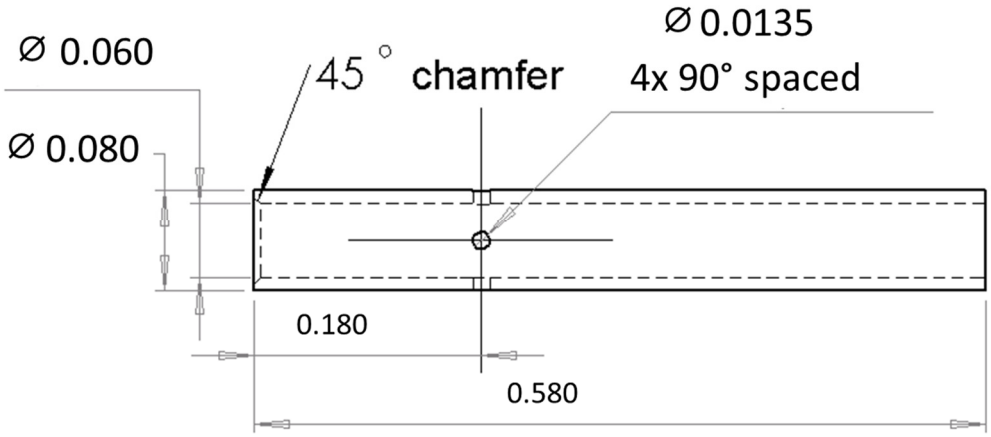

Figure 3.1: Sensor 1 Kiel head design, dimensions in inches

Sensors manufactured by Cleveland Electric Laboratories were additionally tested. These are designated as “sensor 2”. The geometry and features of this professionally manufactured sensor is proprietary. These sensors use a Type B thermocouple to perform temperature measurements. Type B thermocouples consist of two platinum-rhodium legs. The positive leg is a platinum-30% rhodium alloy, and the negative leg is a platinum-6% rhodium alloy. The thermocouple sheath is also composed of platinum-30% rhodium. It is important to state that sensor 2 features large regions of thermal contact between the thermocouple and the Kiel head, which greatly affected how heat is transferred via conduction.

There are numerous differences between these two total temperature sensors. The internal Kiel head geometry is significantly different between sensor 1 and sensor 2. Sensor 1 features no thermal contact between the Kiel head and the thermocouple. The Kiel head and thermocouple only share thermal contact with the strut that they are embedded into. Sensor 2 features direct thermal contact between the Kiel head and thermocouple at the base of the sensor. Furthermore, sensor 1 is composed of a stainless steel Kiel head and an Inconel sheathed thermocouple, both with thermal conductivities around 18 W/m/K. Sensor 2 is composed of a platinum alloy Kiel head and platinum alloy sheathed thermocouple. The thermal conductivity of the platinum is about 72 W/m/K. Table 2 lists the differences between each sensor.

For the purposes of this study, sensor 1 served primarily as a sensor to test and validate the experimental setup and data acquisition procedure before obtaining calibrations for sensor 2. Measurements are significantly easier to obtain with the sensor 1 due to the higher sensitivity of Type K thermocouples. Type K thermocouple sensitivity, and all other thermocouple sensitivities, are function of temperature. The expected voltage signal level for a Type K thermocouple at 550 °F is about 11.8 mV with a sensitivity of 22.7 µV/°F, while the signal level for a Type B thermocouple at this condition is about 0.4 mV with a sensitivity of just 1.67 µV/°F, referenced from 0 °C. The expected voltage signal level for a Type K thermocouple at 850 °F is about 18.5 mV still with a sensitivity of 22.7 µV/°F, while the signal level for a Type B thermocouple at this condition is about 1 mV with an improved sensitivity of 2.8 µV/°F. Due to this drastic difference in signal levels, the Type B measurement is much more challenging than the Type K measurement. Thus sensor 1 was tested thoroughly for validation.

Table 2: Physical Characteristics of Tested Total Temperature Sensors

	Sensor 1	**Sensor 2**
Kiel Head outer diameter (in.)	0.08	0.08
Kiel Head inner diameter (in.)	0.06	0.065
Kiel Head length (in.)	0.58	0.58
Kiel Head material	303 Stainless steel	Platinum
Thermocouple diameter (in.)	0.032	0.032
Thermocouple sheath material	Inconel	Platinum-Rhodium
Thermocouple type	“K”	“B”
Nominal sheath conductivity	18 W/m/K	72 W/m/K

3.2 VIRGINIA TECH HOT JET FACILITY

The facility used in this study is the Virginia Tech Hot Jet. The facility operates using compressed air from an Ingersoll-Rand Type 4-HHE-4 4-stage reciprocating air compressor that pressurizes two reservoir tanks with a volume of 23 m^3 up to 300 psi. The air from the compressor is passed through a dryer to remove moisture before being heated. The hot jet facility uses a Sylvania 192 kW Flanged Inline Heater, Model 073153. The jet rig features several layers of screens and honeycomb to condition the flow. The jet contracts from a 4 in. duct at the plenum section to a 2 in. nozzle exhausting to room ambient. The 2 in. nozzle features 6 equally radially spaced threaded holes that allow converging/diverging nozzles to be rapidly installed for supersonic studies. For the purposes of this study involving high subsonic speeds, only the 2in. converging nozzle is used. The subsonic, hot flow characteristics of this facility have not been previously studied. The jet facility is shown in Figure 3.2.

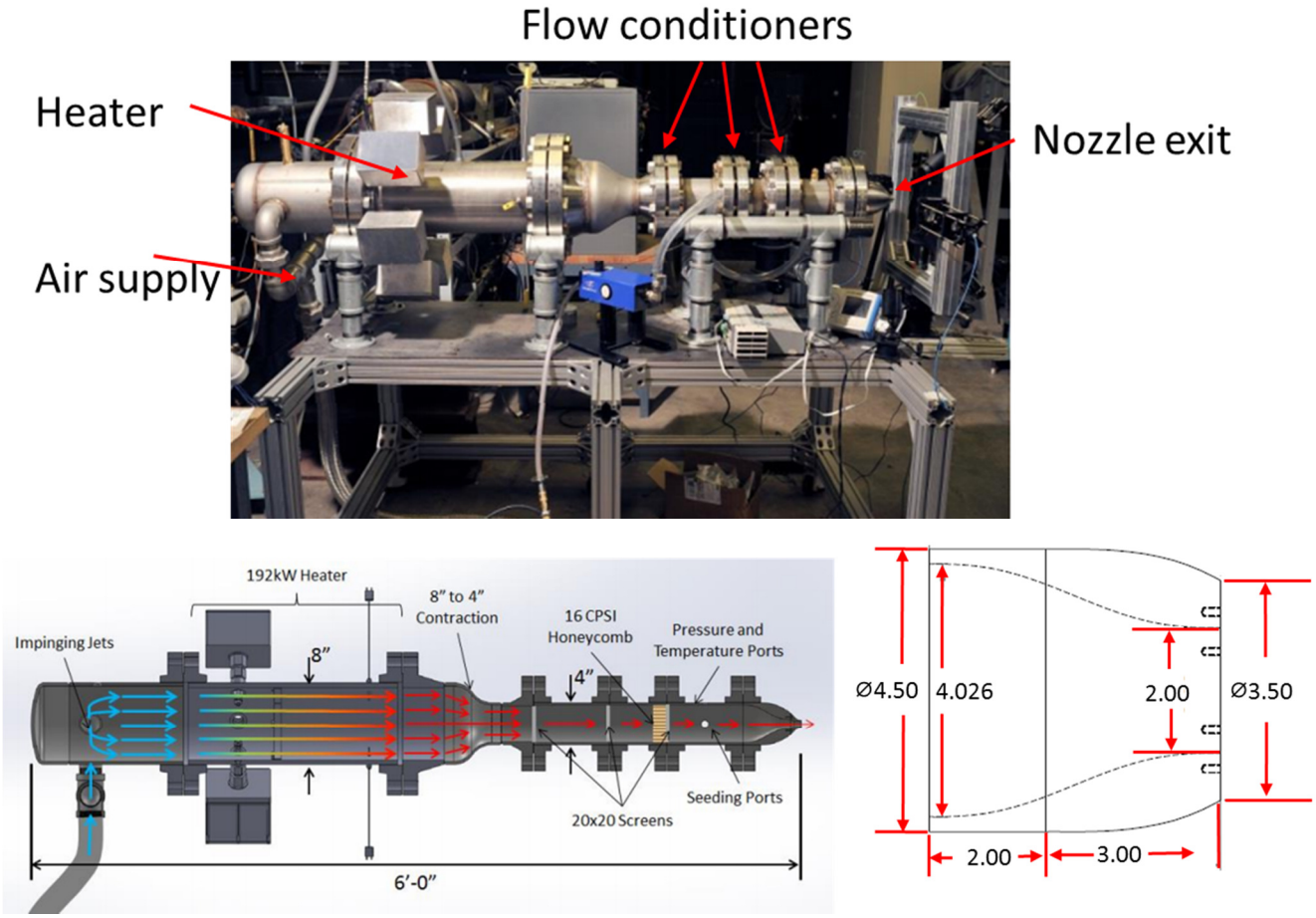

Figure 3.2: (Top) Virginia Tech Hot Jet Facility. (Bottom left) Detailed facility schematic. (Bottom right) Nozzle contour, dimensions in inches.

The total pressure of the flow is measured upstream in the jet plenum with a Pitot probe. The jet exhausts to ambient conditions where the static pressure is the local atmospheric pressure. This atmospheric pressure was consistently about 1 atm for all data acquired. The current study involves the experimentation of total temperature sensors over a range of temperatures and conduction

drivers. It is paramount to understand and characterize the heater operation and its accuracies. The Sylvania heater is capable of reaching temperatures up to 1200 °F at a mass flow rate of 0.25 kg/s.[40] This low mass flow rate corresponds to an exit Mach number of approximately 0.5, which is below the target Mach number range desired for this study. Furthermore, the 500 °F to 700 °F temperature range has been extensively used for supersonic jet research, thus the heater controller was optimized for temperature stability in this regime. Control of the facility total temperature using the Sylvania heater is simple. The desired temperature is input using an LED display on the heater control box. The temperature stability that the heater can achieve can be quantified by observing the standard deviation of the measured total temperature. The total temperature standard deviation for various total temperatures provided by the heater are shown in Figure 3.3. Assuming a normal distribution, the heater would be accurate to approximately +/- 4 °F across all set total temperatures with 95% confidence.

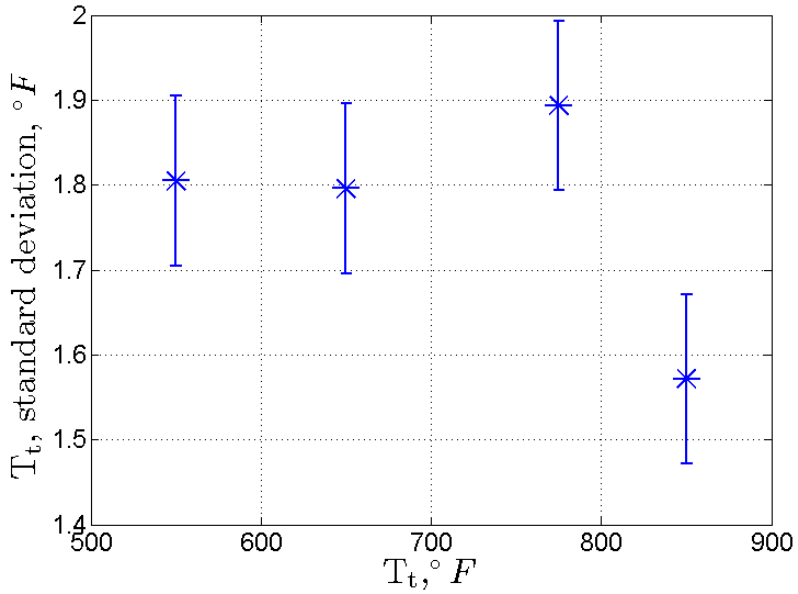

Figure 3.3: Virginia Tech Hot Jet Facility total temperature standard deviation.

For this test program the Mach number was varied from 0.15 to 0.8, and the total temperature was varied from 550 °F to 850 °F. Repeatability and sensor performance were highly dependent on the facility run time previous to acquisition, if the stainless steel facility was not adequately heated. Before data was taken, it was required for the facility to be run until the nozzle temperature achieved a steady state temperature. The heat capacity of the facility, namely the nozzle, was large and was seen to influence the performance of the sensor. This is explained by simply thinking about the heat transfer between the fluid and the facility. If there is heat transfer between the fluid and the facility, the total temperature of the flow would be changing from where it is measured in the plenum and the nozzle exit. Therefore, it is desired for there to be no heat transfer between the facility and the fluid. The day to day repeatability of sensor measurements vastly improved when this was realized and the facility was ran to a steady state nozzle temperature. The nozzle temperature was monitored with the same type of fiberglass thermocouple that the plenum probe uses. The thermocouple was wedged between the external nozzle surface and the nozzle insulation.

The nozzle temperature was monitored in real time and data was taken when the nozzle temperature reached a steady value.

3.3 EXPERIMENTAL RIG

The experimental rig consists of all mechanical assemblies that are directly associated with testing sensor performance. A clam shell strut design was developed to house the sensor and a structure was built to rigidly hold this strut onto the hot jet facility. The strut features internal cooling channels that provide a means to impart a conduction error to the sensor.

3.3.1 Inconel Strut

A strut was chosen to be the method with which to rapidly test sensors under various conduction driver conditions. The strut features a clam shell design to allow easier instrumenting, seen in Figure 3.4. The strut has a span of 3 in. and a chord of 0.95 in. The leading edge contains bores for testing of three 0.032 in. diameter sensors for Kiel head sizes up to 0.08 in. diameter. Two spanwise grooves allow temperature sensor placement for base temperature measurement. The grooves are positioned to be close to the point of contact between the sensor and strut. The inner faces of each strut half was machined smooth so the faces were flush. The airfoil geometry has a maximum thickness to chord ratio of 27%. Each strut half has one 0.03 in. diameter and seven 0.065 in. diameter holes that penetrate the entire span of the strut. These are the channels that the cooling fluid will flow through during operation. The strut was additively manufactured using direct metal laser sintering (DMLS) out of Inconel 718 by Turbocam Energy Solutions. Inconel was chosen primarily due to its thermal conductivity versus other material options and its affordability. It is desired to keep the strut isothermally cooler than the total temperature of the flow. The difference between the strut temperature and the flow total temperature set the conduction driver of the sensor. The thermal conductivity of the strut needs to be high enough such that cooling is effective while not being high enough where the convective heat load on the strut in the hot free stream heats the strut quicker than it is being cooled. To decrease the convective heat loading, a zirconia thermal barrier coating was applied to the strut. The thermal barrier coating was applied via air plasma spraying by Pratt and Whitney.

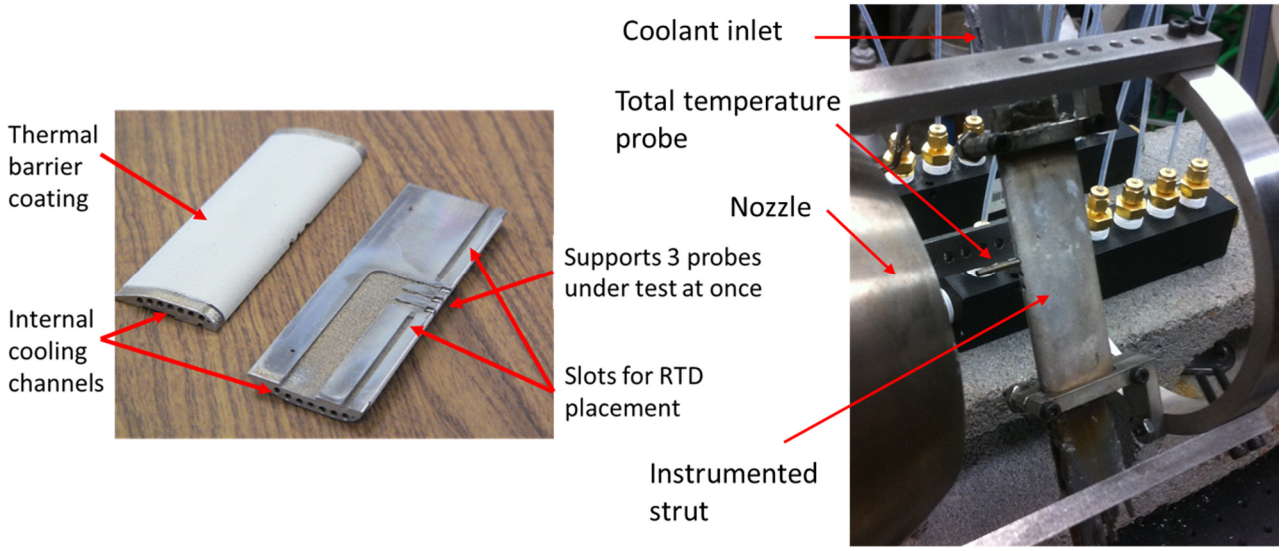

Figure 3.4: (Left) Inconel mounting strut. (Right) Instrumented strut installed in rig.

The instrumented strut features placement for three sensors to test at once, placement for two internal sensors to measure the strut temperature, and eight cooling channels. It should be made clear that the sensor leads exit the strut out of the flow. A simple jig was created to bend sensors at a safe angle before placement into the strut. It was found that the tolerances on the strut manufacturing were not large enough to properly accommodate the sensors to be tested. A gap through the strut was formed when assembly began. This problem was solved by using a high temperature graphite gasket, GRAFOIL, and a high temperature paste, OMEGATHERM 201, to fill in the leading edge gap. This high temperature paste has a high coefficient of thermal conductivity and was subsequently used at all sensor contact points with the strut in hopes of minimizing the effect of thermal contact resistance. Resistance temperature detectors (RTD) were used to measure the base temperature of the strut. The spanwise groove on the inner strut surface was greased with the high temperature paste and the RTD was placed into the groove. Again, the high temperature paste served to reduce thermal contact resistance between the RTD and the strut but also served to hold the RTD in place during strut assembly. Once the instruments were set in place on the strut, the strut was clamped together and attached onto the nozzle mounting structure.

3.3.2 Cooling Operation

The cooling channels were extended with 1/16 in. diameter and 1/32 in. diameter stainless steel tubing. The tubing was inserted roughly 0.25 in. into the strut on both ends. The cooling tube-strut assembly was sealed using JB Weld; other compounds simply could not hold up to the cooling pressure. The free end of the tubes where the cooling fluid was passed through were connected to a 1/16 in. tube to 1/8 in. tube Swagelok union. The cooling manifold was constructed from two aluminum manifolds from McMaster-Carr, part number 5469K165, with pipe fittings to conjoin the two manifolds. The outlets were fitted with 3/8 NPT 1/8 in. Swagelok tube fittings. Flexible nylon tubing with a 1/8 in. diameter was used to connect the cooling manifold to the cooling channel tubes. Both water and air were used to cool the strut. Very large conduction error was imposed when using water as a coolant, but simply using water as the sole coolant would not be

suitable for the testing matrix. Air cooling was needed to hit the low and intermediate conduction errors. Air was pulled from a line to the compressor and the cooling rate was easily adjustable with a needle-nose valve. Water was pulled from the sink and a pump was used to overcome the large pressure loss through the manifold and tubing. The cooling manifold assembly is displayed in Figure 3.5. The free end of the tubes where the cooling fluid was ejected drained into a bucket.

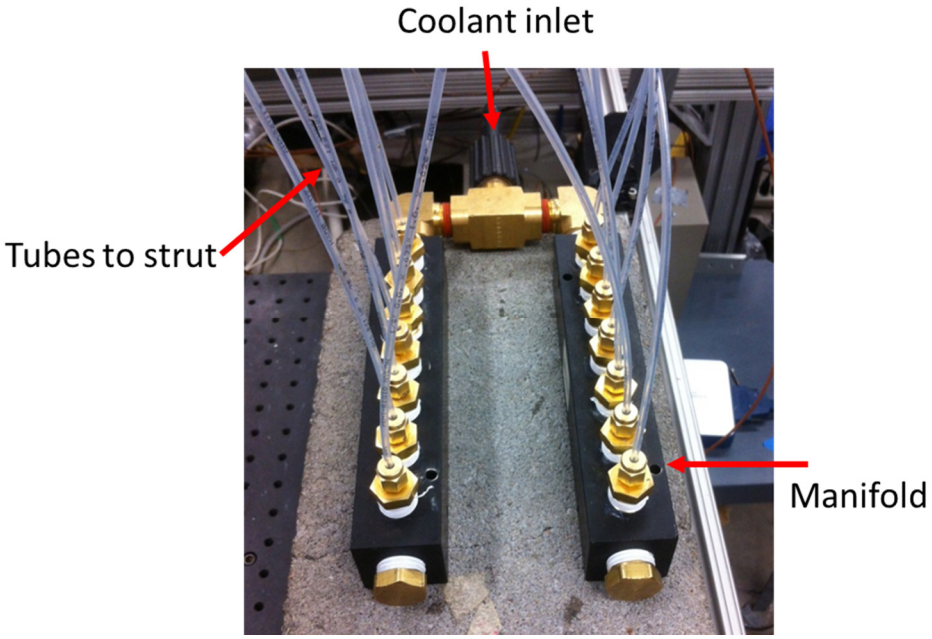

Figure 3.5: Cooling manifold assembly

3.3.3 Nozzle Mount Structure

A simple rig to be used in conjunction with the hot jet facility was designed. The rig features a nozzle mounting structure comprised of a modified 4.5 in. shaft collar, 8 in. stainless steel struts and a circular cross-member that the instrumented strut is screwed onto. A nozzle mounted design was favorable because it ensured repeatable probe positioning that moved with any nozzle deflection due to thermal loads. The nozzle mounted structure can be easily rotated along the nozzle axis and also allows streamwise strut movement to test different distances from the nozzle exit plane. This nozzle mounted structure that the instrumented strut is placed in is shown in Figure 3.6.

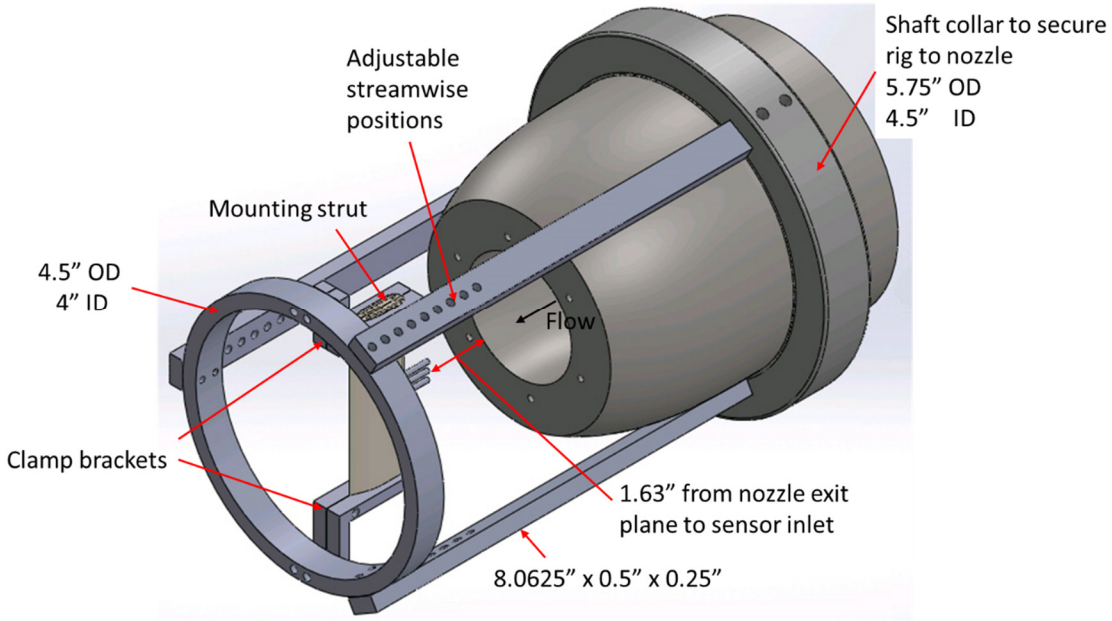

Figure 3.6: Nozzle mount structure assembly

3.4 INSTRUMENTATION

3.4.1 Data Acquisition Hardware

A National Instruments (NI) PXIe-6358 was purchased for 16 channels of high speed, simultaneous voltage measurements. The PXIe-6358 was used in conjunction with an 8 slot National Instruments PXIe-1082 chassis with a PXIe-8133 embedded controller running Windows 7. All data acquisition was acquired through this single PXIe-6358 card. The PXIe-6358 has a 16 bit analog to digital converter, a minimum voltage range of +/- 1 Volt, and is capable of up to 1.5M samples/sec. The bit resolution for this card on the minimum voltage range is 30.5 µV.

All measurements made were acquired as a raw voltage through this card. An external voltage calibration was performed to ensure the voltage accuracy of the card. An Agilent 34420A Nanovoltmeter served as the reference voltage measurement, and a 12 Volt battery served as the voltage source. Two Helipot 8106 ten turn potentiometers were used to create a voltage divider. One potentiometer served as a coarse and the other potentiometer served as a fine adjustment to serve as an effective voltage divider. This voltage divider method was used because there was difficulty synching the NI card with the reference voltage measured by the nanovoltmeter. If the NI card and the nanovoltmeter were perfectly synched, the stability of the voltage signal does not matter. However, since synching the instruments to have the exact acquisition time was not achieved, the voltage signal was instead made to be steady. The NI card voltage was then corrected linearly versus the nanovoltmeter reading, i.e. Voltage_Agilent = m*Voltage_NI + b. This calibration was applied during post-processing.

It was earlier mentioned that the temperature of the strut was measured using resistance temperature detectors (RTD). The resistance across an RTD changes as a function of temperature.

RTD's are not self-powered devices and thus require a current to be supplied across the excitation leads. RTD transmitters from Acromag were used to supply this constant current. Acromag ST131-0600 transmitters were powered with +/- 15 Volts DC and were cited to produce a nominal constant current of 0.5 mA. The accuracy of the constant current source is the largest source of uncertainty in an RTD measurement. Due to this fact, the constant current value had to be measured under various loads. Precision foil resistors from Vishay were used to simulate the resistance of the RTD. Resistors of 100, 120, 200, 250, and 350 Ω were used to determine how the output current from the Acromag RTD transmitter behaved over various loads. The voltage drop across each resistor was measured and recorded using the Agilent 34420A Nanovoltmeter. With the voltage across the resistor and the resistance value of the resistor being known, Ohm's law, V = IR, can be simply used to compute the current through the resistor. This was performed for each transmitter. The output current value was defined as a function of measured voltage. Thus, when the voltage across the RTD is measured, the curve fit value for current versus voltage is used to determine what the actual value of the current is.

Total pressure measurements were made in the jet plenum with a Scanivalve ZOC17/8Px-APC pressure transducer. This pressure transducer was referenced to ambient atmospheric conditions and had a maximum range of 50 psig. The transducer required 15 Volt DC power and output a voltage linearly proportional to the pressure. The transducer was calibrated with a standard deadweight pressure gauge tester. The atmospheric pressure was measured with a Conex Electro Systems JDB1 Digital Barometer that has a ±0.05 in. Hg accuracy.

3.4.2 Temperature Devices

The jet plenum total temperature probe uses a 30 AWG wire, fiberglass insulated, exposed junction Type K thermocouple. This thermocouple was manufactured by Omega Engineering, part number 5TC-GG-K-30-36. The temperature reading from this plenum probe was taken to be the total temperature of the flow.

It was common engineering knowledge that an output thermocouple signal is produced when a temperature difference exists in the thermocouple loop between the hot junction and the cold junction. All thermocouples were referenced to 0 °C. There were two important reasons for referencing all thermocouple signals to 0 °C: the National Institute of Standards and Technology (NIST) tables for thermocouple calibrations, which also reference thermocouple signals to 0 °C, could then be easily implemented and the thermocouple signal magnitude would be larger than having a cold junction at a higher temperature. Previous work has been done where the sensor under test had served as the cold junction for the plenum total temperature sensor and the signal difference was converted to a direct temperature difference between the two sensors. This method leads to thermocouple signals on the μV level as opposed to thermocouple signals on the mV level when the junction is kept at 0 °C. GE/Kaye K140-4 Ice Point References were purchased from Amphenol Thermometrics, Inc. These ice point references kept a cold well to 0 °C with guaranteed +/- 0.05 °C accuracy, though +/- 0.02 °C accuracy was typical. The cold junctions for all thermocouples used in this study were inserted into the cold well. The cold junctions for all thermocouples used were simply twisted-shielded thermocouple extension wire that was twisted into a bare-wire junction on one end. The other free end of the extension wire was appropriately

welded to the wire extending from the hot junction. The two positive wire legs carrying the differential thermocouple signal were then read by the PXIe-6358. A schematic of this thermocouple circuit is shown in Figure 3.7.

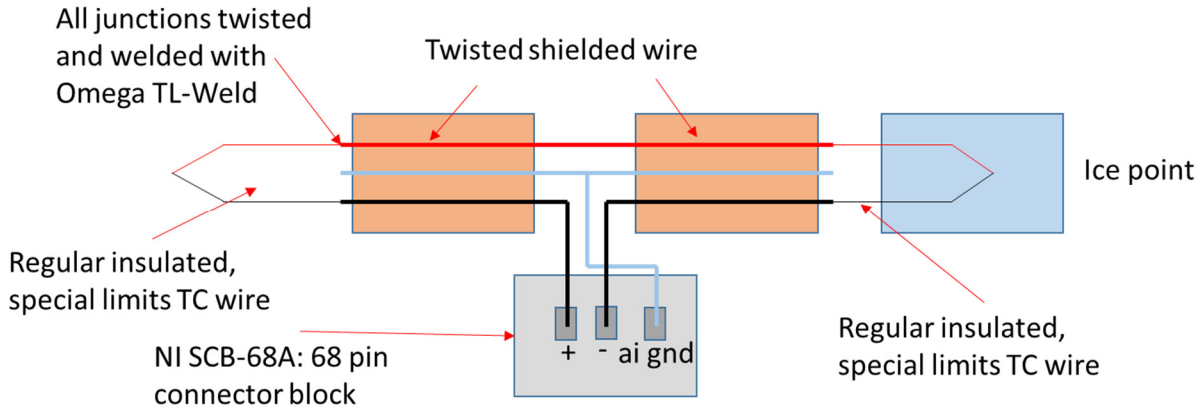

Figure 3.7: Thermocouple wiring diagram

The base temperature was measured using 4 wire RTD's from Sensing Devices, Inc. These RTD's are Platinum 100Ω thin film sensors with a nominal temperature coefficient of 0.00385 Ω/Ω/°C. The nominal resistance is 100 Ω +/-0.12% at 0 °C, known as Class B accuracy specified in the International IEC 60751 Standard. The RTD element is a thin film model TF100/2108. The manufacturer provided the calibration coefficients for each RTD that are used to determine its Callendar-van Dusen (CDV) equation. The Callendar-van Dusen equation describes the relationship between resistance and temperature for platinum RTD's. Specifically how the base temperature is extracted from the RTD will be described in the post-processing segment of this report.

3.5 Data Collection

This section contains all information on how the data was acquired and processed. The hardware used for data acquisition, as well as acquisition procedure is discussed.

3.5.1 Data Acquisition

All data acquisition was performed using Labview software. A Virtual Instrument (VI) was written for acquisition of all instruments measured with the NI PXIe-6358 card. The user interface features real time gauges for an assortment of temperatures and conduction driver. This user interface is shown in Appendix C: Acquisition User Interface. These gauges allow the user to observe when a certain total temperature or conduction driver has been achieved. All variables except the total pressure are saved in the form of a raw voltage. The raw voltage associated with the total pressure is calibrated and converted to pressure for real time monitoring. The total pressure of the flow is subsequently written to the output file. The variables that are acquired and saved are the flow total temperature, the flow total pressure, the measured sensor temperature, the strut base temperatures, and the nozzle temperature. Data was acquired with a sample frequency of 10 kHz for 30 seconds.

3.5.2 Data Post-Processing

All post-processing of the raw data was performed in Matlab. The Matlab post-processing script accepted an Excel input file containing raw voltages from temperature measurements and the total pressure value. This script converted the temperatures from raw voltage units to standard engineering units, such as degrees Fahrenheit or Celsius, using multiple subroutines. Multiple steps were required to convert the raw data to its final form. First, the voltage calibration was applied to the raw voltage to yield the true, calibrated voltage. Next a digital low-pass filter with a cutoff frequency of 4 kHz was applied to discard of high frequency noise caused by the heater operation. In addition to digital filtering, large outliers were replaced with the bin mean. The signal was split into 1000 point bins, and any points that were outside of +/- 3 standard deviations from the bin mean were replaced with the bin mean. This eliminated any spurious signals that were not removed during the digital filtering process. Once the raw voltage was calibrated and filtered, next it was passed through a separate subroutine to convert the voltage to a temperature depending on if the voltage read was from a thermocouple or an RTD.

Thermocouple voltage to temperature conversions were performed using National Institute for Standards and Technology (NIST) curve fits from NIST tables for type K and B thermocouples. The curves relate measured thermocouple voltage to temperature using a 9^{th} order polynomial. Over a specific temperature range, the maximum temperature error between a NIST certified thermocouple and the NIST curve fits is on the order of +/- 0.1 °F. The NIST curve fit used to obtain measured temperature for type K thermocouples is valid from 0 °C to 500 °C (32 °F to 932 °F). The NIST curve fit used to obtain measured temperature for type B thermocouples is valid from 250 °C to 700 °C (482 °F to 1292 °F).

RTD voltage to temperature conversions were performed using the Callendar-van Dusen (CVD) equation previously discussed. Recall that the voltage drop across the RTD is directly measured and also that the Acromag transmitter is used to provide constant current excitation. The current value that the transmitter is actually providing is a function of the resistive load that it is under, which is also a function of the voltage drop across the RTD using Ohm's Law. The constant current value for the transmitter was calibrated using high precision foil resistors manufactured by Vishay. A polynomial fit was used to obtain the value of current as a function of measured voltage drop. Therefore, the voltage drop measured across the resistor is used to obtain the transmitter output current value. Since both the voltage drop across the RTD and the excitation current is known, the resistance of the RTD can be simply calculated using Ohm's Law R = V/I. It is extremely important to minimize the uncertainty in the excitation current value. The excitation current value is approximately 0.5 mA. An error of just 0.02 mA will cause a significant difference in the calculated RTD resistance value, which in turn propagates through the CVD equation and ultimately yields an inaccurate base temperature measurement. Once the measured voltage drop was converted to RTD resistance, the CVD equation was used. The fundamental CVD equation is shown in Equation (3.1). In this equation, R is the measured RTD resistance, T is the RTD temperature in degrees Celsius, R_0 is the resistance at 0 °C, and A and B are directly related to the RTD calibration.

$$R = R_0(1 + A \cdot T + B \cdot T^2) \tag{3.1}$$

The variables R_0, A, and B in Equation (3.1) are different for each RTD. The resistance at 0 °C is nominally 100 Ω for the platinum thin film RTD's used in this study. Other coefficients that compose an RTD's calibration are its α and δ coefficients. The RTD temperature coefficient is α and a separate high temperature calibration coefficient is δ. These RTD calibration coefficients were provided by the manufacturer and are needed to determine the values of A and B in Equation (3.1). The variables A and B are mathematically determined in Equations (3.2) and (3.3).

$$A = \alpha(1 + \frac{\delta}{100}) \tag{3.2}$$

$$B = -\alpha \cdot \delta \cdot 10^{-4} \tag{3.3}$$

Equation (3.1) gives RTD resistance as a function of temperature. For this study, the resistance of the RTD is measured and the temperature is unknown; therefore it is desired to know the RTD temperature as a function of resistance. This is done by simply solving Equation (3.1) for the temperature variable T. This is expressed below in Equation (3.4).

$$T = \frac{-A\sqrt{R_0} - \sqrt{R_0(A^2 - 4B) + 4BR}}{2B\sqrt{R_0}} \tag{3.4}$$

Combining Equations (3.2) and (3.3) to compute the values of A and B and Equation (3.1) yields the temperature measured by the RTD. This RTD measured temperature is taken to be the base temperature of the strut.

Recall that data acquisition occurs at a sampling frequency of 10 kHz over 30 seconds. This provides a sufficiently long acquisition time to average and reduce the data. Data must be acquired over a long time to maximize the benefit of averaging. Data was always acquired at a perceived steady state condition. However, it is still necessary to average this data due to small fluctuations in the flow characteristics. The primary source of fluctuation came from the jet heater which stemmed from the jet PID controller that regulates the flow valve. This unsteady feature of the jet controller manifests itself as a flow total temperature that fluctuates by a few degrees. Averaging the time series data reduces the effect of this fluctuation. Once all raw voltages have been calibrated, filtered, and converted to their respective temperatures, the time series data is saved to a Matlab structure. A separate Matlab script was developed to take the time series data and determine sensor performance and specific flow characteristics, such as Mach and Reynolds number. The sensor recovery factor was calculated from averaging the appropriate temperatures as shown in Equation (3.5). The sensor Mach corrected recovery factor was performed in accordance with Equation (1.10). This Mach correction is used to eliminate velocity error such that conduction error is the only substantial error in the sensor measurement; radiation in this temperature regime was determined to be negligible by basic simulations, compared to convection and conduction. The dimensionless conduction driver was calculated from averaging the appropriate temperatures as shown in Equation (3.6). To summarize the averaging procedure, all variables acquired take the value of the mean of its respective time series.

$$R = \frac{mean(T_j)}{mean(T_t)} \tag{3.5}$$

$$\Theta = \frac{mean(T_t) - mean(T_b)}{mean(T_t)} \tag{3.6}$$

The following assumptions were made during data post-processing: the flow is behaving as an ideal gas, the flow is isentropic, and Sutherland's law is valid for viscosity calculation. The flow characteristics were calculated with gas properties, such as viscosity, evaluated at the total temperature of the flow. The Mach number of the flow at the nozzle exit was calculated using the isentropic relation for total and static pressure. This important, fundamental relationship is expressed in Equation (3.7). The ratio of specific heats for air is represented as γ, the total pressure of the flow is represented by p_0, the static pressure of the flow is represented by p, and the Mach number of the flow is represented as M.

$$\frac{p_s}{p_t} = (1 + \frac{\gamma - 1}{2} M^2)^{\frac{\gamma - 1}{\gamma}} \tag{3.7}$$

The Reynolds number of the flow was calculated in accordance with its definition in Equation (3.8). This Reynolds number uses the freestream flow that the sensor is subjected to. The freestream density, ρ, is calculated in accordance with the ideal gas law at static pressure in Pascals and temperature in Kelvin at the nozzle exit. The gas constant, R, uses the constant value of 287 J/kg/K. The density calculation performed is shown in Equation (3.9). The freestream velocity in m/s, U, is calculated from the Mach number and speed of sound, a, at the nozzle exit. The freestream velocity calculation performed is shown in Equation (3.10). The dynamic viscosity in kg/m/s, μ, is calculated using Sutherland's law with the temperature evaluated at the total temperature in Kelvin of the flow. Evaluating the viscosity at this temperature resulted in a better data collapse. Sutherland's law is expressed in Equation (3.11).

$$\mathrm{Re} = \frac{\rho U L}{\mu} \tag{3.8}$$

$$\rho = \frac{P}{RT} \tag{3.9}$$

$$U = M \cdot a = M \cdot \sqrt{\gamma R T} \tag{3.10}$$

$$\mu = \frac{1.4578 \cdot 10^{-6} \cdot T_t^{1.5}}{T_t + 110.4} \tag{3.11}$$

The only variable left undefined in the Reynolds number calculation is the length scale, L. The length scale that is used is the inlet diameter (ID) of the sensor under test. This ID Reynolds number uses the external flow around the sensor scaled on the inlet diameter of the sensor. It can be argued

that this may not be the proper Reynolds number to use for data analysis. However, it cannot be refuted that it is the most convenient Reynolds number definition to use. Experimental turbine rigs can easily obtain the Reynolds number of the external scale, in the previously described fashion, and simply scale it on the sensor ID. It is nearly impossible to measure the true Reynolds number that the miniature sensor experiences internally. This would require measuring the velocity past the sensor, which is not a trivial task.

3.6 UNCERTAINTIES

The total uncertainty for a system made up of multiple components is subject to the uncertainty of each individual component. The uncertainties of the individual components are generally known, or are easy to estimate. It is extremely important to quantify how the uncertainties of individual parameters combine into the overall uncertainty of the experimental result. The process for estimating system uncertainty will be briefly discussed here. Consider a system y that is a function of n independent variables, shown in Equation (3.12).

$$y = f(x_1, x_2, \ldots, x_n) \tag{3.12}$$

Taylor series expansion can be used with good approximation to estimate the corresponding change in y for small changes in x_n.[23] The change in y versus the change in x_n is estimated in Equation (3.13).

$$\Delta y = \frac{\partial f}{dx_1}\Delta x_1 + \frac{\partial f}{dx_2}\Delta x_2 + \ldots + \frac{\partial f}{dx_n}\Delta x_n \tag{3.13}$$

The partial derivatives represent the sensitivity of y to changes in each independent variable. If the small changes in each independent variable are considered to be the uncertainty of each independent variable, the root-sum-square formula can be used to determine the uncertainty of y. This formulation is known as the propagation of errors and is shown in Equation (3.14).

$$\delta y = \sqrt{\left(\frac{\partial f}{dx_1}\delta x_1\right)^2 + \left(\frac{\partial f}{dx_2}\delta x_2\right)^2 + \ldots + \left(\frac{\partial f}{dx_n}\delta x_n\right)^2} \tag{3.14}$$

This formulation for system uncertainty will be applied to determine the uncertainty in recovery data. Recall the definition of overall recovery factor in Equation (1.1). Using Equation (3.14), the overall uncertainty in recovery factor is expressed in Equation (3.15). The partial derivatives are evaluated accordingly and substituted to yield the result in Equation (3.16).

$$\delta R = \sqrt{\left(\frac{\partial R}{dT_j}\delta T_j\right)^2 + \left(\frac{\partial R}{dT_t}\delta T_t\right)^2} \tag{3.15}$$

$$\delta R = \sqrt{\left(\frac{1}{T_t}\delta T_j\right)^2 + \left(-\frac{T_j}{T_t^{\,2}}\delta T_t\right)^2} \tag{3.16}$$

The overall recovery uncertainty is clearly a function of the uncertainties of the total temperature probe under test and the plenum probe. The plenum probe uses a type K thermocouple with special limits of error wire; wire of this quality is taken to have an uncertainty of 1.98 °F or 0.4% above 32 °F. The greater of these two values are used for the uncertainty in the total temperature measurement. The uncertainty associated with the sensor 2 was taken to be 0.87 °F; this temperature uncertainty was provided from the manufacturer. Evaluating experimental results using these estimated uncertainty values yields an uncertainty on the order of 0.0025 in the overall recovery factor for sensor 2. It is important to note that this value is simply the minimum uncertainty for a single point measurement. The uncertainty in overall recovery for a nominal total temperature of 850 °F and Θ = 0.6 is shown in Figure 3.8.

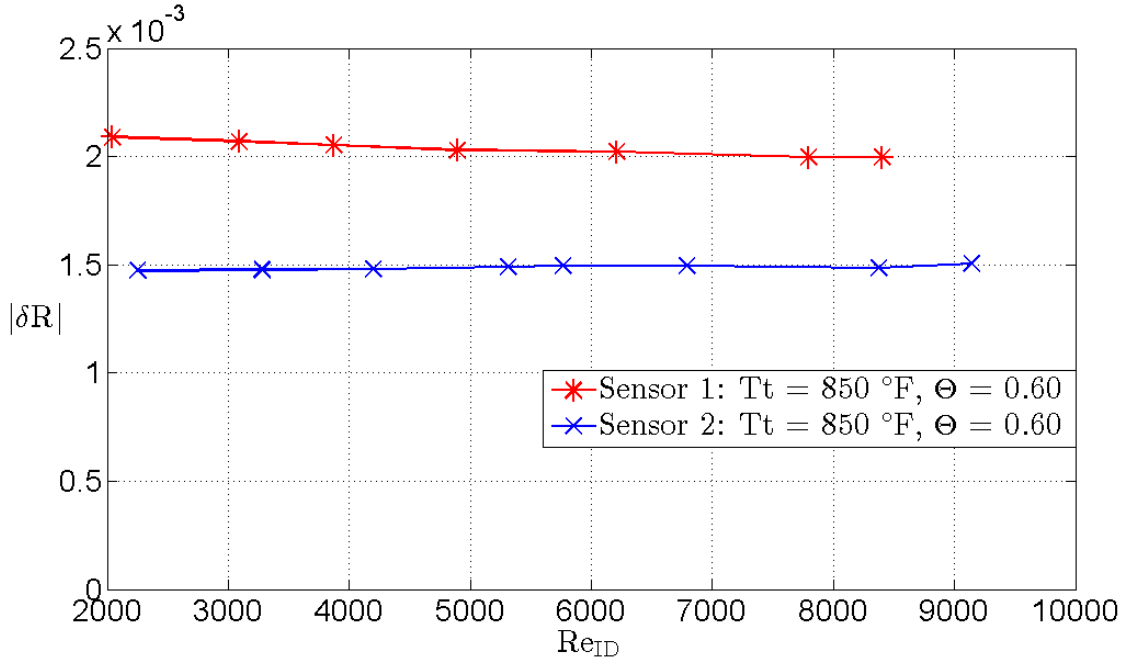

Figure 3.8: Uncertainty in overall recovery factor R.

The same procedure is performed to calculate the overall uncertainty for the Mach corrected recovery factor. Recall the definition of the Mach corrected recovery factor in Equation (1.10). The Mach corrected recovery factor is strictly a function of Mach number M, aerodynamic recovery factor α, and overall recovery factor R. The partial derivatives of Equation (1.10) with respect to these three independent variables are expressed in Equation (3.18) through Equation (3.20).

$$\delta\overline{R} = \sqrt{\left(\frac{\partial\overline{R}}{dR}\delta R\right)^2 + \left(\frac{\partial\overline{R}}{d\alpha}\delta\alpha\right)^2 + \left(\frac{\partial\overline{R}}{dM}\delta M\right)^2} \tag{3.17}$$

$$\frac{\partial\overline{R}}{dR} = 1 \tag{3.18}$$

$$\frac{\partial \bar{R}}{d\alpha} = -\frac{[(\gamma-1)/2]M^2}{1+[(\gamma-1)/2]M^2} \tag{3.19}$$

$$\frac{\partial \bar{R}}{dM} = -\frac{4(\alpha-1)(\gamma-1)M}{\left((\gamma-1)M^2+2\right)^2} \tag{3.20}$$

The uncertainty in overall recovery factor δR is calculated just as in Equation (3.16). Moffat reports the uncertainty in the aerodynamic recovery factor for a thermocouple aligned with the flow to be ±0.09.[2] The uncertainty in Mach number comes to the uncertainty in measured static and total pressure. Mach number is related to these pressures by Equation (3.7). Thus the uncertainty in Mach number is related to the uncertainty in static and total pressure by Equation (3.21). Differentiating Equation (3.7) with respect to the static pressure and total pressure yields Equations (3.22) and (3.23), respectively.

$$\delta M = \sqrt{\left(\frac{\partial M}{\partial p_s}\delta p_s\right)^2 + \left(\frac{\partial M}{\partial p_t}\delta p_t\right)^2} \tag{3.21}$$

$$\frac{\partial M}{\partial p_s} = \frac{\gamma\left(\frac{p_s}{p_t}\right)^{\frac{1}{\gamma-1}}}{\sqrt{2}(\gamma-1)^2\, p_t \sqrt{\frac{\left(\frac{p_s}{p_t}\right)^{\frac{\gamma}{\gamma-1}}-1}{\gamma-1}}} \tag{3.22}$$

$$\frac{\partial M}{\partial p_t} = -\frac{\gamma p_s\left(\frac{p_s}{p_t}\right)^{\frac{1}{\gamma-1}}}{\sqrt{2}(\gamma-1)^2\, p_t^{\,2} \sqrt{\frac{\left(\frac{p_s}{p_t}\right)^{\frac{\gamma}{\gamma-1}}-1}{\gamma-1}}} \tag{3.23}$$

The uncertainty in static and total pressure measurement was taken to be the uncertainty of the instruments measuring them. The uncertainty for the total pressure measurement was taken to be ±0.08% of the full scale transducer value of 50 psig, the quoted uncertainty value for the Scanivalve Zoc17 pressure transducer used. This yields an uncertainty of approximately 275 Pa for the total pressure measurement. The uncertainty in the static pressure was taken from the quoted

±0.05 in. Hg of the pressure reading for the digital barometer. This yields an uncertainty of approximately 340 Pa for the static pressure measurement. Combining Equations (3.17) through (3.21) gives an estimation of the overall uncertainty for the Mach corrected recovery results. The uncertainty in the aerodynamic recovery factor α contributes the largest amount of uncertainty to the Mach corrected recovery results. It is expected for the uncertainty in the Mach corrected recovery to be greater than the uncertainty for the uncorrected recovery, simply due to the fact that two more sources of uncertainty are introduced in the calculation. This behavior is shown in Figure 3.9 and is explained upon inspection of Equation (3.19). This behavior scales with the square of Mach number because d $\overline{R}$ /dα scales with the square of Mach number.

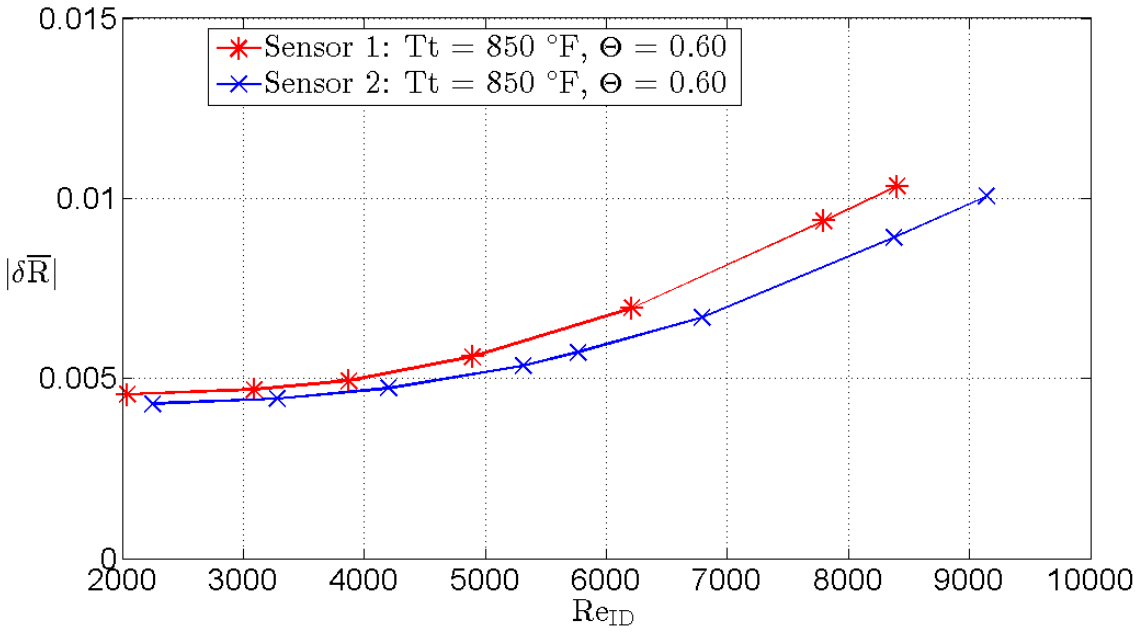

Figure 3.9: Uncertainty in Mach corrected recovery factor $\overline{R}$

A more expansive discussion of overall experimental uncertainty is found in Appendix A: Expanded Experimental Uncertainty and Model Sensitivity.

4 EXPERIMENTAL RESULTS

Experimental results for both the sensors are presented in this section. The results for each sensor are presented separately due to the differences in respective sensor geometry and material. Observations that were made in section 2.3 expressing sensor performance as function of Reynolds number and conduction driver are expected to be valid for the experimental results.

It is important to make note that the cooling rate was kept constant when acquiring a single set of data; the conduction driver was not necessarily constant with probe Reynolds number test conditions. Depending on whether air or water was used as the cooling fluid, the steadiness of the conduction driver was affected. Water was the most effective coolant and the variation of the conduction driver with Reynolds number was minimally affected. Water was used as the coolant fluid to impose high conduction drivers to the sensor. Air was used as the coolant fluid to impose very low to moderate conduction errors to the sensor. The heat capacity of water is about 4.2 kJ/kg/K while the heat capacity of air is 1.005 kJ/kg/K at standard temperature and pressure; water has over quadruple the heat capacity of air thus making it an extremely effective coolant.

Since the cooling rate was specified via a valve setting, the conduction driver varied with probe Reynolds number test conditions. This phenomena is shown in Figure 4.1. The heat transfer balance between conduction and convection changes as convection is increased, and the cooling rate is kept constant. Increased convective heat transfer over the strut and sensor generally resulted in a lower conduction driver. The large heat capacity of water effectively kept the conduction driver constant with Reynolds test number, but the variance of driver versus Reynolds is clearly seen when air is used as the coolant.

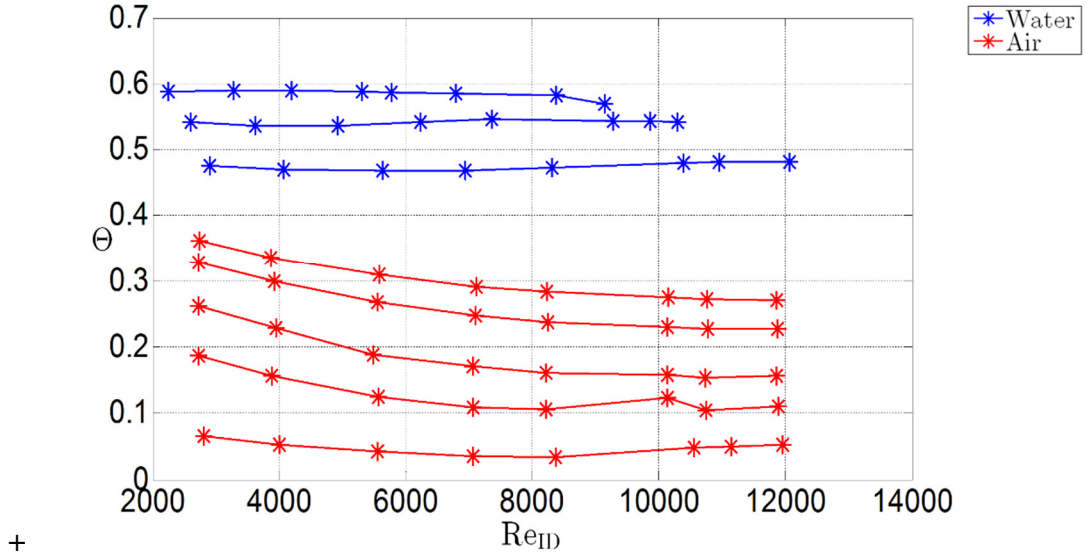

Figure 4.1: Effect of heat convection on sensor 2 conduction driver for water and air coolants.

The figures following in this section all have the conduction driver averaged for a data set. The deviation between the average and actual driver value is negligible when water is used as the

coolant. When air is used as the coolant, the deviation between the average and actual driver value is significantly larger. These deviations from average driver used is shown in Figure 4.2. It is important for the reader to realize this during data presentation.

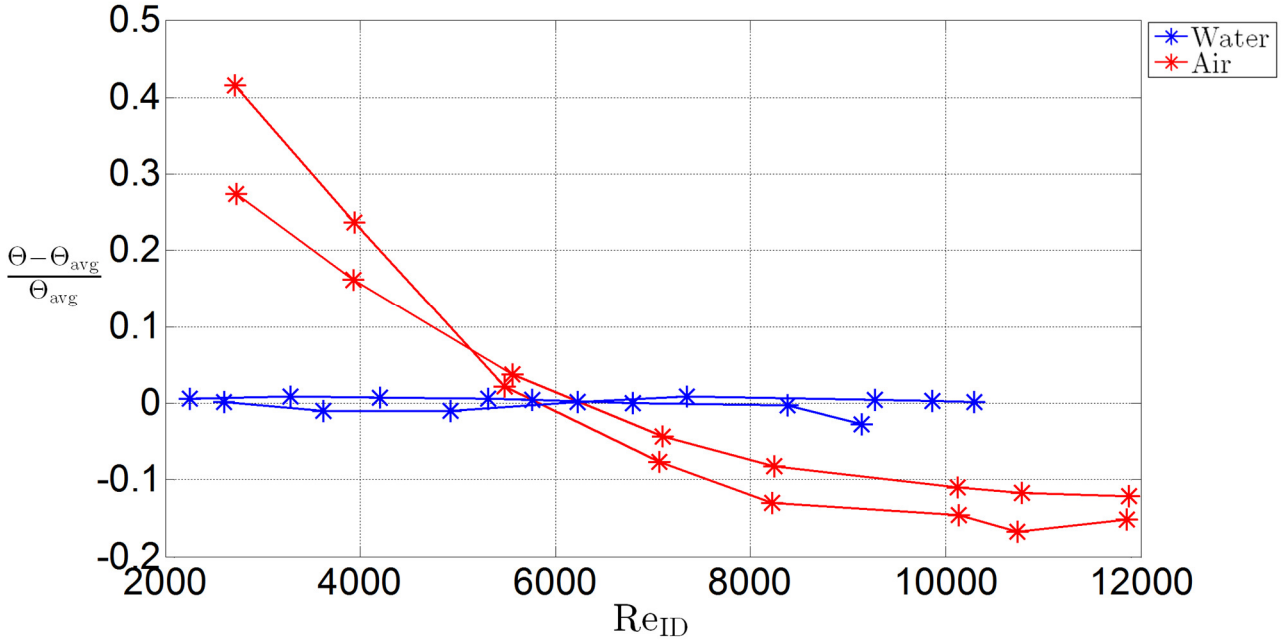

Figure 4.2: Conduction driver deviation from mean driver for water and air coolant for sensor 2.

Conduction drivers for sensor 2 less than 0.4 were all obtained using air as the coolant. For both sensors, conduction drivers greater than 0.4 were all obtained using water as the coolant. Air cooling was not performed for sensor 1.

The effect of Reynolds number on sensor performance was determined to be a significant factor, referencing previous insight gained by using the thermal resistance model in section 2.3.2. The effect will be presented for both types of sensors. Sensor performance is Mach corrected in order to isolate the effect that conduction has on sensor performance. Sensor measurement error due to radiation is not accounted for.

4.1 SENSOR 1

The data set for sensor 1 consisted of 4 independent runs, repeated two or three times for a total of 13 runs, over a range of total temperatures between 300 °F and 850 °F with Θ ranging between about 0.05 and 0.6. The range of the Reynolds number varied between 2000 and 15,000.

4.1.1 Impact of Reynolds Number and Conduction driver

The impact of the Reynolds number on sensor 1 performance is shown in Figure 4.3. The Mach corrected recovery is presented against Reynolds number for a driver of Θ = .55. As expected, sensor performance relies on the Reynolds number. The effect that the Reynolds number has on sensor 1 performance is not as strong as found for sensor 2 results to be shown below. This is primarily due to the dramatic difference in thermal conductivity between the sensors, with

secondary effects stemming from differences in sensor geometry and fabrication. About 3% of the flow total temperature is further recovered between the lowest Reynolds condition and the highest Reynolds condition.

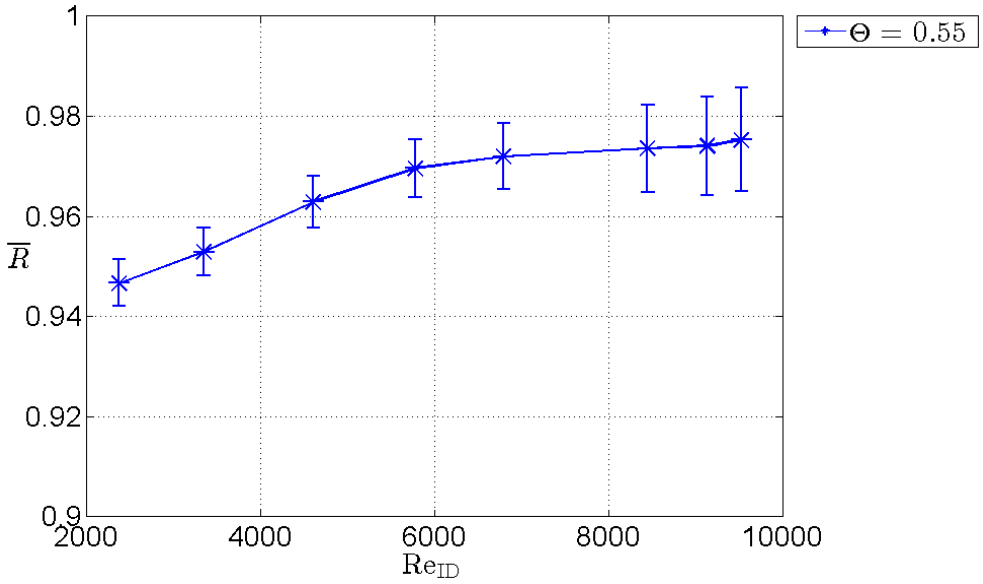

Figure 4.3: Dependence of sensor 1 performance on Reynolds number for Θ = 0.55.

Sensor 1 was tested over a limited range of conduction conditions and total temperatures between 300 °F and 850 °F. The conduction conditions were achieved using only water as the coolant. A portion of the Type K data set that includes the total range of conduction drivers tested is shown in Figure 4.4. The sensor performance is seen to increase as the conduction driver decreases.

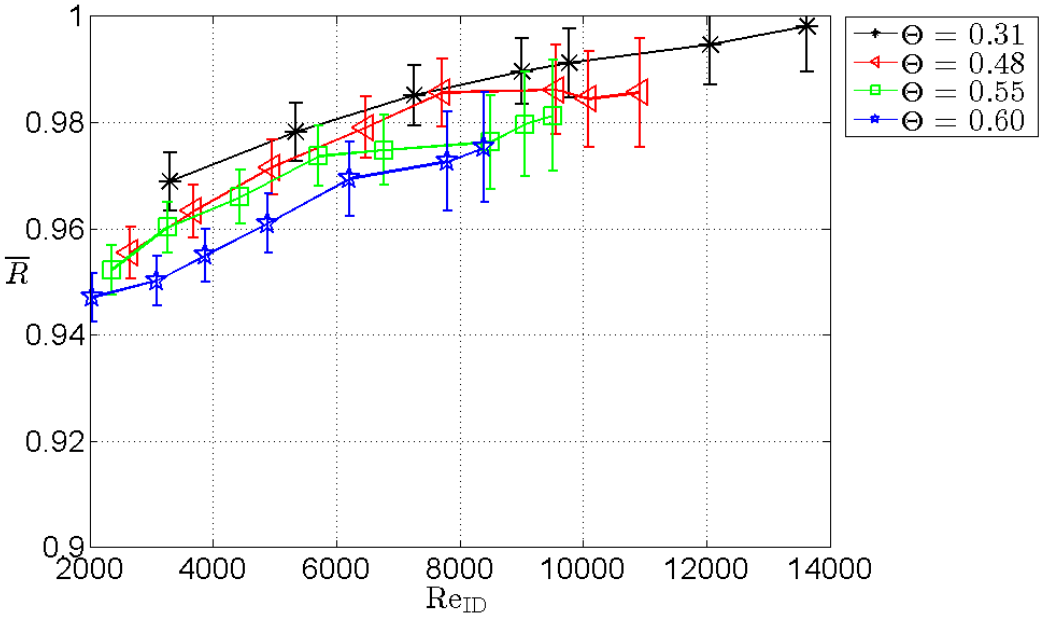

Figure 4.4: Dependence of sensor 1 performance on conduction driver as a function of Reynolds number, T_t ranging from 300 °F to 850 °F

4.1.2 Comparison of Results to Thermal Resistance Model Predictions and Simulations

Results comparing experimental data with thermal resistance model predictions will be presented. A few select simulations were performed to predict sensor 1 performance using ANSYS Fluent. A multi-physics CFD model was developed in conjunction with this study to provide high fidelity sensor predictions.[43]

The comparison of sensor 1 experimental data, its respective low-order and CFD predictions are shown in Figure 4.5. The low-order model significantly under predicts the sensor performance across the entire Reynolds number range. This is a shortcoming of the low-order model that was briefly discussed in section 2.3.5. Four CFD simulations were performed with $\Theta = 0.5$ at total temperatures of 550 °F and 850 °F at the upper and lower bounds for Reynolds numbers. There is excellent agreement between the experimental data and the simulation results for $\Theta = 0.5$ with total temperature of 550 °F at the high Reynolds test condition. The experimental facility was not able to achieve Reynolds numbers below 2000; simulations were performed with Reynolds numbers of about 1000 to 1500. It can be expected that further sensor performance roll-off would be achieved if the minimum achievable Reynolds number for the facility was able to match those of the simulation results.

The ratios between experimental data and thermal resistance model predictions are shown in Figure 4.6. The indicated trend shows that the thermal resistance model under predicts sensor performance at low Reynolds numbers. Again, this is caused by the small convective heat transfer at low Reynolds number. As the convective heat transfer approaches zero, the thermal resistance model approaches the steady-state conduction solution where the thermocouple temperature is equal to the base temperature.

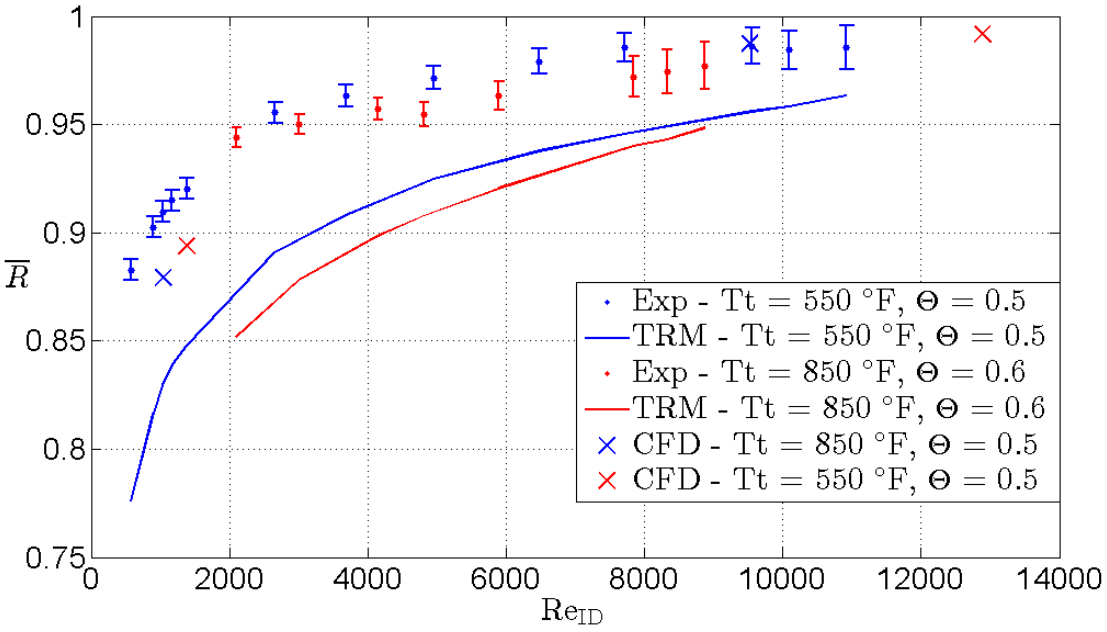

Figure 4.5: Comparison of experimental results, TRM predictions, and CFD simulations for sensor 1 performance

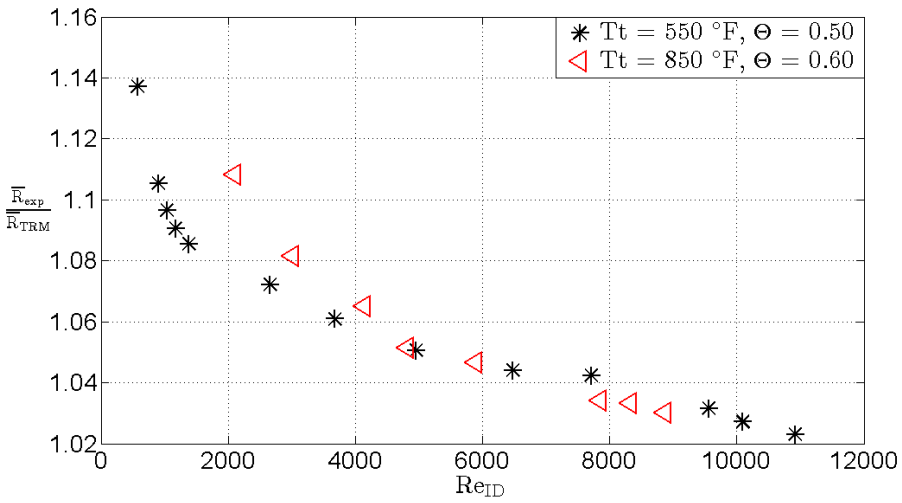

Figure 4.6: Ratio between sensor 1 experimental data and thermal resistance model predictions.

4.2 SENSOR 2

The effect of conduction driver on sensor performance was determined to be a significant factor, referencing previous insight gained by using the thermal resistance model in section 2.3.3. Sensor performance is still Mach corrected in order to isolate the effect that conduction has on sensor performance. The data set for sensor 2 consisted of 16 independent runs, repeated twice for a total of 32 runs, over a range of total temperatures between 550 °F and 850 °F with Θ ranging between about 0.05 and 0.6. The range of the Reynolds number varied between 2000 and 12,000.

4.2.1 Impact of Reynolds Number and Conduction Driver

The impact of the Reynolds number on the sensor 2 performance is shown in Figure 4.7. The Mach corrected recovery is presented against Reynolds number for a driver of Θ = .47 with a nominal total temperature of 550 °F. As expected, sensor performance heavily depends on the Reynolds number. More than 7% of the total temperature is recovered at high Reynolds conditions versus low Reynolds conditions. This is in agreement with thermal resistance model predictions.

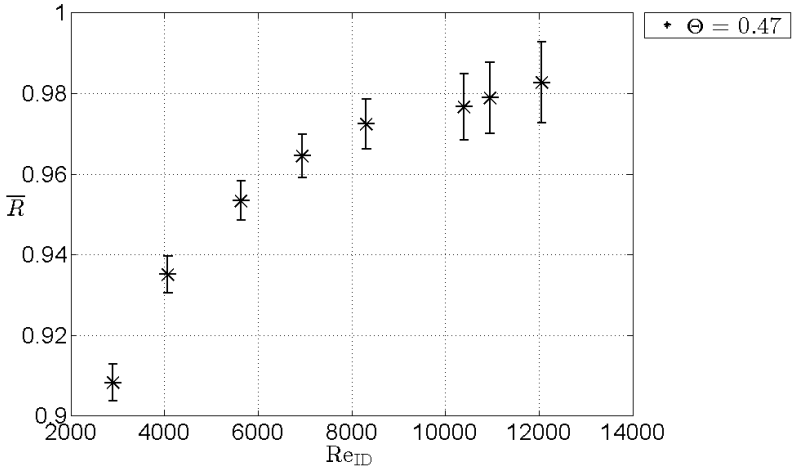

Figure 4.7: Dependence of sensor 2 performance on Reynolds number, Θ=0.47, T_t=550 °F

Sensor 2 was tested over a range of conduction conditions and total temperatures between 550 °F and 850 °F. The conduction conditions were achieved using air and water as coolants, as well as no cooling. A portion of the complete data set that includes the total range of conduction drivers tested is shown in Figure 4.8. The sensor performance clearly increases as the conduction error decreases. The effect of not cooling the strut ($\Theta = 0.05$) yielded the best sensor performance. The conduction driver was nonzero even though the cooling was off due to the internal cooling channels providing a path to absorb and diffuse part of the heat load. Introducing a very low rate of airflow to cool the strut clearly affected the sensor performance for Reynolds number below 10,000. The effect of conduction on sensor performance is largest at lower Reynolds number due to decreased heat transfer by convection. This was a trend observed in the low-order model analysis.

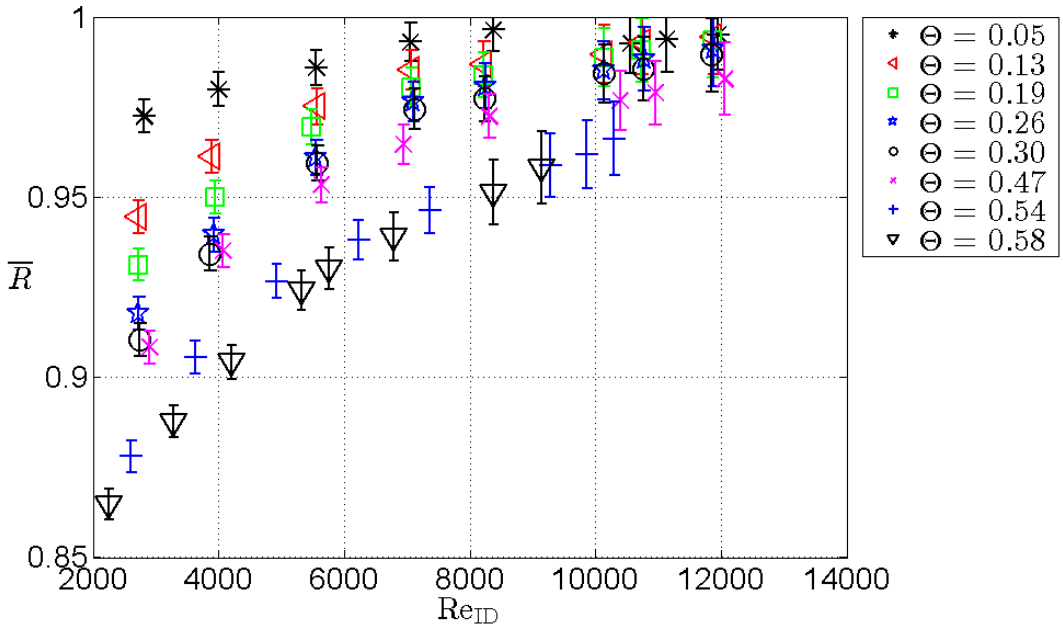

Figure 4.8: Dependence of sensor 2 performance on conduction driver as a function of Reynolds number, T_t ranging from 550 °F to 850 °F

4.2.2 Comparison of Results to Thermal Resistance Model Predictions

The comparison of experimental data for sensor 2 and its respective thermal resistance model predictions are shown in Figure 4.9. The thermal resistance model accurately predicts sensor performance when the conduction driver is low. It quickly loses accuracy when the conduction driver increases. The ratio between experimental data and thermal resistance model predictions is displayed in Figure 4.10. The characteristic is significantly different than the observed characteristic for sensor 1 in Figure 4.6. This difference is explained by the significantly different probe geometry; the thermal resistance model was modified to accommodate the geometry of sensor 2.

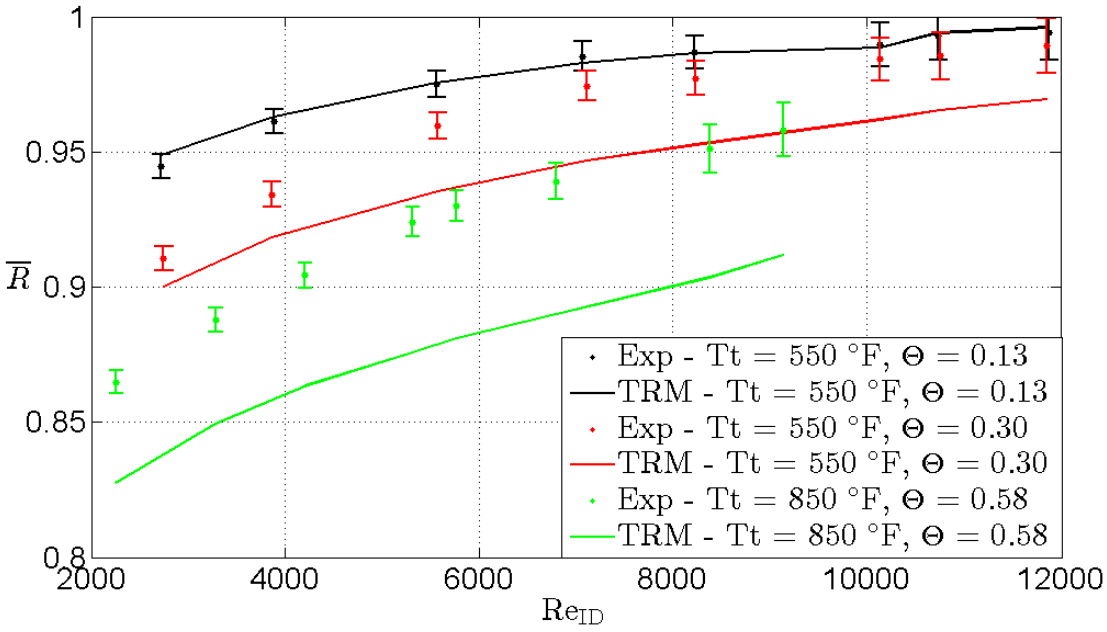

Figure 4.9: Comparison of experimental results and TRM predictions for sensor 2 performance

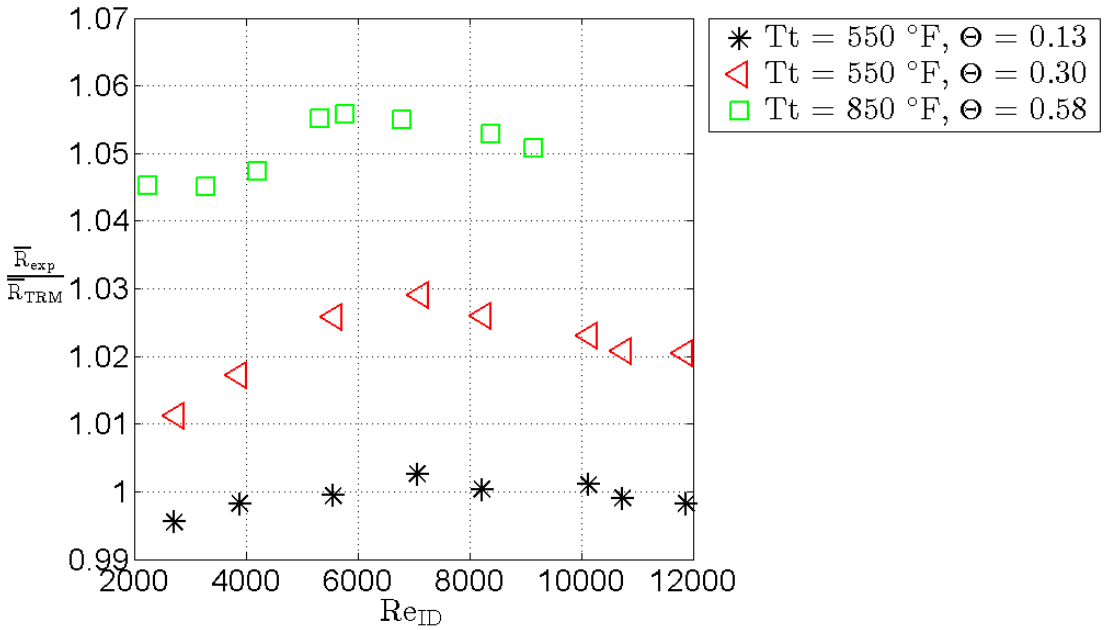

Figure 4.10: Ratio between sensor 2 experimental data and thermal resistance model predictions.

4.3 Physical Model Characterization

Recall that the results from the thermal resistance model were clearly a function of Reynolds number and conduction driver and successfully collapsed on these two parameters using Equation (2.18) presented earlier in section 2.3.6. This model form is shown again in Equation (4.1) for clarity.

$$R = 1 - \frac{c_1 \Theta}{\cosh\left(c_2 \mathrm{Re}^{0.337}\right)} \tag{4.1}$$

The validity of this functional form was shown to be viable when fitting to the results of the thermal resistance model. The experimental data will be fit to this statistical model to determine its validity.

4.3.1 Sensor 1 Collapse using Moffat's Functional Form

The results for the data collapse using the historical functional form is expressed in Table 3. The RMS deviation between all Type K experimental data and the surface fit is 0.0085 which indicates that sensor performance estimated from the surface fit is generally within 0.85% of the experimental flow total temperature. The L_∞ norm indicates that the maximum deviation between sensor performances estimated from the surface fit is 4.03% of the flow total temperature that was experimentally measured. The coefficient of determination, R-sq, shows that the statistical model using the historical functional form explains 58.45% of the variance in sensor performance. This is nowhere near as strong as the fit to the thermal resistance model, which had an R-sq of 0.9979. The decrease in the statistical model correlation is likely due to experimental uncertainty, differences between actual sensor geometry and geometry used in the low-order model, as well as thermal contact resistance.

Inspection of Figure 4.11 indicates that the sensor performance at low conduction driver clearly is not behaving as expected. Sensor 1 performance decreases when the conduction driver decreases from about 0.3 to 0.05. This completely goes against previously discussed performance trends. It is necessary to determine how the Type K data set behaves when these uncooled data sets are removed. The data collapse results for sensor 1 with the uncooled data sets removed are expressed in Table 4. The surface fit and all resulting data set is shown in Figure 4.12. The deviation between experimental data and the surface fit is shown in Figure 4.13. It is observed that the greatest deviation generally occurs at low Reynolds number, due to the lower convective heat transfer.

Recall the theoretical value of c_1 to be one and the theoretical value for c_2 to be $2\frac{L}{d}\sqrt{0.085\frac{k_{flow}}{k_{sheath}}}$. The actual value for c_1 is 72.66% lower than the theoretical value of one. Scaling of the correction factor $\Theta/\cosh(c_2\mathrm{Re}^{0.337})$, indicates sensor 1 is not as sensitive to conduction error as the analytical solution for conduction error suggests for an exposed thermocouple. The actual value for c_2 is 73.67% lower than the theoretical value of 0.473. The L/d value for sensor 1 is approximately 18, while the average k_{flow}/k_{sheath} value is equal to 0.0020. The deviation between theoretical and actual values for the fit coefficients agrees with the deviations that the low-order model fit coefficients had. Given that c_1 is nearl 73% lower than the theoretical value of one, Sensor 1 results are even less sensitive to the conduction error relationship involving the conduction driver and Reynolds number than the low-order model results suggest.

Removing the uncooled data sets greatly improved the data fit to the statistical model. The value of R-sq increasing to 0.9111 indicates that 91.11% of the variation in sensor performance due to Reynolds number and conduction driver is explained. The fit constants remained nearly the same;

the coefficients for 95% confidence changed substantially which further validates how the uncooled data sets were not in agreement with the remaining data.

Table 3: Summary of sensor 1 surface fit result using model form expressed in Equation (4.1).

RMS Error	R-sq	L_∞ Norm	Fit constant c1	Fit constant c2
0.0085	0.5845	0.0403	0.2751 +/- 0.0849	0.1245 +/- 0.0188

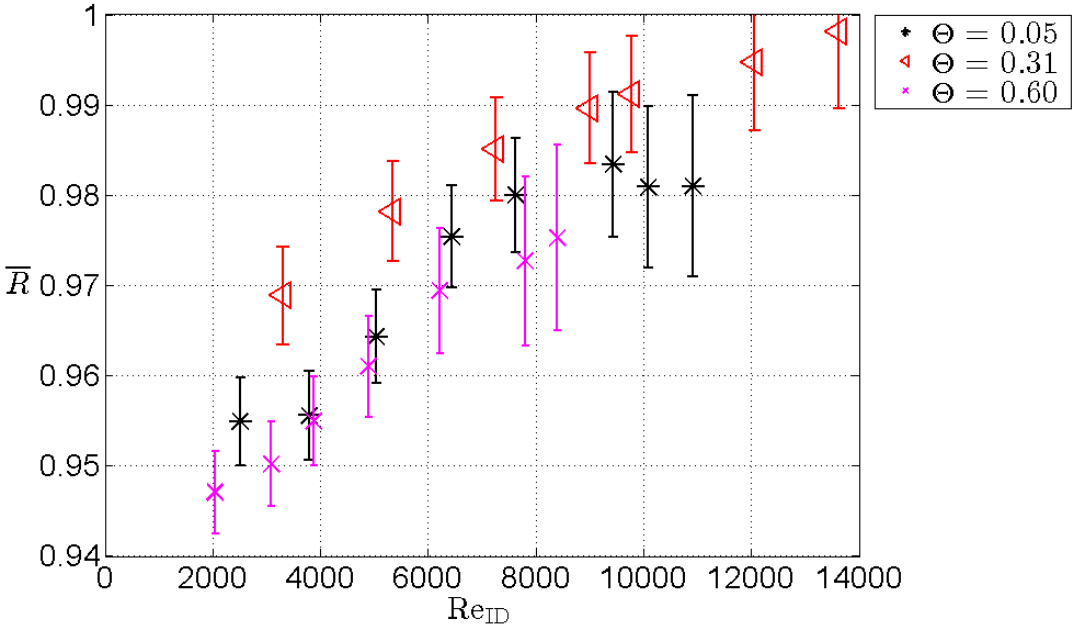

Figure 4.11: Unexplained uncooled sensor 1 performance trend.

Table 4: Summary of Type K surface fit with cooling off data sets removed

RMS Error	R-sq	L_∞ Norm	Fit constant c1	Fit constant c2
0.0040	0.9111	0.0114	0.2734 +/- 0.0401	0.1245 +/- 0.0089

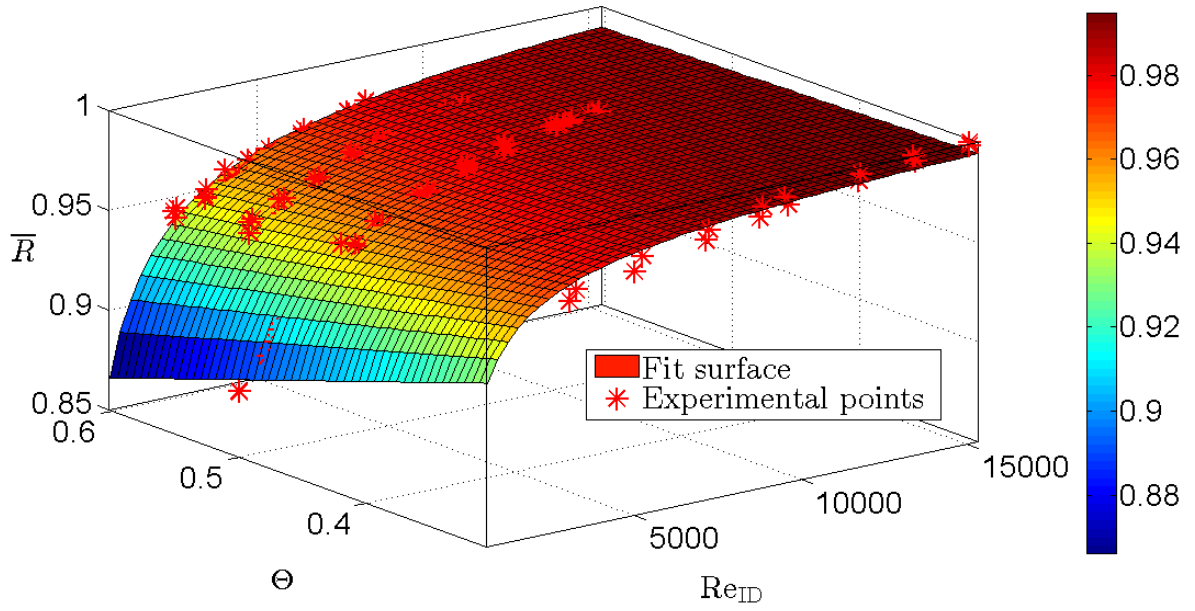

Figure 4.12: Surface fit for Type K data with cooling-off data sets removed

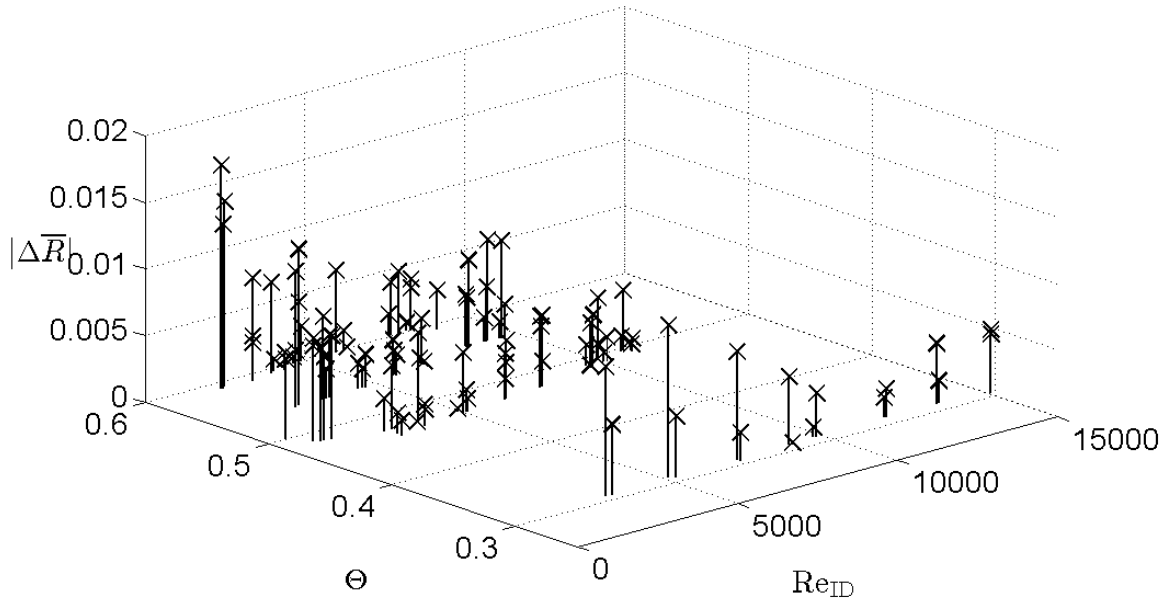

Figure 4.13: Absolute deviation between sensor 1 experimental data and surface fit.

4.3.2 Sensor 2 Data Collapse using Moffat's Functional Form

The results for the data collapse using the historical functional form is expressed in Table 5. The surface fit and all experimental data is shown in Figure 4.14. The RMS deviation between all sensor 2 experimental data and the surface fit is 0.01185 which indicates that sensor performance estimated from the surface fit is generally within 1.185% of the experimental flow total temperature. The L_∞ norm indicates that the maximum deviation between sensor performances estimated from the surface fit is 2.98% of the flow total temperature that was experimentally

measured. The coefficient of determination, R-sq, shows that the statistical model using the historical functional form explains 86.57% of the variance in sensor performance. This is not as good an agreement of the statistical model fit with the data from sensor 1, seen previously in Table 4. This difference is explained by the differences in sensor geometry. Sensor 1 has geometry most similar to the assumed geometry of the fin equation discussed earlier in the derivation of Equation (4.1). The deviation between experimental results and the surface fit is shown in Figure 4.15.

Recall the theoretical value of c_1 to be one and the theoretical value for c_2 to be $2\frac{L}{d}\sqrt{0.085\frac{k_{flow}}{k_{sheath}}}$. The actual value for c_1 is just 6.19% lower than the theoretical value of one. Scaling of the correction factor $\Theta/\cosh(c_2 Re^{0.337})$, indicates sensor 1 is not as sensitive to conduction error as the analytical solution for conduction error suggests for an exposed thermocouple. The actual value for c_2 is 27.1% lower than the theoretical average value of 0.206. The L/d value for sensor 2 is approximately 15.6, while the average k_{flow}/k_{sheath} value is equal to 0.00052. These fit coefficients for sensor 2 are in much better agreement with theoretical values. This agreement indicates that sensor 2 is more sensitive to conduction error described by the physical model fit.

Table 5: Summary of sensor 2 surface fit result using model form expressed in Equation (4.1).

RMS Error	R-sq	L_∞ Norm	Fit constant c1	Fit constant c2
0.0118	0.8657	0.0298	0.9381 +/- 0.1867	0.1504 +/- 0.0126

a

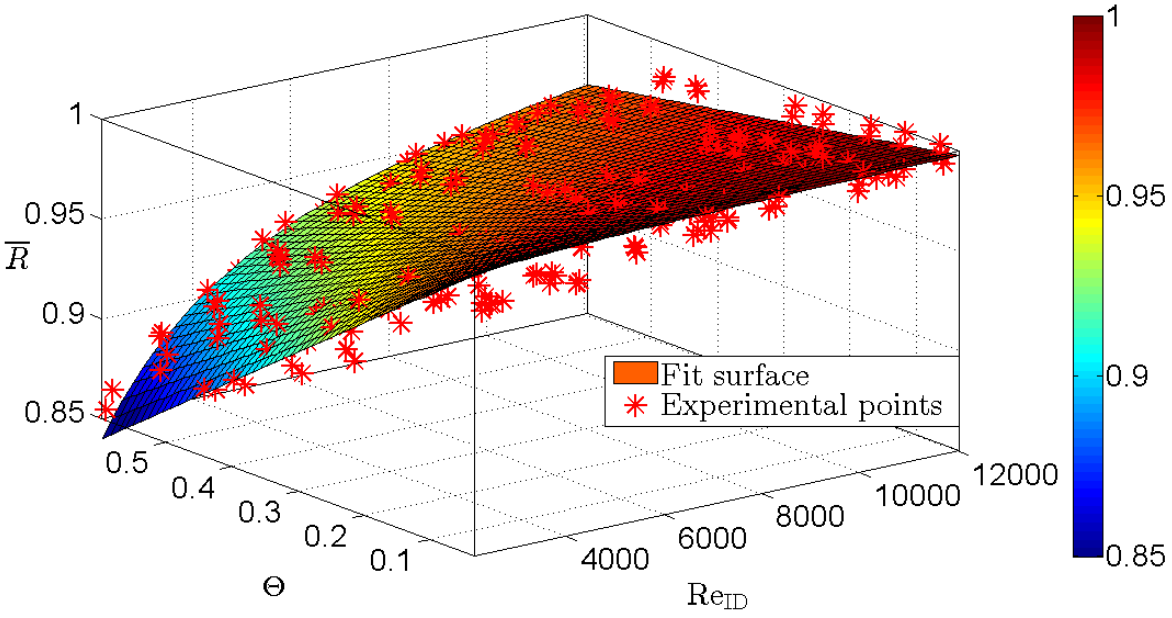

Figure 4.14: Surface fit of all sensor 2 data.

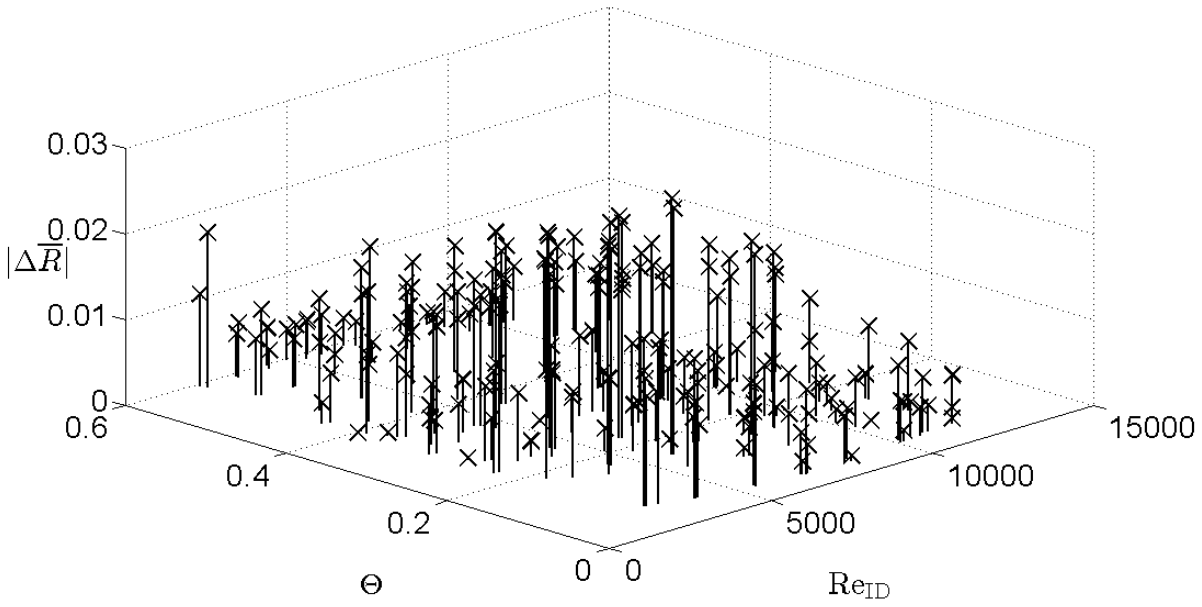

Figure 4.15: Absolute deviation between sensor 2 experimental data and surface fit.

4.3.3 Collapse of both Sensors via Biot Number

Recall that Moffat's model can be recast expressing sensor performance as a function of conduction driver, L/d, and Biot number. This formulation is expressed in Equation (2.12) in section 2.1. Moffat's model is derived assuming the heat transfer at the sensor tip is negligible compared to the heat transfer across the lateral surface of the sensor.[11] Replacing this assumption with a more physically accurate one that includes heat convection at the tip yields the following statistical model in Equation (4.2).[10] This model was successfully used by Warren for analytical conduction error correction.[38]

$$R = 1 - \frac{c_1 \Theta}{\cosh\left(c_2\sqrt{Bi}\right) + c_3 Bi \cdot \sinh\left(c_2\sqrt{Bi}\right)} \tag{4.2}$$

The fit constant c_2 should tend to be proportional to the sensor L/d. An additional constant c_3 was added to the hyperbolic sine term to capture the heat convection at the sensor tip that the Biot number might not capture, and other material properties are absorbed by this constant. Note that the Biot number is computed in accordance with Equation (2.9) in section 2.1. Thus this Biot number calculation uses Moffat's Nusselt and Reynolds number correlation, effectively making the Biot number a function of Reynolds number. The statistics for collapsing data from both sensors are presented in Table 6. This statistical model explains 71% of the variation in sensor performance as a function of Biot number and conduction driver. This indicates a moderately strong correlation between sensor performance with Biot number and conduction driver.

This statistical model of all sensor performance using Biot number and conduction driver should be taken to be a general rule for sensor performance. The geometry of both tested sensors were extremely different thus making the data collapse of both sensor challenging. Sensor 2 features

geometry that ultimately lead to an ambiguous definition of sensor L/d, while sensor 1 featured traditional geometry.

Figure 4.16 shows all experimental data for both sensors strictly as a function of Biot number and conduction driver. Note that the cooling-off runs for sensor 1 are still removed. The same roll-off of sensor performance is seen at both high conduction drivers and low Biot numbers. This is directly related to the trends previously seen with the model using a Reynolds number parameter. It is important to note that the Biot number has been assumed to scale on the Reynolds number, thus the same model behavior is expected. The physics of the problem is governed by the Biot number, which in turn relies on the Reynolds number for convective heat transfer. Figure 4.17 shows the deviation between the experimental data and the surface fit. The deviation is relatively constant for sensor 1 data, though it tends to increase as the conduction driver increases. This behavior is also seen in the deviation for sensor 2. The deviation for sensor 2 data is significantly higher than the deviation for the sensor 1 data. This is likely due to the geometry of sensor 2 not being appropriately captured by the model expressed in Equation (4.2). This form is representative of the geometry for sensor 1.

Table 6: Summary of surface fit result using statistical model expressed in Equation (4.2)

RMS Error	R-sq	L_∞ Norm	Fit constant c1	Fit constant c2	Fit constant c3
0.0146	0.7122	0.0376	0.4310 +/- 0.0649	22.990 +/- 2.091	-19.078 +/- 2.052

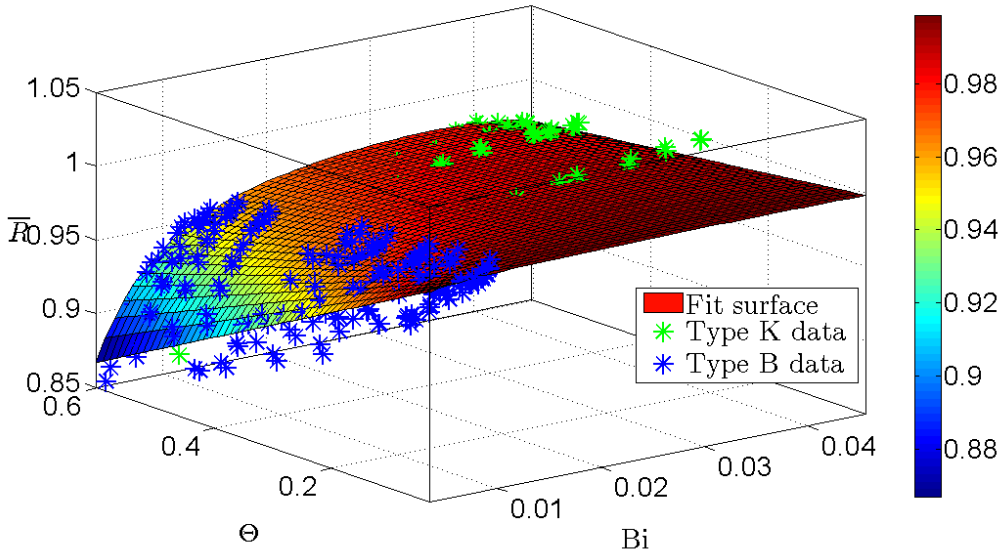

Figure 4.16: Surface fit for all Type B data and Type K data, uncooled Type K data removed

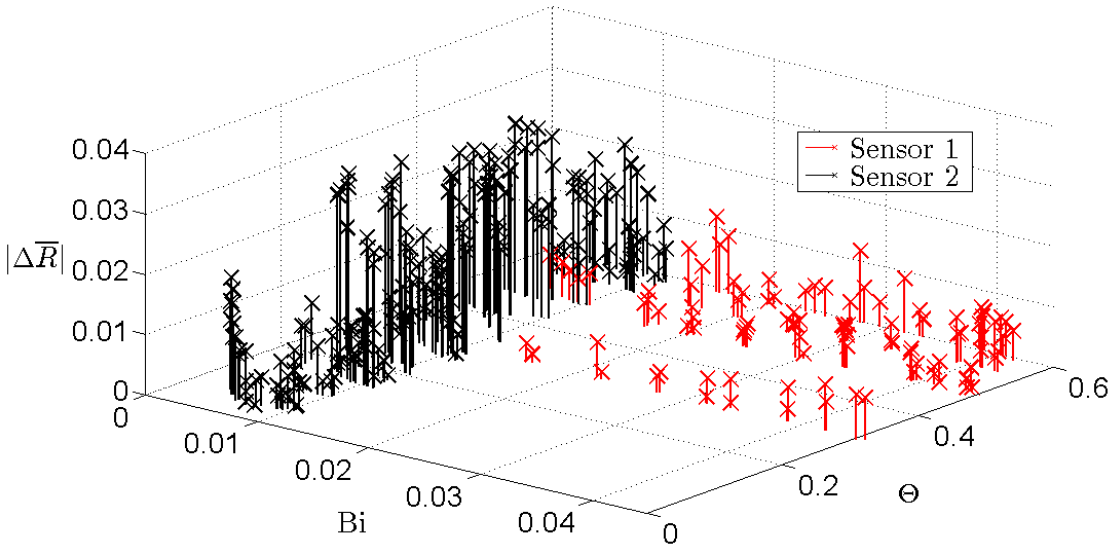

Figure 4.17: Absolute deviation between all experimental data and surface fit.

4.4 Recommendations on an Appropriate Calibration Procedure

Experimental rigs in industry often do not know the value of the flow total temperature with low uncertainty. The experimental procedure and results presented sensor performance as a function of Reynolds number and conduction driver. The statistical model results in Table 4 and Table 5 allow a procedure to extract a particular sensor's calibration. The calibration of a sensor is governed by non-dimensional parameters, namely the Reynolds number and the conduction driver for the purpose of the data fit to the statistical model.

The surface fit for experimental data for a particular sensor can be used to estimate the unknown flow total temperature from knowledge of the Reynolds number, base temperature, and junction temperature indicated by the sensor. Recall that the Reynolds number uses the external flow conditions but scaled on the inlet diameter to the sensor. An initial guess for the recovery factor is used to start the iterative procedure. The performance of the sensor is not sensitive to the initial performance guess. The initial recovery factor guess R_0 is used to calculate a value for the total temperature from the junction temperature in Equation (4.3).

$$T_t = T_j / R_0 \tag{4.3}$$

The Reynolds number is then adjusted to recalculate gas properties at the new total temperature and the conduction driver term, $\Theta = 1 - T_b/T_t$ is computed. The recovery factor is calculated using the model described in the surface fit. The total temperature is then extracted from the newly calculated recovery factor and is compared to the previously calculated total temperature value. This procedure is iterated until the difference between total temperature iterations is within some specified temperature tolerance. An example is presented in Appendix B: Example Calibration Procedure Calibration of total temperature sensors in a rig that accentuates conduction error is needed to understand how cooled sensor performance relies on conduction conditions. The sensor performance can then be expressed in terms of non-dimensional parameters that can be used universally.

5 CONCLUSIONS

A fundamental study of conduction error on total temperature probes has been performed in this work and a calibration procedure has been proposed and is demonstrated in Appendix B: Example Calibration Procedure. A thermal resistance model was developed in order to predict the performance of total temperature sensors when exposed to large temperature differences between the flow and sensor base. This model was developed based on the results presented by Moffat.[2] The thermal resistance model was used to validate Moffat's conclusions regarding the important parameters governing conduction error of thermocouples. The effect of the Reynolds number and dimensionless conduction driver was studied and determined to be critical parameters for total temperature probe performance. The thermal resistance model proved conduction error calibration to be governed by dimensionless parameters, namely the conduction driver as well as the Nusselt, Biot, and Reynolds number. This result indicates that conduction error calibration can be performed in any flow regime and can be universally used, provided that velocity and radiation error are appropriately accounted for. This indicates that total temperature probes can be calibrated in experimental facilities where the operating conditions are well known. These calibrations can then be used to calculate the flow total temperature in facilities where the operating conditions may not be accurately known. The thermal resistance model successfully verified the conduction error model introduced by Moffat.

An experiment to study conduction error of total temperature probes was designed and conducted in the Virginia Tech Hot Jet facility. The total temperature probes under test are embedded in a cooled strut in order to develop the driving conduction mechanism. Experimental data was obtained for two total temperature probes; one developed internally by Virginia Tech with conventional design and a proprietary second probe. Data was collected over total temperatures ranging from 550 °F to 850 °F with Mach number varying between 0.15 and 0.8 which resulted in probe Reynolds numbers between 2,000 and 12,000. Experimental data shows sensor performance strongly depending on both conduction driver and Reynolds number. This is in agreement with historical results and predictions from the thermal resistance model. The experimental data was collapsed on conduction driver and Reynolds number using an appropriate statistical model formed from a heat transfer solution. The statistical model captured most of the variation of sensor performance with respect to these two parameters and serves as the "calibration surface" for the probe.

The model fit of all experimental data is inherently physics based. The simple heat transfer solution presented by Moffat serves as an effective statistical model to represent total temperature probe performance. The high level of agreement between experimental data and the model fit verifies that the performance of total temperature probes is largely a function of Reynolds number and conduction driver. Additionally, the thermal resistance model predictions verified the model fit. Recall that the model fit can express total temperature probe performance as either a function of Reynolds number or Biot number. The governing physics of the problem simplifies to dependence on the conduction driver, sensor geometry, i.e. the L/d, and the Biot number. It is important to recognize that the problem at hand is inherently governed by Biot number, however, it is not practical to implement this parameter into a calibration procedure. Due to the difficulty in

experimentally measuring the convective heat transfer coefficient, and thus the Biot number, it is more practical to use the Reynolds number as a governing parameter for conduction error calibration.

This study proves conduction error to be governed by dimensionless parameters, the conduction driver and Reynolds number in this case, thus indicating sensor performance to be constant for any constant combination of conduction driver and Reynolds number. This is a powerful result in the fact that if these two parameters are known, then the sensor performance can be estimated using the "calibration surface" result from the model fit. This particular recovery factor can be used independent of temperature regime, as long as radiation effects are kept small or corrected for.

The effect of dimensionless conduction driver Θ on sensor performance has been studied using Moffat's model and the thermal resistance model. Experimental data for both sensor types was obtained. All models and experimental data indicate that sensor performance is dependent on the conduction driver, most noticeably at lower Reynolds number where heat convection is lower. The only exception to this was for the uncooled case for sensor 1. It was expected for the recovery to increase rather than decrease. This behavior was successfully repeated between multiple days, however, this goes against the physics of the problem and is not currently understood.

The conduction driver is the parameter that is used to describe how measurement error scales due to conduction. The measurement junction temperature is the result of a heat transfer balance via convection from the fluid and conduction from the junction. The second law of thermodynamics states that for an irreversible process, such as heat transfer via conduction, heat flows from a point of high temperature to low temperature. This is directly analogous to the flow of current from high electric potential to low electric potential, previously discussed in the thermal resistance model. As the base temperature decreases, more heat transfer will occur from the thermocouple junction, i.e. the hottest part of the thermocouple, to the base; the coldest part of the thermocouple. The thermocouple base is in direct thermal contact with the strut, which ultimately serves as a heat sink. This conduction effect balances with the convective heat transfer to yield a lower steady-state thermocouple junction temperature.

Significant differences exist between experimental data and low-order predictions. This stems from the previous discussion on the limitations of the thermal resistance model in section 2.3.5. When a temperature gradient does not exist between the base and thermocouple junction, the predicted recovery is 1.0. The experimental data contains errors due to random sources as well as error due to radiation that is assumed to be small. The radiation error was assumed to be small enough to ignore. The thermal resistance model does not include these sources of error. Furthermore, thermal contact resistance between the probe assembly and the cooled strut is an experimental unknown; the actual base temperature on the thermocouple is different than the base temperature of the strut. This leads to a lower conduction driver value that should be used as an input to the thermal resistance model. This variation in conduction driver is difficult to estimate due to thermal contact resistance.

Experimental results for sensor 1 show a good comparison to the high fidelity CFD simulations performed by Schneider.[43] The CFD results appear to collapse on conduction driver, as expected

and closely agree with the experimental data. All results shown indicate the same performance trend with Reynolds number. The thermal resistance model predictions follow the same characteristic with Reynolds number that the experimental and computation results have. There is a near constant offset between the thermal resistance predictions and experimental results of about 5% of the total temperature. This indicates that the thermal resistance model effectively captures the Reynolds number dependence of sensor 1. The nearly constant offset can be considered a bias error due to the true base temperature at the exact point of contact between the thermocouple and cooled strut being unknown.

Experimental results for sensor 2 show good agreement with the thermal resistance model at low conduction drivers. Sensor 2 data indicates that as the conduction driver increases, the deviation between experiment and prediction increases. The geometry of this sensor is significantly different than sensor 1 and the thermal resistance model was modified accordingly

This study presents an experimental setup to calibrate for conduction error and suggests an iterative calibration procedure that may be used in any conditions to determine the flow total temperature. The sensitivity of the calibration procedure is dependent on the uncertainties of the input parameters, namely uncertainties in base temperature and sensor Reynolds number. The sensitivity of the calibration procedure for conditions typically found in engine diagnostics, combined with the inherent uncertainty in the instruments used, yields an accuracy on the order of ±4% of the flow total temperature with extremely conservative estimates of ±30% uncertainty in both base temperature and Reynolds number.

5.1 FUTURE WORK

Future work should include a set of experiments that use numerous sensors of identical geometry but of different thermal conductivity. This allows the Biot number to truly be isolated for study. The current work studies two sensors of different thermal conductivity but of radically different geometry. Additionally, sensors using exposed bare wire junctions should be studied; total temperature sensor literature discusses exposed thermocouple junctions, as does Moffat, though this study uses sheathed, ungrounded thermocouple junctions.

REFERENCES

1. Hill, P.G and Peterson, C.R. "Mechanics and Thermodynamics of Propulsion." 2nd ed. Addison-Wesley Publishing Company, Inc, New York, 1992. pg. 21.
2. Moffat, R.J. "Gas Temperature Measurement." Temperature: Its Measurement and Control in Science and Industry: Volume 3, Part 2. 1962
3. Scadron, M.D. and Warshawsky, I. "Experimental Determination of Time Constants and Nusselt Numbers for Bare Wire Thermocouples in High Velocity Air Streams and Analytical Approximation of Conduction and Radiation Error." NACA TN-2599. 1952.
4. King, W.J. "Measurements of high temperatures in high velocity gas streams." Trans. ASME 65, 421. 1943.
5. Rohsenow, W.M. "A graphical determination of unshielded thermocouple thermal corrections." Trans. ASME 68. 1946.
6. Haig, L.B. "A Design Procedure for Thermocouple Probes." SAE Preprint 158C. 1960.
7. Hottel H.C. and Kalitinsky, A. "Temperature measurements in high velocity air streams." Trans. ASME 67, A-25. 1945.
8. Glawe G., Simmons F.S., and Stickney T.M. "Radiation and Recovery Corrections and Time Constants of Several Chromel-Alumel Thermocouple Probes in High Temperature, High Velocity Gas Streams." NACA TN-3766. 1956.
9. Simmons, F.S. "Recovery Corrections for Butt Welded Straight Wire Thermocouples in High Velocity, High Temperature Gas Streams." NACA RM-E54G22a. 1954
10. Eckert, E.R.G. and Drake, R.M. "Heat and Mass Transfer." McGraw-Hill Book Company, Inc. New York. 1959. pg. 39-42.
11. Özişik, M.N. "Basic Heat Transfer." McGraw Hill Book Company. New York. 1977. pg. 68-71.
12. Dahl, A.I. and Fiock, E.F. "Thermocouple pyrometers for gas turbines." Trans. ASME 71, 153. 1949.
13. Moffatt, E.M. "Multiple Shielded High Temperature Probes – Comparison of Experimental and Calculated Errors." SAE T-13. 1952.
14. West, W.E. and Westwater, J.W. "Radiation-conduction correction for temperature measurements in hot gases." Ind. and Eng. Chem. 45, 2152-2156. 1953.
15. Dahl, A.I. and Freeze, P.D. "Tests of Total Temperature Probes." WADC Technical Report 53-251. 1953.
16. Glawe, G.E. and Shepard, C.E. "Some effects of exposure to exhaust-gas streams on emittance and thermoelectric power of bare wire platinum rhodium-platinum thermocouples." NACA TN-3253. 1954.
17. Hottel, H.C., and Sarofim, A.F.: "Radiative Transfer," McGraw-Hill Book Company, New York 1967
18. Özişik, M.N.: "Radiative Transfer and Interations with Conduction and Convection," John Wiley & Sons, Inc., New York, 1973.
19. Singham, J.R.: Tables of Emissivity of Surfaces, Int. J. Heat Mass Transfer, 5:67-76 (1962)
20. Gubareff, G.G, Janssen, J.E: "Thermal Radiation Properties Survey," Honeywell Research Center, Honeywell Regulator Company, Minneapolis, 1960.
21. Glawe, G.E. and Shepard, C.E. "Some effects of exposure to exhaust-gas streams on emittance and thermoelectric power of bare-wire platinum rhodium-platinum thermocouples." NACA TN-3253. 1954.

22. Werner, F.D., Keppel, R.K., and Bernard, M.A., "Design and Performance Studies for Improved Multiple Shielded Total Temperature Probes," ASTIA-DSC AD-27 727.
23. Doeblin, E. "Measurement systems – application and design." McGrawl-Hill Book Company. New York. 2004.
24. Goodwin, W. N., Response time and lag of a thermometer element in a protecting case, Am. Inst. Elec. Engrs. 64, 665 (1945)
25. Moffat, R.J. "Designing thermocouples for response rate." Trans. ASME 80, 257. 1958.
26. Dahl, A.I. and Fiock, E.F. "Response characteristics of temperature sensing elements for use in the control of jet engines." J. Research Natl. Bur. Standards, Vol. 45, No. 4. 1950.
27. Wormser, A.F. "Experimental determination of thermocouple time constants with use of a variable turbulence, variable density wind tunnel, and the analytic evaluation of conduction, radiation, and other secondary effects." SAE Preprint 158D. 1960.
28. Shepard, R.L. and Carroll, R.M. "Measurement of the transient response of thermocouple and resistance thermometers using an in situ method." ORNL/TM-4573. 1977.
29. Shepard, C.E. and Warshawsky, I. "Electrical techniques for compensation of thermal time lag of thermocouple and resistance thermometers." NACA TN-2703. 1952.
30. Franz, A. "Pressure and temperature measurements in supercharger investigations." NACA TM 953. 1940.
31. Keenan, J.H. and Kaye. J. "Gas Tables". John Wiley & Sons, Inc. New York. 1948. pg. 139.
32. Bontrager, P.J. "Development of thermocouple-type total temperature probes in the hypersonic flow regime." AEDC-TR-69-25. 1960.
33. Willbanks, C.E. "Recovery characteristics of a single-shielded self-aspirating thermocouple probe at low pressure levels and subsonic speeds." J. Phys. E.: Sci. Instrum. 6. 1973
34. Zeisberger, A. "Total temperature probes for turbine and combustor applications." ISABE-2007-1108. 2007
35. Villafane, L. and Paniagua, G. "Aero-thermal analysis of shielded fine wire thermocouple probes." Int. J. Therm. Sci. 65. 2013.
36. Moffatt, E.M. and Markowski, S.J. "Instrumentation for development of aircraft powerplant components involving fluid flow." SAE Quarterly Trans. 1948.
37. Beede, H.M. and Droms, C.R. "A simplified thermocouple for temperature measurements in high velocity gas streams." Instruments 24, 338. 1951.
38. Warren, R.C. "Design of thermocouple probes for measurement of rocket exhaust plume temperatures." AD-A285 423. 1960.
39. Rhodes, R., Moeller, T.M., and May, M.M. "Prediction and experimental measurement of total temperature in an afterburning turbojet exhaust." AIAA 2012-0811. 2012.
40. Brooks, D.R., Ecker, T., Lowe, K.T., and Ng. W.F. "Experimental Reynolds stress spectra in hot supersonic round jets." Proceedings of the 52nd AIAA Aerospace Sciences Meeting. National Harbor, MD. AIAA-2014-1104. 2014
41. Wimmer, W. "Stagnation temperature recording." NACA Technical Memorandum No. 967. 1940.
42. Schetz, J.A. and Bowersox, R.D.W. "Boundary layer analysis." 2nd ed. AIAA Educational Series. 2011.
43. Schneider, A.J. "Computational modeling of total temperature probes." Masters thesis. Virginia Tech. 2015.

APPENDIX A: EXPANDED EXPERIMENTAL UNCERTAINTY AND MODEL SENSITIVITY

EXPERIMENTAL REPEATABILITY

The day-to-day repeatability of measurements is another measure of experimental uncertainty. The repeatability is taken to be the deviation from the mean of two data sets. This is performed for all data sets for sensor 2. The average of the deviations from mean between all respective sensor 2 data sets will indicate the overall repeatability for sensor 2. Figure A.1 shows these deviations.

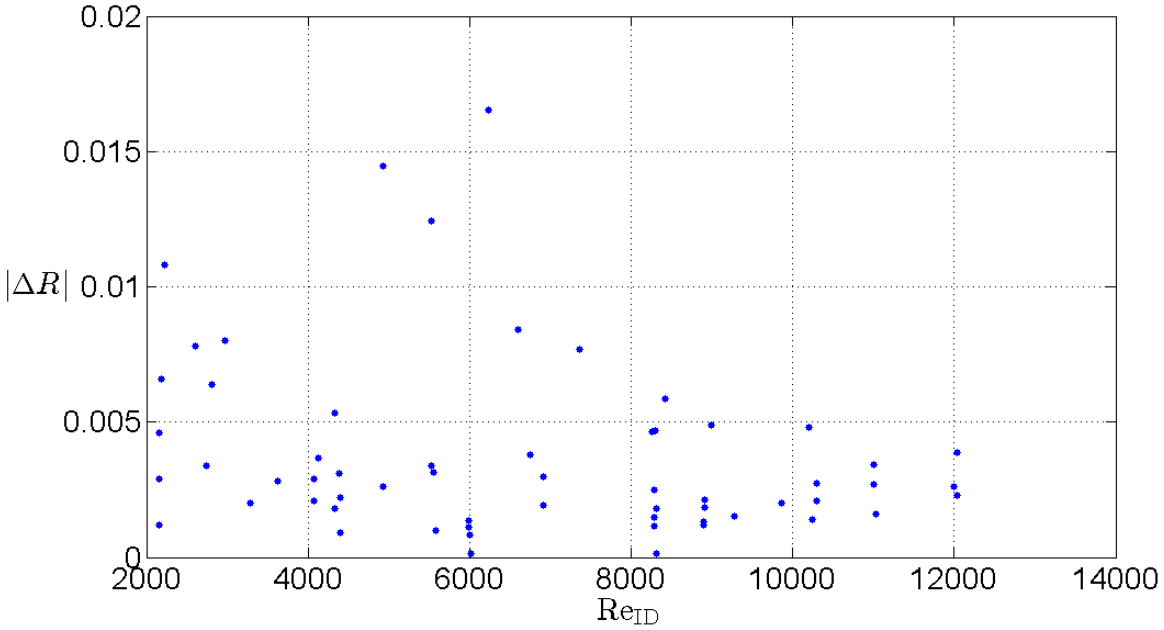

Figure A.1: Deviation between same sensor 2 data sets

Taking the average of all deviations shown in Figure A.1 yields a measure of the average repeatability across all Type B data sets. The average deviation for these data sets comes out to be 0.0019. Thus the total uncertainty due to inherent instrument uncertainty and experimental repeatability is ±0.0044. This is a measure of how well any singular data point captures the true recovery factor for sensor 2.

$$\delta R = \sqrt{\delta R_{instr}{}^2 + \delta R_{repeatabil\ ity}{}^2} \tag{A.1}$$

STATISTICAL MODEL SENSITIVITIES

While the experimental conditions are well controlled in this study, other experimental rigs may not always know what the specific operating conditions are. Due to this, it is necessary to determine how sensitive the model is to large uncertainties in the driving parameters, i.e. conduction driver and Reynolds number. These uncertainties in rig conditions can be ultimately expressed as

uncertainty in sensor recovery factor. It is assumed that the primary uncertainties are in the base temperature measurement and the Reynolds number calculation. Again, the total temperature of the flow is an unknown that is iteratively solved for using the "calibration surface" that describes the performance of the sensor.

Before the sensitivity is explored, the best achievable uncertainty of the statistical model must be discussed. Table 3 through Table 5 contain 95% confidence intervals for the calculated fit constants. These intervals indicate the uncertainty bounds for how well the calculated function fits the experimental data. These intervals conservatively contain the experimental uncertainty due to day to day repeatability of results. The uncertainty in sensor performance using the iterative calibration procedure is produced by perturbing the two fit constants, c_1 and c_2, by their respective confidence interval and observing the effect that is has on the calculated recovery factor. These combinations are shown in Table 7. The median value for recovery is obtained by not perturbing the fit constants at all, represented as R_0 in the coefficient table. The resulting maximum and minimum recovery factors obtained from including the uncertainty due to the confidence intervals are used to characterize the overall uncertainty in the iteratively calculated recovery factor. Thus the upper bound on the uncertainty is calculated by taking the maximum recovery of R_1 through R_8 and subtracting the median recovery R_0 from it. The lower bound recovery uncertainty is determined by subtracting the minimum recovery of R_1 through R_8 from the median recovery R_0. The resulting uncertainty bound is not symmetric and is weighted towards the lower bound. This calculated uncertainty is strictly from the confidence intervals of the fit constants; the uncertainty in the calculated sensor performance cannot be less than these values.

Table 7: Perturbation of calibration surface fit coefficients.

C_1 value	C_1	$C_1+ C_{1,95}$	$C_1- C_{1,95}$	$C_1+ C_{1,95}$	$C_1- C_{1,95}$	C_1	C_1	$C_1+ C_{1,95}$	$C_1- C_{1,95}$
C_2 value	C_2	$C_2+ C_{2,95}$	$C_2- C_{2,95}$	$C_2- C_{2,95}$	$C_2+ C_{2,95}$	$C_2+ C_{2,95}$	$C_2- C_{2,95}$	C_2	C_2
Recovery	R_0	R_1	R_2	R_3	R_4	R_5	R_6	R_7	R_8

Now that the baseline uncertainty associated with the statistical model has been discussed, it is appropriate to determine the effect of uncertainty in base temperature and Reynolds number on the calculated sensor performance. The statistical model is of the form shown again in Equation (A.2).

$$R = 1 - \frac{c_1 \Theta}{\cosh\left(c_2 \,\mathrm{Re}^{0.337}\right)} \tag{A.2}$$

Using the propagation of errors, the uncertainty in this model due to base temperature and Reynolds number uncertainties is expressed in Equation (A.3) with the subsequent partial derivatives evaluated in Equations (A.4) and (A.5).

$$\delta R = \sqrt{\left(\frac{\partial R}{\partial T_b}\delta T_b\right)^2 + \left(\frac{\partial R}{\partial \mathrm{Re}}\delta \mathrm{Re}\right)^2} \tag{A.3}$$

$$\frac{\partial R}{\partial T_b} = \frac{c_1}{T_t \cosh\left(c_2 \,\mathrm{Re}^{0.337}\right)} \tag{A.4}$$

$$\frac{\partial R}{\partial \,\mathrm{Re}} = \frac{0.337 c_1 c_2 \Theta \tanh\left(c_2 \,\mathrm{Re}^{0.337}\right) sech\left(c_2 \,\mathrm{Re}^{0.337}\right)}{\mathrm{Re}^{0.663}} \tag{A.5}$$

The effect of base temperature and Reynolds number uncertainty was studied using the preceding equations for flow conditions commonly encountered at the turbine inlet. The sensor was assumed to have a temperature reading of 2800 °F, base temperature of 1800 °F, and Reynolds number of 4500. The uncertainty in base temperature and Reynolds number was varied from zero to 30% of their base value. The total uncertainty in calculated sensor performance is comprised of the uncertainty due to the statistical model confidence intervals and the uncertainty due to base temperature and Reynolds number. This is expressed in Equations (A.6) and (A.7) and subsequently plotted in Figure A.2 and Figure A.3.

$$\delta R_{tot,upper} = \sqrt{\left[\max(R_1 : R_8) - R_0\right]^2 + \delta R^2} \tag{A.6}$$

$$\delta R_{tot,lower} = \sqrt{\left[R_0 - \min(R_1 : R_8)\right]^2 + \delta R^2} \tag{A.7}$$

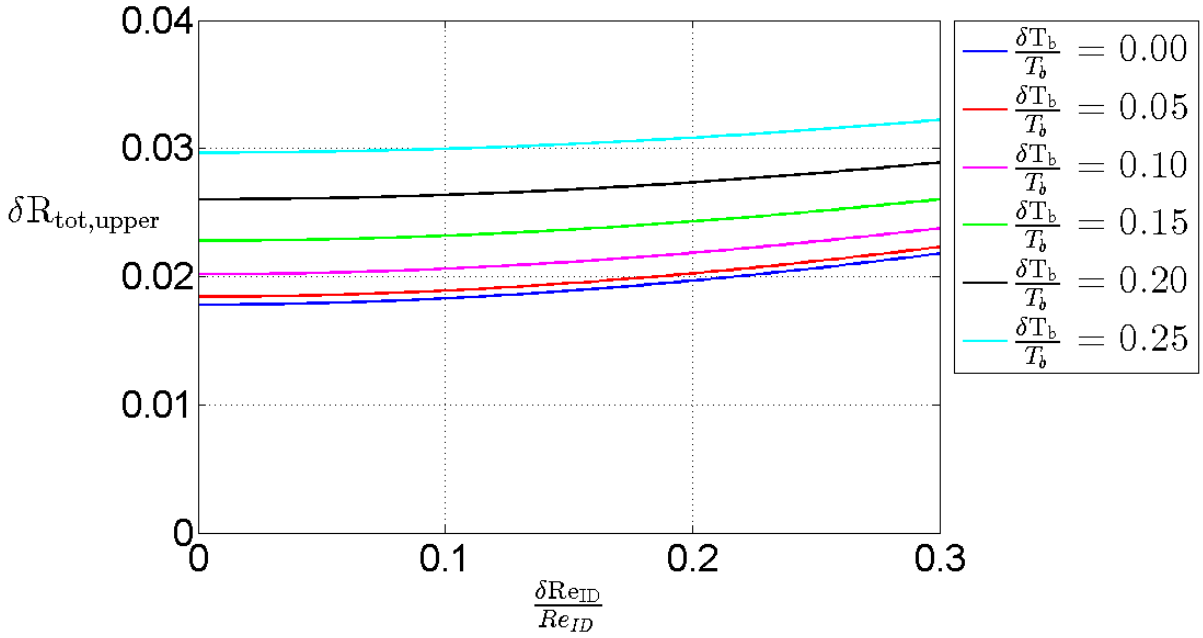

Figure A.2: Upper bound uncertainty for extrapolated sensor 2 performance

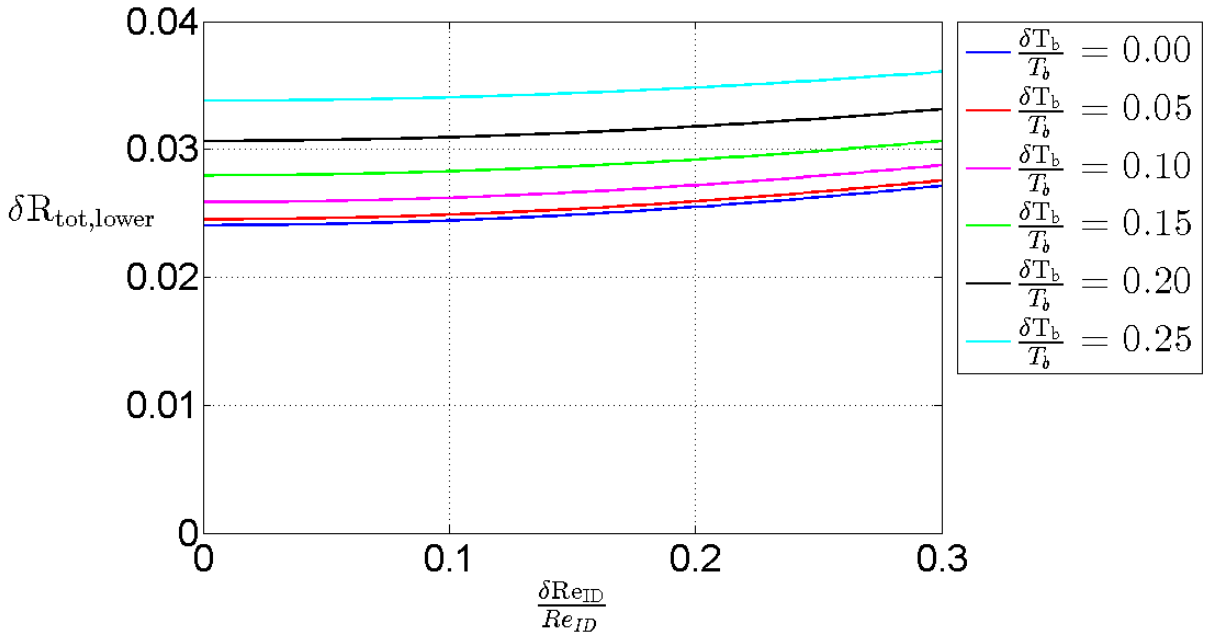

Figure A.3: Lower bound uncertainty for extrapolated sensor 2 performance

The intercept in each of these figures indicates the uncertainty due to the confidence intervals of the fit coefficients and the inherent uncertainty of the instruments. Moving along the 0% base temperature uncertainty line indicates how sensitive the total uncertainty is to the uncertainty in Reynolds number. Subsequently moving along the vertical axis, where the uncertainty in Reynolds number is zero, indicates how sensitive the total uncertainty is to the uncertainty in base temperature. Simple inspection along these two lines indicate that the sensitivity to base temperature uncertainty has a greater effect than the uncertainty in Reynolds number. These results indicate that even for severe uncertainty in Reynolds number and base temperature, the uncertainty in the flow total temperature is within approximately ±4%.

APPENDIX B: EXAMPLE CALIBRATION PROCEDURE

The iterative calibration procedure will be used to estimate the total temperature of the flow for sensor 2. The calibration surface found for sensor 2 is shown in Equation (B.1).

$$R = 1 - \frac{(0.9381 \pm 0.1867)\Theta}{\cosh\left((0.1504 \pm 0.0126)\mathrm{Re}^{0.337}\right)} \tag{B.1}$$

For this example, the uncertainty in base temperature T_b and in the probe Reynolds number Re_{ID} is assumed to be zero. The following inputs are required to be known for this calibration procedure: thermocouple junction temperature T_j, mount strut base temperature T_b, and freestream total and static pressures. The freestream pressures are used to calculate the Mach number, which in turn is used to calculate the Reynolds number in conjunction with the indicated thermocouple temperature. The calibration procedure is as follows:

1. Use T_j to guess T_t with a conservative first guess for R.
2. Compute the Reynolds number and conduction driver Θ using the calculated T_t.
3. Evaluate Equation (B.1) using the newly computed Reynolds number and conduction driver to obtain the new recovery factor value.
4. Compute the new T_t from the new R, i.e. $T_t = T_j/R$
5. Compare the value for T_t to the previously calculated T_t value
6. Iterate steps 2-5 until some stopping criteria is met, i.e. $\left|T_{t,i+1} - T_{t,i}\right| < \varepsilon$

The following inputs will be used to compute the flow total temperature: T_j = 750 °F, T_b = 300 °F, p_s = 100 kPa, p_t = 139 kPa. This pressure ratio is for a freestream Mach of 0.7. The results from the calibration procedure are shown in Table 8: Results from iterative calibration procedure for sensor 2. For this particular set of inputs, the flow total temperature was determined to be 788.85 (+15.3,-23.0) °F, resulting from a predicted recovery factor of 0.96887 (+0.0120,-0.0175). The Reynolds number was determined to be 8427 and the conduction driver to be 0.39. Figure B.1 shows the calculated region in a subset of the sensor 2 experimental data.

Table 8: Results from iterative calibration procedure for sensor 2: T_j = 750 °F.

Iteration count	Estimated Recovery	Conduction driver	Total temperature (°F)	Reynolds number
1	0.8	0.4155	840.04	6791.8
2	0.95088 (+0.030,-0.0004)	0.4028	812.48 (+24.1,-36.0)	8249.6
3	0.96738 (+0.0135,-0.016)	0.3924	790.77 (+16.0,-24.1)	8412.5
4	0.96887 (+0.012,-0.0175)	0.3915	788.85 (+15.3,-23.0)	8427.3

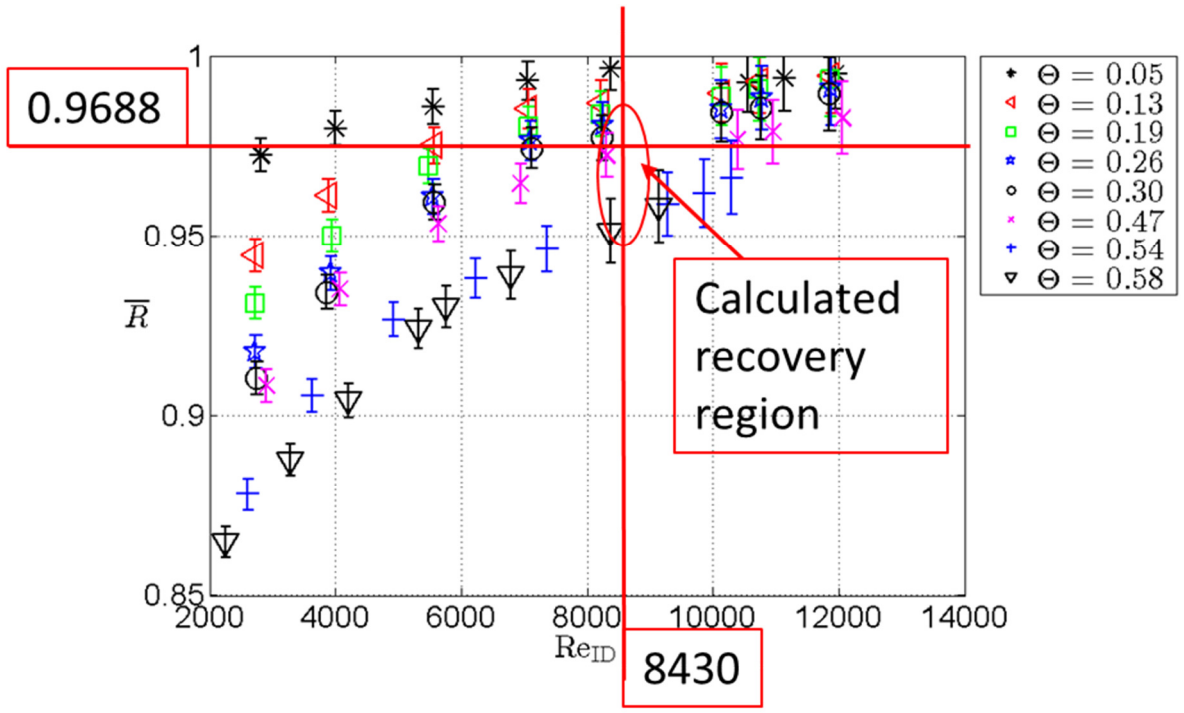

Figure B.1: Calculated recovery region from calibration procedure, T_j = 750 °F, T_b = 300 °F.

The following inputs will be used to compute the flow total temperature: T_j = 900 °F, T_b = 600 °F, p_s = 100 kPa, p_t = 111.6 kPa. This pressure ratio is for a freestream Mach of 0.4. The results from the calibration procedure are shown in Table 9. For this particular set of inputs, the flow total temperature was determined to be 951.04 (+18.4,-26.0) °F, resulting from a predicted recovery factor of 0.96887 (+0.0120,-0.0175). The Reynolds number was determined to be 4462 and the conduction driver to be 0.25. Figure B.2 shows the calculated region in a subset of the sensor 2 experimental data.

Table 9: Results from iterative calibration procedure for sensor 2: T_j = 900 °F.

Iteration count	**Estimated Recovery**	**Conduction driver**	**Total temperature (°F)**	**Reynolds number**
1	0.8	0.2452	944.22	3626.6
2	0.93526 (+0.0413,-0.0111)	0.2711	994.12 (+33.7,-47.7)	4314.8
3	0.95954 (+0.0170,-0.0131)	0.2521	957.34 (+20.6,-29.1)	4440.6
4	0.96326 (+0.0133,-0.0168)	0.2492	951.85 (+18.7,-26.4)	4460.0
5	0.96382 (+0.0127,-0.0174)	0.2488	951.04 (+18.4,-26.0)	4462.9

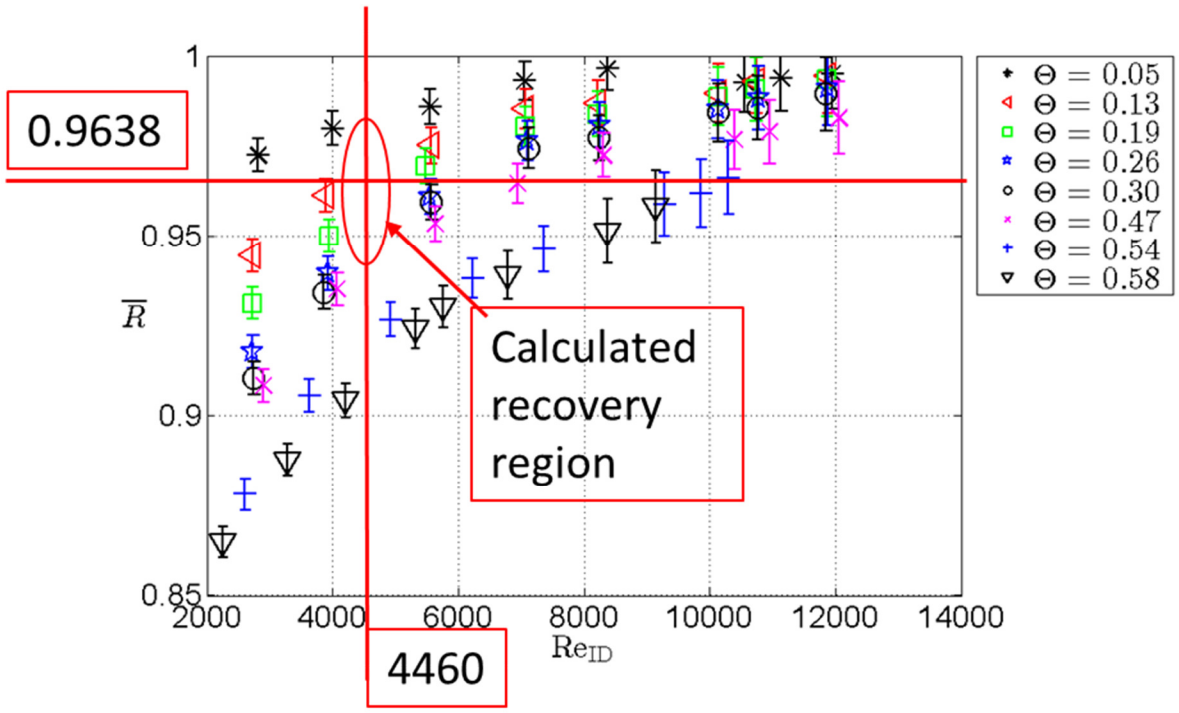

Figure B.2: Calculated recovery region from calibration procedure, T_j = 900 °F, T_b = 600 °F

APPENDIX C: ACQUISITION USER INTERFACE